Phenomenological Modeling of Pre-Ignition in Gas Engines

Von der Fakultät Konstruktions-, Produktions- und Fahrzeugtechnik
der Universität Stuttgart
zur Erlangung der Würde eines Doktor-Ingenieurs (Dr.-Ing.)
genehmigte Abhandlung

Vorgelegt von

Lukas Wißmann
aus Bietigheim-Bissingen

Hauptberichter:	Prof. Dr.-Ing. M. Bargende
Erster Mitberichter:	Prof. Dr. sc. techn. K. Herrmann
Zweiter Mitberichter:	Prof. Dr.-Ing. A. Casal Kulzer

Tag der mündlichen Prüfung: 26.10.2023

Institut für Fahrzeugtechnik
der Universität Stuttgart

2023

„The roots of education are bitter, but the fruit is sweet.“
Aristotle

Preface

This dissertation was created during my work as a research assistant at the Institute of Automotive Engineering (IFS) at the University of Stuttgart under the supervision of Prof. Dr.-Ing. M. Bargende.

My deep gratitude goes to Prof. Dr.-Ing. M. Bargende for his support and guidance. I want to thank Prof. Dr. sc. techn. K. Herrmann and Prof. Dr.-Ing. A. Casal Kulzer for their interest in this thesis and for joining the doctoral committee.

I would especially like to thank my supervisor, Dr. Michael Grill, for the professional exchange and helpful advice. I would also like to thank Sebastian Crönert, who supported me with his expertise and Sebastian Welscher who always had a good advice for me especially with coding issues. But I would also like to thank all other colleagues at the IFS and FKFS for the fruitful discussions and the good collegiality.

I would also like to thank the working group for the FVV project ”Phenomenological Modeling of Pre-ignition in Gas Engines” which was led by Dr. Markus Wenig. Special thanks are due to the BMWK and FVV for funding the project within the CORNET programme. I would also like to thank the company WinGD for providing measurement data and Dr. Fridolin Unfug for the expertise exchange in the field of marine engines. A big thanks also goes to the project partners Pascal Süess and Patrick Albrecht from the FHNW for providing the measurement data and the great cooperation.

Lastly, I would like to thank my family and friends, as well as my partner, who have supported me over the years.

Bietigheim-Bissingen

Lukas Wißmann

Kurzfassung

Für den Seetransport verwenden große Containerschiffe Dual-Fuel-Gasmotoren, die mit flüssigem Erdgas (LNG) betrieben werden. Auf Grund des besseren Verhältnisses von Kohlenstoff zu Wasserstoff von Erdgas im Vergleich zu denen von Diesel und Benzin bietet dieser Kraftstoff eine Möglichkeit, CO_2-Emissionen zu reduzieren. Des Weiteren sind bei der Verbrennung von Erdgas auch die Emissionen von SO_x, NO_x und Partikeln sehr gering, weshalb die geltenden Abgasvorschriften meist auch ohne teure Abgasnachbehandlung eingehalten werden können.

Beim Betrieb dieser Motoren kann es zu einer Vorentflammung des Luft-Kraftstoff-Gemischs kommen, was zu hohen Druckanstiegen im Brennraum führt. Im schlimmsten Fall können dadurch Bauteile des Motors beschädigt werden. Dieses Phänomen genauer zu verstehen und vorhersagen zu können, ist im Fokus der Entwicklung bei Marine-Gasmotoren. Bei PKW-Motoren treten Vorentflammungen ebenfalls auf, allerdings ist der Mechanismus nicht mit denen in einem großen Dual-Fuel-Motor zu vergleichen. Aus diesem Grund können bestehende Erkenntnisse aus der Forschung im PKW-Sektor auch nicht genutzt beziehungsweise übertragen werden. Bei direkteinspritzenden Ottomotoren kann es dazu kommen, dass flüssiger Kraftstoff mit der Zylinderwand in Berührung kommt. Die physikalischen Eigenschaften des Schmierölfilms ändern sich und das Öl kann von der Wand verdampfen oder es lösen sich auf Grund der veränderten Oberflächenspannung kleine Tropfen ab. Diese Tropfen entzünden sich und es kommt zu einer Vorentflammung. Bei einem Gasmotor tritt dieser Effekt nicht auf. Schmieröl wird allerdings bei den Großmotoren mit Düsen direkt auf die Zylinderwand gespritzt und es können Tropfen in den Brennraum gelangen. Auch sind bereits Schmieröltropfen in der Frischluft vorhanden. Diese Öltropfen sind der Hauptgrund für Vorentflammung bei Marine-Gasmotoren.

Bei PKW-Motoren werden Vorentflammungen auch durch heiße, sich durch den Brennraum bewegende Partikel, ausgelöst. Erdgas verbrennt im Gegensatz

zu Benzin jedoch nahezu rußfrei. Dieser Mechanismus ist deshalb auch zu vernachlässigen. Bei der schmierölinduzierten Vorentflammung ist vor allem die zur Verfügung stehende Zeit bei hohem Druck und hoher Temperatur entscheidend. Typische Motordrehzahlen für Marine-Gasmotoren liegen zwischen 70 und 100 Umdrehungen pro Minute, während selbst Leerlaufdrehzahlen von PKW's diesen Wert den um Faktor zehn übersteigen.

Der Betrieb von Vollmotorprüfstanden für große Schiffsmotoren ist sehr kostenintensiv. Auch 3D-CFD-Simulationen sind auf Grund der geometrischen Gegebenheiten sehr resourcenintensiv. In dieser Arbeit wird deshalb ein schnelles quasidimensionales Modell entwickelt, welches Vorentflammungen vorhersagen kann.

Um die Mechanismen einer Vorentflammung genauer zu analysieren, werden umfangreiche reaktionskinetische Untersuchungen durchgeführt. Als Werkzeug wird die Open-Source-Suite Cantera in Python verwendet. In einem nulldimensionalen Reaktor wird die initiale Gaszusammensetzung berechnet, welche als Randbedingungen die Kraftstoffzusammensetzung, den Druck, die Temperatur, das Luft-Kraftstoffverhältnis, den Abgasrückführungsanteil und die Schmierölkonzentration enthält. In einem Vergleich wird ein geeigneter Reaktionsmechanismus ausgewählt. Kriterien für dessen Eignung sind zum einen die Möglichkeit, auch langkettige Kohlenwasserstoffe, wie sie in Schmieröl vorkommen, zu modellieren, und zum anderen die Erdgasverbrennung darstellen zu könen.

Für die Zündungsdetektion sind vier verschiedene Kriterien implementiert. Zwei davon sind abhängig von der Temperatur (τ_{ignT400} und τ_{ignT300}) und zwei abhängig von der Konzentration des Radikals $^{\bullet}$OH ($\tau_{\mathrm{ignOHgrad}}$) und ($\tau_{\mathrm{ignOHmax}}$). Die temperaturabhängigen Kriterien sind erfüllt, wenn die Starttemperatur um 300 K (τ_{ignT300}) respektive um 400 K (τ_{ignT400}) überschritten wird. Die $^{\bullet}$OH-Radikal abhängigen Kriterien sind jeweils erfüllt, wenn die maximale $^{\bullet}$OH-Konzentration erreicht ist (τ_{ignOHmax}) beziehungsweise der Wert, bei dem eine Gerade angelegt an den steilsten Gradienten des $^{\bullet}$OH-Konzentrationsverlaufes die Zeitachse schneidet ($\tau_{\mathrm{ignOHgrad}}$). In der Modellierung kann zwischen zwei Reaktortypen gewählt werden, welche beide ein Realgasverhalten abbilden. Zum einen "Real isochor", bei dem das Volumen konstant ist, und "Real isobar", bei dem der Druck konstant ist. In dieser Arbeit wird der isobare Reaktortyp verwendet, die Unterschiede zwischen beiden Typen werden analysiert, allerdings ist der Einfluss im Bezug auf die Zündverzugszeiten vernachlässigbar.

Um Schmieröl in der Modellierung zu berücksichtigen, wird ein Ersatzstoff benötigt, der das Verhalten von realem Öl gut abbilden kann. Die genaue Zusammensetzung von Marine-Schmieröl wird von den Herstellern nicht herausgegeben. Die Modellbildung für den Ersatzstoff basiert deshalb auf bestehenden Arbeiten. C_{16}-C_{18} n-Alkane sind geeignete Kohlenwasserstoffe, um Schmieröl zu modellieren. Auch zeigt sich, dass die Additivierung des Öls bei der Betrachtung reaktionskinetischer Mechanismen vernachlässigt werden kann. Bei einer Ölkonzentration im Luft-Kraftstoffgemisch von bis zu 1 % ist n-Hexadecan ein geeigneter Ersatzstoff. Bei deutlich höheren Konzentrationen kann mit der Beimischung eines C_{18} n-Alkans die Übereinstimmung verbessert werden. Für diese Arbeit wurde durchgehend n-Hexadecan als Ersatzstoff verwendet. Es zeigt sich, dass die Konzentration des Schmieröls im relevanten Zündbereich kleiner als 1 % ist, weshalb mit dieser Annahme eine gute Übereinstimmung erzielt wird. Bei der Berechnung von Zündverzugszeiten von verschiedenen Zusammensetzungen stellt sich heraus, dass mit C_{18} n-Alkanen eine signifikante Erhöhung der Rechenzeit einhergeht. Während mit n-Hexadecan die Berechnung in wenigen Sekunden abgeschlossen wird, dauert diese bei den längerkettigen Kohlenwasserstoffen mehre Stunden bis Tage.

Für die reaktionskinetische Untersuchung werden Zündverzüge bei einer Variation von Druck, Temperatur, Kraftstoffqualität, Kraftstoff-Luft-Verhältnis, Abgasrückführungsverhältnis und Schmierölkonzentration berechnet. Für die Zündung zeigt sich, dass sich die Kraftstoffqualität und das Abgasrückführungsverhältnis zwar auf die Zündverzugszeit auswirken, jedoch der Einfluss für die Vorentflammung relativ gering ist. Im Vergleich dazu reicht bereits eine geringe Menge an Schmieröl aus, um die Zündverzugszeit extrem zu reduzieren. Ein Druckanstieg führt ebenfalls zu einer reduzierten Zündverzugszeit, allerdings nicht in dem Maße, wie es die Beimengung von Öl tut. Bei für den Motorbetrieb typischen Drücken und Temperaturen sind die Zündverzugszeiten deutlich länger als selbst bei den niedrigen Drehzahlen von unter 100 Umdrehungen pro Minute an Zeit zur Verfügung stehen würde. Mit Schmierölbeimischung ist eine Zündung selbst bei niedrigen Temperaturen und Drücken möglich. Es zeigt sich, dass eine Vorentflammung ohne vorhandenes Öl nicht möglich ist. Der Gradient der Zündverzüge über der Temperatur ist bis ca. 850 K sehr steil. Eine Zündung ist deshalb stark temperaturabhängig.

Zur Bewertung, wie sich eine Flamme nach einer vorhergegangenen Vorentflammung ausbreitet, werden laminare Flammengeschwindigkeiten berechnet.

Es wird gezeigt, wie sich unterschiedliche Schmierölbeimischungen auswirken. Zusätzlich variiert wurden das Luft-Kraftstoffverhältnis, der Druck und die Temperatur. Es zeigt sich, dass die laminare Flammengeschwindigkeit bei 100 % Schmierölersatzstoff über dem kompletten variierten Bereich höher ist als bei Methan oder Methan mit Ölbeimischung. Konzentrationen von Öl über 5 % sind, in der für die Zündung relevanten Gasphase, nicht realistisch. Bei dieser Größenordnung ist der Einfluss nahezu zu vernachlässigen. Eine Flamme wird sich mit Schmieröleinfluss ähnlich schnell ausbreiten wie ohne.

In den reaktionskinetischen Untersuchungen zeigt sich, dass Schmieröltropfen die Ursache für die Vorentflammungen sind. Um zu verstehen, wie das Phänomen auftritt und welche Konzentrationen des Öls auftreten, wird ein Tropfenverdampfungsmodell als Teil des Vorentflammungsmodells implementiert. Für die Modellbildung wird auf Gleichungen zurückgegriffen, die auch bei der Spraymodellierung zum Einsatz kommen. Es wird gezeigt, wie bereits verschiedene Datenquellen die Modellgenauigkeit beeinflussen. Die thermodynamischen Eigenschaften für die Flüssigphase werden einer Datenbank entnommen, die der Gasphase werden mit Hilfe von Cantera und dem Reaktionsmechanismus berechnet.

Das Tropfenverdampfungsmodell wird gegen Messreihen aus der Literatur validiert. Hierfür werden Veröffentlichungen gewählt, bei denen Tropfenverdampfungen bei unterschiedlichsten Randbedingungen aufgezeichnet wurden. Das in dieser Arbeit entwickelte Modell stimmt gut mit allen Messungen aus der Literatur überein. Es zeigt sich, dass Temperatur-, Druck- und Strömungseinflüsse gut abgebildet werden können. Es wird analysiert welche Auswirkung die Tropfengröße auf die Verdampfung und das komplette Vorentflammungsmodell hat. Auch werden die Grenzen dieses Modellansatzes aufgezeigt und diskutiert.

Für das Gesamtmodell wird die Tropfenverdampfung mit der Reaktionskinetik gekoppelt. Dem Tropfenverdampfungsmodell werden die Eingangsgrößen Druck- und Temperaturverlauf sowie die Startrandbedingungen der Schmieröltropfen übergeben. Im ersten Schritt werden die Temperaturen im Schmieröltropfen und in der Gasphase sowie die Konzentration der einzelnen Spezies in der Gasphase kurbelwinkelaufgelöst berechnet. Im zweiten Schritt werden mit der Reaktionskinetik Zündzeitpunkte bestimmt. Mit der Verdampfungs- und Zündzeit wird im Modell der Zeitpunkt des Vorentflammunsgbginns vorhergesagt. In einer Sensitivitätsanalyse wird untersucht, wie sich verschiedene Parameter auf das Ergebnis auswirken. Variiert wird hierbei die Anströmung des Tropfens, die initiale Tropfengröße, das Luft-Kraftstoff-Verhältnis im Brennraum und die Temperaturkurve während der Verdichtung.

Das Vorentflammungsmodell wird gegen umfangreiche Messergebnisse validiert. Die Messungen werden von einem Forschungspartner an der University of Applied Sciences and Arts Northwestern Switzerland (FHNW) an einem optisch zugänglichen Prüfstand durchgeführt. Dieser eignet sich für die Analyse von Vorentflammungseffekten bei niedrigen Drehzahlen. Es lassen sich flexibel verschiedene motornahe Randbedingungen wie Druck, Temperatur, Strömungszustände und Luft-Kraftstoff-Verhältnis einstellen. Einzelne Schmieröltropfen können mit einem extra für diesen Anwendungsfall entwickelten Injektor in den Brennraum eingebracht werden. Die Detektion der Vorentflammungen erfolgt durch eine Kombination aus Schlierenaufnahmen und der Aufnahme der Chemielumineszenz des $^{\bullet}$OH Radikals mit High-Speed-Kameras. Anhand der optischen Aufnahmen kann der genaue Zeitpunkt des Vorentflammungsbeginns ermittelt werden.

In Abstimmung mit dem Schiffsmotorenhersteller Winterthur Gas & Diesel Ltd. (WinGD) werden motorrelevante Randbedingungen identifiziert. Für die Messungen werden drei verschiedene Verdichtungskurven verwendet. Für jede Verdichtungskurve wird wiederum das Luft-Kraftstoff-Verhältnis variiert. Bei allen Betriebspunkten wird eine Start Of Injection (SOI) Variation, was der Zeitpunkt der Schmieröleinbringung darstellt, durchgeführt. Für jeden SOI werden ca. 30 Versuche vermessen, um die Schwankung der Zündzeitpunkte messen zu können. Die Randbedingungen des Schmieröls wurden analog zu einem realen Schiffsmotor am Prüfstand eingestellt.

Es wird eine Messdatenanalyse aller gemessenen Betriebspunkte durchgeführt. Es zeigt sich, dass das Luft-Kraftstoffverhältnis eher eine untergeordnete Rolle für den Beginn der Vorentflammung spielt. Auch der Zeitpunkt, bei dem das Schmieröl in den Brennraum eingebracht wird, ist, wenn es nicht kurz vor TDCF eingespritzt wird, zu vernachlässigen. Da der Brennraum nicht vollständig optisch erfasst werden kann, kommt es vor allem bei frühen SOIs zu leichten Auswertefehlern. Diese äußern sich in einer minimal später detektierten Vorentflammung, da diese teilweise außerhalb des sichtbaren Bereichs beginnt und erst wenn die Flammenfront in diesen eintritt, als Zündung ausgewertet wird.

Es zeigt sich in den Messdaten, dass eine höhere Temperatur in der Verdichtung eine deutlich frühere Zündung auslöst.

Alle zur Verfügung stehenden Messergebnisse werden mit denen des phänomenologischen Vorentflammungsmodells verglichen. Es zeigt sich, dass das Modell in allen validen Betriebspunkten sehr gut mit den Messergebnissen übereinstimmt. Auch die hohe Temperatursensitivität des Vorentflammungsphänomens kann vom Modell gut abgebildet werden. Bei dem gewählten Modellansatz ist es normalerweise üblich, Abstimmparameter zu verwenden. Das entwickelte Modell basiert jedoch auf physikalischen Annahmen und kommt ohne diese aus.

Ebenfalls wurde das Modell gegen Messwerte eines Schiffsmotors von WinGD validiert. Hierfür wurde eine Temperaturvariation der Kolbenunterseite verwendet. Diese Temperatur ist bei einem klassichen 4-Takt Motor vergleichbar mit der Ladelufttemperatur. Die Temperaturdifferenz der zwei Betriebspunkte beträgt nur 5.4 K, was den Unterschied zwischen dem Betrieb bei Standardbedingungen und bei tropischen Bedingungen darstellt. Während bei Standardbedingungen keine Vorentflammungen auftreten, sind diese bei den um 5.4 K erhöhten tropischen Bedingungen in jedem der 100 gemessenenen Zyklen zu sehen. Das Vorentlammungsmodell kann den Beginn der Vorentflammung perfekt vorhersagen und die berechneten Ergebnisse stimmen gut mit den Messungen des realen Motors überein.

Es wird gezeigt, dass die Ergebnisse des Vorentflammungsmodells sehr gut mit den Messungen, sowohl am Prüfstand als auch am Schiffsmotor, übereinstimmen. Mögliche zukünftige Forschungsthemen, die sich durch diese Arbeit aufgetan haben, könnten die Betrachtung der Flammausbreitung nach einer vorhergehenden Vorentflammung sein. Auch könnte untersucht werden, ob es sich überhaupt um eine klassische Flammenausbreitung handelt oder bei den sehr mageren Gemischen eher um eine Volumenzündung oder einer Mischung aus beidem. Im Marinebereich gewinnen CO_2 reduzierte Kraftstoffe wie Ammoniak oder Wasserstoff immer mehr an Bedeutung. Eine Erweiterung des Modells um diese Kraftstoffe kann für die zukünftige Forschung interessant sein.

Abstract

In order to comply with the Paris Agreement on climate protection and limit the average temperature increase to less than 1.5 °C, CO_2 emissions must also be reduced in the area of large engines. To achieve this goal, the use of CO_2-reduced fuels such as ammonia, hydrogen, and other synthetic fuels is already being prepared. At least in the transition phase, Liquefied Natural Gas (LNG) is an economic and ecological compromise. Therefore, this fuel is increasingly used in large two-stroke engines of container ships. For marine Dual Fuel (DF) Gas engines, unwanted pre-ignition is a fundamental issue when considering the combustion process. The underlying mechanism of this phenomenon is lubricating oil droplets that ignite in the combustion chamber and lead to thermal and mechanical stresses, causing damage to engine components.

Extensive testing, especially in large engines, is costly. For this reason, understanding the pre-ignition phenomenon and developing a predictive simulation model is essential. In order to minimize computation times, an attempt is made to represent the phenomenon using a 0D/1D approach. For the model validation, measurements are performed at a highly flexible optically accessible test facility at the FHNW.

Reaction kinetics studies in the form of ignition delay times are carried out to identify the causes of pre-ignition in gas engines. The main engine influencing factors are varied, such as pressure, temperature, air-fuel ratio, different fuel qualities, and lubricating oil quantity. It is shown that pre-ignition is not possible without the presence of oil.

A combination of droplet evaporation and reaction kinetics is chosen to develop a predictive model. The submodel of droplet evaporation is based on the equations of Abramzon and Sirignano, which are also used in spray modeling. The material properties for the liquid and gas phase are determined using transport data of a reaction mechanism and values from the National Institute of

Standards and Technology (NIST) database. The droplet evaporation model is validated against literature for different temperatures, pressures, and flow conditions and showed excellent agreement.

The submodel of the droplet evaporation delivers a time-resolved temperature course and course of the lubricating oil concentration in the gas phase. With these boundary conditions for the second submodel, the ignition timing of the droplets in the surrounding air-fuel mixture is determined with reaction kinetic calculations. With this simulation method, it is possible to determine and predict the ignition onset, i.e., the start of pre-ignition.

The phenomenological pre-ignition model is validated by carrying out an extensive measurement campaign in which the timing of the lubricating oil application is varied, and the ignition is evaluated optically. Measurements are made at temperatures of 750 K, 800 K, and 850 K at the end of compression. The air-fuel ratio variation is performed and optically evaluated for each temperature curve. The simulation results of the pre-ignition model fit very well with the measured values. It is shown that the air-fuel mixture has a negligible influence on pre-ignition timing. This should not be confused with flame propagation after pre-ignition, as, in this case, the air-fuel ratio significantly influences flame propagation. The analyses show that the phenomenon of pre-ignition is very temperature-sensitive. Even minor temperature differences have an extreme influence on pre-ignition.

The model is also validated against measured values from a marine DF gas engine. Measurements of a piston underside temperature variation, which can be compared with a charge air temperature variation, are provided by WinGD. From these measurements, no pre-ignition is seen at standard conditions, but at tropical conditions, where the piston underside temperature is 5.4 K higher, pre-ignition is visible in each of the 100 cycles. The model can determine the onset of pre-ignition very well. Furthermore, analyses are performed on the large engine concerning pre-ignition and flame propagation. Above all, the high-temperature sensitivity of the pre-ignition phenomenon became apparent again in this analysis. Flame propagation after pre-ignition was analyzed by calculating laminar burning velocities, including the influence of Exhaust Gas Recirculation (EGR). However, the investigations leave questions unanswered, as flame propagation after pre-ignition requires further in-depth research.

In summary, this thesis presents a phenomenological pre-ignition model whose simulation results agree very well with the available measurement results of the optically accessible test facility and the measurements of the large marine engine. Furthermore, the model is based on purely physical and reaction kinetic assumptions and does not require any tuning parameters, which is a unique characteristic of this model approach.

Contents

List of Figures

List of Tables

Acronyms

0D	Zero-Dimensional
1D	One-Dimensional
3D	Three-Dimensional
AFER	Air-Fuel Equivalence Ratio (λ)
ASM	Abramzon-Sirignano Model
BMEP	Brake Mean Effective Pressure
BMWK	Federal Ministry for Economic Affairs and Climate Action
CA	Crank Angle
CFD	Computational Fluid Dynamics
CNG	Compressed Natural Gas
CORNET	Collective Research Networking
DF	Dual Fuel
DNS	Direct Numerical Simulation

EGR	Exhaust Gas Recirculation
FHNW	University of Applied Sciences and Arts Northwestern Switzerland
FKFS	Forschungsinstitut für Kraftfahrwesen und Fahrzeugmotoren Stuttgart
Flex-OeCoS	Flexibility regarding Optical engine Combustion diagnostics and/or Sensing
FVV	FVV e. V. // Science for a moving society
HCCI	Homogeneous Charge Compression Ignition
HT	High Temperature
ICE	Internal Combustion Engine
IFS	Institut für Fahrzeugtechnik Stuttgart
IGN	Ignition
ITFE	Institute for Thermal and Fluid Engineering
KCS	Knock Control System
LLNL	Lawrence Livermore National Laboratory
LNG	Liquefied Natural Gas
LSODA	Livermore Solver for Ordinary Differential Equations
LT	Low Temperature

MAX	Maximum Value
MEAN	Mean
MED	Median
MGO	Marine Gasoil
MIN	Minimum Value
MMT	Measurement
NG	Natural Gas
NIST	National Institute of Standards and Technology
NTC	Negative Temperature Coefficient
ODE	Ordinary Differential Equation
QD	Quasi-Dimensional
RCM	Rapid Compression Machine
RPM	Revolutions Per Minute
SD	Standard Deviation
SI	Spark Ignition
SIM	Simulation
SOI	Start Of Injection
SOIgn	Start Of Ignition

TDCF	Top Dead Center Firing
WinGD	Winterthur Gas & Diesel Ltd.

Symbols

	Chemical Species
C_2H_4	Ethylene
C_2H_6	Ethane
C_3H_8	Propane
C_4H_{10}	Butane
C_5H_{12}	Pentanes
C_7H_{16}	n-Heptane
C_8H_{10}	m-Xylene
$CaCO_3$	Calcium Carbonate
CH_4	Methane
CO_2	Carbon Dioxide
H_2O	Dihydrogen Oxyde
N_2	Nitrogen Molecule
$nC_{12}H_{26}$	n-Dodecane
$nC_{16}H_{33}$	n-Hexadecyl
$nC_{16}H_{34}$	n-Hexadecane
$nC_{18}H_{38}$	n-Octadecane
NO	Nitric Oxyde
NO_2	Nitrogen Dioxyde

NO_x	Nitrogen Oxydes (mostly NO and NO_2)
O_2	Oxygen Molecule
$^{\bullet}OH$	Hydroxyl Radical
SO_x	Sulfur Oxydes

Greek Letters

α	Weighting Parameter For Gas-Vapour Mixture	–
β	Evaporation Parameter	–
κ	Thermal Conductivity	$\frac{\mathrm{W}}{\mathrm{m\,K}}$
λ	Air–Fuel Equivalence Ratio	–
η	Dynamic Viscosity	Pa s
ν	Kinematic Viscosity	$\frac{\mathrm{m}^2}{\mathrm{s}^{-1}}$
ρ	Density	$\frac{\mathrm{kg}}{\mathrm{m}^3}$
τ	Ignition Delay Time	s

Indices

atm	Atmospheric
b	Boiling
c	Critical
classic	Classic
d	Droplet
EGR	Exhaust Gas Recirculation
EOC	At The End Of Compression
ev	Evaporation

f	Forward
g	Ambient Gas
gen	Generated
ign	Ignition
in	Input
k	Species
L	Laminar
liq	Liquid
M	Mass
max	Maximum
mix	Gas-Vapour Mixture
new	New
OHgrad	Ignition Criterion $^{\bullet}$OH Gradient
OHmax	Ignition Criterion Maximum $^{\bullet}$OH Concentration
oil	Oil
old	Previous Step
out	Output
PUS	Piston Underside
s	Droplet Surface
sat	Saturation
st	Stoichiometric
T300	Ignition Criterion $\Delta T = 300\,K$
T400	Ignition Criterion $\Delta T = 400\,K$
T	Thermal
v	Vapour

vap	Vaporization
wb	Wet-Bulb

	Latin Letters	
A	Arrhenius Frequency Factor	–
a	NASA Polynomial Coefficient	–
A	Antoine Equation Coefficent	–
B	Arrhenius Exponent	$\frac{\mathrm{MJ}}{\mathrm{kg}}$
b	Temperature Exponent	–
B	Antoine Equation Coefficent	–
B_{M}	Spalding Mass Transfer Number	–
b	NASA Polynomial Integration Constant	–
B_{T}	Spalding Thermal Energy Transfer Number	–
C	Antoine Equation Coefficent	–
C_{p}°	Heat Capacity (isobaric) At Standard State	$\frac{\mathrm{J}}{\mathrm{K}}$
c_{p}	Specific Heat Capacity (isobaric)	$\frac{\mathrm{J}}{\mathrm{kg\,K}}$
c_{v}	Specific Heat Capacity (isochoric)	$\frac{\mathrm{J}}{\mathrm{kg\,K}}$
D	Diameter	m
D	Diffusion Cefficient	$\frac{\mathrm{m}^2}{\mathrm{s}}$
E_{a}	Temperature Exponent	J
F	Correction Factor	–
G	Corection Factor For Energy Transfer Reduction	–
H	Enthalpy	J
h	Specific Enthalpy	$\frac{\mathrm{J}}{\mathrm{kg}}$
H°	Enthalpy At Standard State	J

k	Reaction Rate Constant	$\frac{\mathrm{M}^{\mathrm{i}}}{\mathrm{s}}$
Le	Lewis Number	–
L_{st}	Stoichiometric Air-Fuel Mixture	–
M	Molar Mass	$\frac{\mathrm{kg}}{\mathrm{mol}}$
m	Mass	kg
n	Rotational Speed	min^{-1}
Nu	Nusselt Number	–
Nu^*	Modified Nusselt Number	–
p	Pressure	Pa
Pr	Prandtl Number	–
Q	Heat Flux	W
R	Molar Gas Constant	$\frac{\mathrm{J}}{\mathrm{K\,mol}}$
r	Radius	m
Re	Reynolds Number	–
s	Velocity	$\frac{\mathrm{m}}{\mathrm{s}}$
Sc	Schmidt Number	–
Sh	Sherwood Number	–
Sh^*	Modified Sherwood Number	–
S°	Entropy At Standard State	$\frac{\mathrm{J}}{\mathrm{K}}$
T	Temperature	K
t	Time	s
U	Internal Energy	J
u	Specific Internal Energy	$\frac{\mathrm{J}}{\mathrm{kg}}$
v	Velocity	$\frac{\mathrm{m}}{\mathrm{s}}$
V	Volume	m^3

X	Mole Fraction	$\frac{\mathrm{mol}}{\mathrm{mol}}$
Y	Mass Fraction	$\frac{\mathrm{kg}}{\mathrm{kg}}$

1 Introduction

In order to achieve the ambitious 1.5 °C target of the Paris Climate Agreement, appropriate actions must be taken in all sectors. Hydrocarbons are currently not substitutable as an energy source in the transport and heavy-duty sector due to their higher energy density than batteries. To reduce CO_2 emissions, natural gas is a suitable option due to its better hydrogen-to-carbon ratio than diesel or gasoline. For large engines, lean premixed gas/DF combustion is an attractive solution to meet future emission regulations. This combustion process significantly reduces CO_2, particle, NO_x, and SO_x emissions with an efficiency comparable to diesel combustion. Therefore, especially in the field of marine engines, natural gas is becoming increasingly important as a fuel. However, unwanted pre-ignition, induced by lubricating oil droplets, can occur during the operation of these engines. This phenomenon leads to high peak pressures and can damage components in the worst case.

Extensive measurement campaigns, especially in a large engine environment, are very costly. Three-Dimensional (3D) CFD simulations also require long computing times and are complex and expensive. In order to keep the costs within limits and still generate a good prediction accuracy for engine development, a phenomenological pre-ignition model is developed. It is based on Zero-Dimensional (0D)/One-Dimensional (1D) and Quasi-Dimensional (QD) modeling methods. For the model validation, measurements are performed at an optically accessible test facility at the FHNW. The measurement results are compared with the simulation. This thesis is based on the research project [106].

First, the pre-ignition phenomenon is introduced, and the differences between pre-ignition in gasoline engines in passenger car applications and those in DF gas-engines are elaborated. Then, modeling fundamentals are presented, consisting of reaction kinetics and droplet evaporation. Next, an investigation of the reaction kinetics is shown to analyze the pre-ignition process. The methodology and model setup are discussed, and the structure of the model and its definitions are explained. The subsequent results of these investigations are divided into dominant and secondary effects. In order to roughly estimate the flame propagation after pre-ignition, calculations in terms of laminar burning velocities are performed, evaluated, and analyzed. The modeling of pre-ignition is divided into two submodel aspects, droplet evaporation, and reaction kinetics. The droplet evaporation model is validated against measurements from the literature. Next, a sensitivity analysis is performed to investigate the influence of the different model parameters.

The overall pre-ignition model is validated against a comprehensive measurement campaign at conditions relevant to real operation. Finally, the calculation results of the model are compared to large engine measurements, and further investigations concerning mixture inhomogeneities are carried out. The thesis is summarized, and an outlook for future research is given.

2 Fundamentals and State of the Art

2.1 Pre-Ignition in Gasoline Engines

Pre-ignition is a autoignition phenomenon most frequently observed in turbocharged gasoline engines. Especially operating points that are in the full load range at low engine speeds are susceptible to early ignition [48]. As researched by Dahnz, Han and Magar [24], there are a variety of causes for pre-ignition that are more likely and less likely to occur. Pre-ignition at hot spots (local temperature rise) and ignition at hot particles and deposits are considered improbable but conceivable causes. The phenomenon is most likely caused by oil droplets detached from the cylinder wall. In this case, the oil is diluted by the fuel jet. The viscosity and surface tension of the mixture decreases and detachment may occur due to the changed physical properties. This interaction of fuel and oil must therefore be present in order to trigger pre-ignition. Schweizer et al. [90] confirms this thesis for an engine operation with Compressed Natural Gas (CNG), where no pre-ignitions are observed. Even when the lubricating oil is injected directly into the cylinder, no pre-ignition can be observed.

Further studies show that the fuel influences early ignitions [27]. Also, ignition at particles flying around in the combustion chamber or at solid deposits detaching from the wall plays a role in highly boosted Spark Ignition (SI) gasoline engines [47]. Furthermore, some studies show an influence of individual components of the lubricating oil on the pre-ignition [38]. In particular, calcium in the form of $CaCO_3$ is the focus of investigations [74].

There are different strategies to avoid pre-ignition in SI gasoline engines. The variant caused by deposits on the spark plug and exhaust valve, understood as a pre-ignition induced by heavy knocking, is not a major problem. This mechanism can be controlled by the Knock Control System (KCS). Pre-ignition caused by deposits in the combustion chamber can be detected by measuring the frequency and timing of knocking that occurs in the early phase of pre-ignition. According to Mogi et al. [73], fast enrichment of the air/fuel mixture can prevent pre-ignition.

2.2 Pre-Ignition in Large Dual Fuel Gas-Engines

Pre-ignition in large DF gas engines has received little attention in the literature. Also, there are only a few observations of this phenomenon in DF engines [56]. According to Zaccardi and Serrano [115], the causes of early ignition presented in section 2.1 can not be compared with the ones of the engine technology investigated in this thesis.

Hot spots may well occur in the exhaust valve area or at the hot prechamber if the engine is equipped with one. However, hot spots at the spark plug, as it is the case with SI engines, cannot occur due to the lack of a spark plug, so the primary mechanism does not apply.

Deposits or hot particles flying around in the combustion chamber are often cited as the reason for pre-ignition. The main component of the fuel methane is known to burn relatively soot-free. Despite the small amount of diesel used for pilot injection, no massive deposits or particles are to be expected in gas engines. This cause of undesired ignition also seems unlikely.

In direct-injection gasoline engines, the fuel jet may impact directly on the wall. Fuel on the wall leads to dilution of the lubricating oil and droplets can detach from there due to the changed physical properties and ignite in the combustion chamber. This wall interaction of the spray can also lead to liquid fuel deposits, resulting in locally rich areas with a shorter ignition delay time. If the fuel has Negative Temperature Coefficient (NTC) behavior, a cooler wall can have an even more negative effect on ignition. DF engines, however, work with gaseous fuel that is injected into the combustion chamber through ports. Wall interaction can therefore be ruled out. The diesel pilot also does not come into contact with the wall, as it burns directly with a diffusion flame.

The most likely cause of pre-ignition in gas engines is induced by lubricating oil. This mechanism has been investigated in several studies [113, 112, 117, 34]. However, the source and the way the lubricating oil enters the combustion chamber still leaves questions unanswered. In the case of large two-stroke engines, the amount of oil droplets in the intake air is not negligible. Furthermore, these engine types have oil injection nozzles called oil quills. Lubricating oil is sprayed tangentially onto the cylinder wall through several radially arranged injectors to ensure lubrication of the piston-liner contact. Injection occurs when the exhaust valve closes and long before the piston passes the oil quills in upward motion [60]. Depending on the injection strategy, the amount of oil can also be fed into the ring package and under the piston in addition to being introduced above.

Pre-ignition in gas engines also seems to be very temperature sensitive due to lubricating oil. The compression end temperature is the decisive factor here [113].

The above-mentioned causes thus result in several operating strategies for this type of engine. One method is to reduce the amount of lubricating oil in the cylinder, but to a level where damage or greatly increased wear can be ruled out. The final compression temperature could also be reduced. However, depending on the combustion process, there must still be a sufficient temperature for the diesel pilot combustion to start. Preventing or inhibiting the propagation of a flame after a previous pre-ignition is also a possibility. Cooled EGR to reduce the flame speed would be conceivable here.

2.3 Reaction Kinetic Fundamentals

In this section, the essential reaction kinetic basics are briefly explained. On the one hand, the important equations for modeling chemical reactions are discussed, and a reaction mechanism's essential function and components are described. On the other hand, the zero-dimensional reactor is introduced as it plays an essential role in this thesis. However, the focus of this section is only a short summary of the most important aspects and does not claim to be complete. The interested reader can find further information in countless works in the literature [98, 93, 18, 100, 4].

2.3.1 Elements and Species Thermodynamics

Chemical reactions are broken down into elementary reactions and assembled into a reaction mechanism. As shown schematically in fig. 2.1, a reaction mechanism includes transport and thermodynamic data of the included species in addition to the reactions and reaction rates. A reaction mechanism makes it possible, for example, to extrapolate for ignition delay times outside the values validated by measurements. The following section discusses the three components of a reaction mechanism and roughly explains how they are used in the modeling.

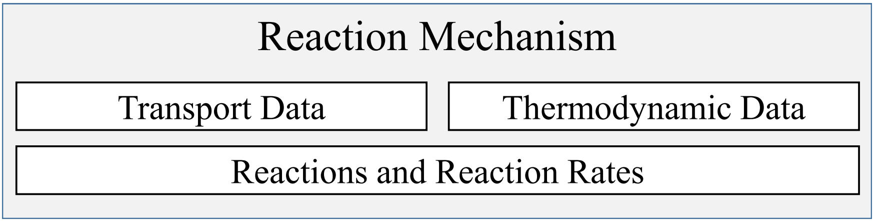

Figure 2.1: Schematic structure of a reaction mechanism.

Transport Data

Transport data are needed in this thesis for the calculation of diffusion coefficients. Diffusion occurs when there are differences in the concentrations of a species in a mixture. In the modeling, two transport models are implemented which are possible for the calculation of gas mixtures. The first model is a multicomponent model based on the findings of Dixon-Lewis [29]. The mixture average rule is applied to the second model which is much more simplistic and therefore less computationally intensive.

Table 2.1 lists the gas transport parameters used. The corresponding parameters are listed for each species that can be calculated from the respective reaction mechanism. Further parameters like the ”acentric-factor”, ”dispersion-coefficient” and ”quadrupole-polarizability” can be specified, but they do not appear in the reaction mechanism used in this thesis and therefore will not be further discussed here.

Table 2.1: Species transport model parameters in reaction mechanisms.

Parameter	Description	Unit
geometry	Geometry of the molecule: ”atom”, ”linear”, or ”nonlinear”	string
diameter	Lennard-Jones collision diameter	[Å]
well-depth	Lennard-Jones well depth	[K]
dipole	Permanent dipole moment	[Debye]
polar	Dipole polarizability	[Å^3]
rot_relax	Rotational relaxation collision number at 298 K	[−]

Thermodynamic Data

For modeling the thermodynamic data for each species in the gas mixture, the NASA 7-coefficient polynomial parameterization [69] is used. These are usually created by a fit of experimental data.

In this way, the thermodynamic properties of the reference state of the species, such as the heat capacity C_p° (eq. (2.1)), the H° (eq. (2.2)) and the S° (eq. (2.3)) can be calculated as a function of temperature using a polynomial for each species.

$$\frac{C_\mathrm{p}^\circ(T)}{R} = a_1 + a_2 T + a_3 T^2 + a_4 T^3 + a_5 T^6 \tag{2.1}$$

$$\frac{H^\circ(T)}{RT} = a_1 + \frac{a_2}{2} T + \frac{a_3}{3} T^2 + \frac{a_4}{4} T^3 + \frac{a_5}{5} T^4 + \frac{b_1}{T} \tag{2.2}$$

$$\frac{S^\circ(T)}{R} = a_1 \ln T + a_2 T + \frac{a_3}{2} T^2 + \frac{a_4}{3} T^3 + \frac{a_5}{4} T^4 + b_2 \tag{2.3}$$

The seven coefficients a_0 to a_6 are given in two temperature regions in the reaction mechanisms used. For the sake of completeness, it is referred to the NASA polynomial parametrization with nine coefficients [68], a newer variant where two additional terms are added in each temperature region, and any number of temperature regions can be specified in the parametrization. However, only reaction mechanisms based on the NASA-7 approach are used in this thesis.

Reactions and Reaction Rates

In order to calculate the rate of chemical reactions and the activation energy, Svante Arrhenius introduced an equation in 1889 that describes the dependence of the rate constant k_f on the temperature [5, 6, 59, 13, 76]:

$$k_\mathrm{f} = A\mathrm{e}^{\frac{-E_\mathrm{a}}{RT}}. \tag{2.4}$$

A is the pre-exponential factor which is also called the frequency factor, since it refers to the collision frequency of the species involved in the reaction. The term $\mathrm{e}^{\frac{-E_\mathrm{a}}{RT}}$ describes the probability that a collision leads to a reaction. E_a is the activation energy and R is the molar gas constant.

Assuming that A is not temperature dependent, the activation energy can be calculated by rearranging the Arrhenius equation by measuring the two rate constants k_1 and k_2 and the two temperatures T_1 and T_2 of the same reaction [75]:

$$E_\mathrm{a} = R \ln \frac{k_2}{k_1} \frac{T_1 T_2}{T_2 - T_1}. \tag{2.5}$$

The original Arrhenius equation was later extended by a temperature-dependent pre-exponential factor. This equation is known as the modified Arrhenius equation [58]:

$$k_\mathrm{f} = AT^b\mathrm{e}^{\frac{-E_\mathrm{a}}{RT}}. \tag{2.6}$$

As an example for a calculation of the forward rate constant, the reaction of $\mathrm{nC_{16}H_{34}}$ with an $^\bullet\mathrm{OH}$ radical to $\mathrm{H_2O}$ and $\mathrm{nC_{16}H_{33}}$ is shown:

$$^\bullet\mathrm{OH} + \mathrm{nC_{16}H_{34}} \underset{k_\mathrm{f}}{\overset{k_\mathrm{f}}{\rightleftharpoons}} \mathrm{H_2O} + \mathrm{nC_{16}H_{33}}. \tag{2.7}$$

This reaction is given in the reaction mechanism POLIMI_TOT_NOx_1412 [82, 33, 35, 21] used among others in this thesis as Reaction 12660 as follows:

reaction('OH + NC16H34 => H2O + NC16H33', [1.198e+07, 2.0, -2259.83])

By substituting the successive numerical values for A, b and E_a which are specified in the exemplary line above, the forward rate constant is derived with:

$$k_\mathrm{f} = 1.198 \cdot 10^7 \cdot T^2 \cdot \mathrm{e}^{\frac{2259.83\,kcal}{RTmol}} . \tag{2.8}$$

The forward rate constant thus depends only on the temperature and the molar gas constant R.

2.3.2 Zero-Dimensional Reactor

The zero-dimensional reactor is introduced at this point. For this purpose, the noteworthy equations and descriptions from Cantera [46] are explained and the unique aspects are presented. The reactor consists of an extensive thermodynamic control volume V. All boundary conditions, such as pressure, temperature and species concentration, are homogeneously distributed. The system is time-resolved to represent transient state changes due to chemical reactions. However, it is always in thermodynamic equilibrium, in contrast to the chemical state, which can change with time.

The reactor can interact with the environment through compression and expansion work, heat transfer, mass transfer, and surface interaction. However, these functions have not been used and will not be discussed here.

In the reactor, conservation of mass and species over time applies. The reactor volume changes due to the movement of one or more walls. The discussion and description of these equations will be omitted here.

The energy equation is solved by default, but can be deactivated. The energy conservation equations change depending on the reactor type used. These equations are briefly described for each reactor type in the following.

Standard Reactor

The equation for the total internal energy for the standard reactor is described by the first law of thermodynamics for open systems:

$$\frac{\partial U}{\partial t} = -p\frac{\partial V}{\partial t} + \dot{Q} + \sum_{\mathrm{in}} \dot{m}_{\mathrm{in}} h_{\mathrm{in}} - h \sum_{\mathrm{out}} \dot{m}_{\mathrm{out}}. \tag{2.9}$$

The net heat input of the open system is represented by $\dot{Q}$ and $\dot{m}_{\mathrm{in}}$ and $\dot{m}_{\mathrm{out}}$ are the inflowing and outflowing mass flows from the system, respectively.

Constant Pressure Reactor

The volume of the reactor changes as a function of time in order to keep the pressure constant. As a state variable, the total internal energy U is replaced by the total enthalpy H:

$$H = U + pV, \tag{2.10}$$

$$\frac{\partial H}{\partial t} = \frac{\partial U}{\partial t} + p\frac{\partial V}{\partial t} + V\frac{\partial p}{\partial t}. \tag{2.11}$$

Since for the constant pressure reactor the pressure change over time is zero ($\frac{\partial p}{\partial t} = 0$), inserting eq. (2.11) into the energy equation eq. (2.9) yields:

$$\frac{\partial H}{\partial t} = \dot{Q} + \sum_{\mathrm{in}} \dot{m}_{\mathrm{in}} h_{\mathrm{in}} - h \sum_{\mathrm{out}} \dot{m}_{\mathrm{out}}. \tag{2.12}$$

Ideal Gas Reactor

For the ideal gas reactor, the total internal energy U is replaced by the temperature T as a state variable. Since all species refer to the same gas constant, there is no need to differentiate between internal energy U and temperature T. The total internal energy U is formulated as a function of the mass fractions Y and temperature T in the case of the ideal gas:

$$U = m \sum_{\mathrm{k}} Y_{\mathrm{k}} u_{\mathrm{k}} (T), \tag{2.13}$$

$$\frac{\partial U}{\partial t} = u\frac{\partial m}{\partial t} + mc_\mathrm{v}\frac{\partial T}{\partial t} + m\sum_\mathrm{k} u_\mathrm{k}\frac{\partial Y_\mathrm{k}}{\partial t}, \tag{2.14}$$

with u_k as specific internal energy of the species k. The energy equation is now obtained by substituting the corresponding derivatives:

$$\begin{aligned} mc_\mathrm{v}\frac{\partial T}{\partial t} = -p\frac{\partial V}{\partial t} + \dot{Q} + \sum_\mathrm{in}\dot{m}_\mathrm{in}\left(h_\mathrm{in} - \sum_\mathrm{k} u_\mathrm{k}Y_\mathrm{k,in}\right) \\ - \frac{pV}{m}\sum_\mathrm{out}\dot{m}_\mathrm{out} - \sum_\mathrm{k}\dot{m}_\mathrm{k,gen}u_\mathrm{k}. \end{aligned} \tag{2.15}$$

This form of the energy equation saves resources in evaluating the Jacobian matrix since the derivatives of the species are evaluated at constant temperature instead of at constant internal energy [46]. However, using the real gas behavior is more accurate and is used preferentially.

Ideal Gas Constant Pressure Reactor

Analogous to the ideal gas reactor, the total enthalpy as the state variable is replaced with the temperature. The total enthalpy H is also written here as a function of mass fraction and temperature:

$$H = m\sum_\mathrm{k} Y_\mathrm{k}h_\mathrm{k}(T), \tag{2.16}$$

$$\frac{\partial H}{\partial t} = h\frac{\partial m}{\partial t} + mc_\mathrm{p}\frac{\partial T}{\partial t} + m\sum_\mathrm{k} h_\mathrm{k}\frac{\partial Y_\mathrm{k}}{\partial t}, \tag{2.17}$$

with h_k as specific enthalpy of the species k. Again, the equation for the temperature is obtained by substituting the corresponding derivatives:

$$mc_\mathrm{p}\frac{\partial T}{\partial t} = \dot{Q} - \sum_\mathrm{k} h_\mathrm{k}\dot{m}_\mathrm{k,gen} + \sum_\mathrm{in}\dot{m}_\mathrm{in}\left(h_\mathrm{in} - \sum_\mathrm{k} h_\mathrm{k}Y_\mathrm{k,in}\right). \tag{2.18}$$

Time Integration

To integrate the stiff Ordinary Differential Equation (ODE)s Cantera uses the CVODES solver from SUNDIALS [39, 51]. To advance a time step starting from the system's current state, the step() method is used. The state of the system is calculated a priori with the unspecified time t_{new} which is computed internally. This time is being selected accordingly so that all states in the system are only in a certain tolerance. Furthermore, the time step must not exceed the maximum time step Δt_{max}, which can also be defined before. The new time t_{new} is then returned by the step() method.

2.4 Droplet Evaporation

Droplet evaporation has already been extensively studied and is used in engine technology, especially in spray modeling [91, 62, 104]. This thesis uses evaporation modeling for oil droplets to determine concentration and temperature during compression, as these are responsible for pre-ignitions. Different approaches for modeling differ strongly in accuracy and the necessary computing power. Due to the ever increasing computing power in recent years, even Direct Numerical Simulation (DNS) simulations are possible [103]. However, more straightforward approaches will suffice for this thesis. The Abramzon-Sirignano Model (ASM) [1] has proven to be satisfactory and is often used in spray modeling. Pinheiro and Vedovoto [80] have presented methodologies for applying the ASM, which serve as the basis for the drop evaporation method used. In the following section, the equations used for modeling the pre-ignition are presented.

The following boundary conditions and assumptions are chosen for the physical model. The droplet and the surrounding gas are assumed to be spherically symmetric so that droplet evaporation becomes a 1D problem. This drop consists of a single species and has a uniform temperature. The thermal energy transfer between the liquid droplet and the surrounding gas phase occurs entirely by convection. Radiant energy and internal recirculation flow are not considered in this model. The droplet temperature reaches an equilibrium state at which all energy transferred from the surrounding gas to the droplet is used for evaporation. The sum of the energy fluxes becomes zero, leading to a constant droplet temperature (wet-bulb temperature). For the droplet temperature, it is essential to note that its validity is lost if the temperature of the droplet is close to or above the boiling temperature. Therefore, alternative approaches must be used for superheated droplets to represent the increased evaporation rate due to superheating [104].

The drop evaporation model is described by the differential equations eq. (2.19), eq. (2.20) and eq. (2.21). Assuming a spherically symmetrical drop, the decrease in drop diameter D_d over time t is given by the following equation:

$$\frac{\partial D_\mathrm{d}}{\partial t} = -\frac{\dot{m}_\mathrm{ev}}{\pi \rho_\mathrm{liq} {D_\mathrm{d}}^2}. \tag{2.19}$$

Here the density ρ_liq has the index liq which refers to the liquid phase of the drop. The mass flow of the evaporating drop is $\dot{m}_\mathrm{ev}$, with the index ev which stands for the evaporation rate of the droplet. The mass flow $\dot{m}_\mathrm{ev}$ is calculated with the time derivative of the evaporated mass m_ev:

$$\frac{\partial m_\mathrm{ev}}{\partial t} = -\dot{m}_{ev}. \tag{2.20}$$

The droplet temperature T_d changing with time is calculated as follows:

$$\dot{Q}_\mathrm{d} = m_\mathrm{ev} c_\mathrm{pliq} \frac{\partial T_\mathrm{d}}{\partial t}, \tag{2.21}$$

where $\dot{Q}_\mathrm{d}$ is the heat flux penetrating the drop and c_pliq is the specific heat capacity at constant pressure (isobaric) of the liquid droplet.

The following section presents the equations for the ASM and the algorithm for calculating the droplet evaporation used in this thesis. It is shown how the evaporation rate m_ev and heat flux $\dot{Q}_\mathrm{d}$ needed for solving the differential equations are calculated for each time step. Large temperature gradients occur at the phase boundary of the droplet between the liquid and the surrounding gas. In order to establish reference conditions for the determination of thermodynamic and physical parameters in this area, an averaging method is used for the vapor mass fraction Y and the temperature T. The two values are calculated with the equations

$$T_\mathrm{mix} = (1-\alpha)\, T_\mathrm{s} + \alpha T_\mathrm{g} \tag{2.22}$$

and

$$Y_\mathrm{v,mix} = (1-\alpha)\, Y_\mathrm{v,s} + \alpha Y_\mathrm{v,g}. \tag{2.23}$$

For the weighting parameter α the value ”1/3” is chosen in this thesis as recommended by Yuen and Chen [114]. Also, Hubbard, Denny and Mills [52] confirm the empirical 1/3 value often used in spray modeling. The paper of Ma, Naud and Roekaerts [65] must also be mentioned, who compare measurements and calculations. The authors point out that $\alpha = 1$ is also possible, i.e. the ambient temperature is used directly to determine thermodynamic and physical properties. In many spray applications, the droplets evaporate at low temperature. The gradient is therefore relatively small and the influence of α is negligible. However, in other applications, the ambient temperature can range from the droplet vapor temperature at 350 K to the flame temperature above 2000 K. Here, $\alpha = 1$ would lead to high evaporation rates. It is also noted that the determination of the exact boundary conditions for the ambient gas is very important and has a large influence on the evaporation [65]. This temperature sensitivity affects the whole pre-ignition model, which will be discussed in more detail later.

The reference temperature T_{mix} can be calculated from the droplet temperature at the surface T_{s} and the temperature of the surrounding gas T_{g}. Since no inhomogeneities in the liquid phase can be considered in the model, the temperature at the surface is the same as the droplet temperature T_{d}. Similarly, the reference molar mass fraction $Y_{\mathrm{v,mix}}$ of the vapor can be calculated from the molar mass fraction at the droplet surface $Y_{\mathrm{v,s}}$ and the molar mass fraction in the surrounding gas $Y_{\mathrm{v,g}}$. In the present model, however, the latter is assumed to be zero, since no gaseous oil is yet present in the environment when calculating single droplets.

To calculate $Y_{\mathrm{v,s}}$, $X_{\mathrm{v,s}}$ must first be determined. It is assumed that the vapor concentration is always saturated at the droplet surface, which can be calculated with:

$$X_{\mathrm{v,s}} = \frac{p_{\mathrm{sat}}}{p_{\mathrm{g}}} = \frac{p_{\mathrm{atm}}}{p_{\mathrm{g}}} \exp\left[\frac{\Delta h_{\mathrm{vap}} M_{\mathrm{v}}}{R}\left(\frac{1}{T_{\mathrm{b}}} - \frac{1}{T_{\mathrm{d}}}\right)\right], \tag{2.24}$$

where p_{g} is the ambient pressure and p_{sat} is the saturated vapor pressure at the respective droplet temperature. If the saturation vapor pressure is unavailable, e.g. in the form of a table, the vapor concentration can be determined using the alternative method. The subscript atm stands for atmospheric, Δh_{vap} is the enthalpy of vaporization, M_{v} is the molar mass of the vapor, R is the universal gas constant and T_{b} is the temperature at which the drop boils.

The mole fraction at the vapor surface $X_{\mathrm{v,s}}$ can now be used to calculate $Y_{\mathrm{v,s}}$ in the equation:

$$Y_{\mathrm{v,s}} = \frac{X_{\mathrm{v,s}} M_{\mathrm{oil}}}{X_{\mathrm{v,s}} M_{\mathrm{v}} + X_{\mathrm{g,s}} M_{\mathrm{g}}}. \tag{2.25}$$

The physical and thermodynamic quantities can be determined with the droplet temperature in the gas phase and the gas concentration now being known. These are the diffusion coefficient $D_{\mathrm{v,mix}}$, the specific heat capacities $c_{\mathrm{p,mix}}$ and $c_{\mathrm{p,g}}$, the densities ρ_{mix} and ρ_{g} as well as the dynamic viscosity η_{mix} and the thermal conductivity κ_{mix}. With these values assumed constant during a time step, the Prandtl number:

$$Pr_{\mathrm{mix}} = \frac{\nu \rho_{\mathrm{mix}} c_{\mathrm{p,mix}}}{\kappa_{\mathrm{mix}}}, \tag{2.26}$$

where ν is the kinematic viscosity and the Schmidt number

$$Sc_{\mathrm{mix}} = \frac{\eta_{\mathrm{mix}}}{\rho_{\mathrm{mix}} D_{\mathrm{v,mix}}} \tag{2.27}$$

can be calculated. The Schmidt number divided by the Prandtl number equals the Lewis number:

$$Le_{\mathrm{mix}} = \frac{\kappa_{\mathrm{mix}}}{c_{\mathrm{p,mix}} D_{\mathrm{v,mix}} \rho_{\mathrm{mix}}} = \frac{Sc}{Pr}. \tag{2.28}$$

To consider the flow influence, the Reynolds number is calculated with:

$$Re_{\mathrm{d}} = \frac{\rho_{\mathrm{g}} D_{\mathrm{d}} |\vec{v}_{\mathrm{g}} - \vec{v}_{\mathrm{d}}|}{\eta_{\mathrm{mix}}}. \tag{2.29}$$

The modulus of the two velocity vectors $|\vec{v}_{\mathrm{g}} - \vec{v}_{\mathrm{d}}|$ is the slip velocity between the droplet and the surrounding gas.

The Sherwood number is calculated using the Ranz-Marshall [81] correlation, which was developed primarily for drop geometry:

$$Sh_{\mathrm{mix}} = 2 + 0.6 {Re_{\mathrm{d}}}^{1/2} {Sc_{\mathrm{mix}}}^{1/3}. \tag{2.30}$$

The oldest correlation for calculating the Sherwood number was found in 1938 by Frössling [37] for the application of evaporation. Here, the prefactor before the Reynolds number is 0.552 instead of 0.6, but 0.552 is still often used in spray modeling. Numerous publications have been presented on these empierical correlations for different use cases, geometries and states [41, 36, 11, 12, 86, 17, 64, 40]. In this thesis, however, the Ranz-Marshall correlation is used. The Nusselt number is calculated analogously to the Sherwood number:

$$Nu = 2 + 0.6{Re_\mathrm{d}}^{1/2}{Pr_\mathrm{mix}}^{1/3}. \tag{2.31}$$

With the already known molar mass fractions, the Spalding mass transfer number B_M can be determined:

$$B_\mathrm{M} = \frac{Y_\mathrm{v,s} - Y_\mathrm{v,g}}{1 - Y_\mathrm{v,s}}. \tag{2.32}$$

Energy and mass exchange can be described with the film theory [10]. According to this theory, it will be represented by finite gas films. Due to the Stefan flow effect, these films are thickened [88]. To take the thickening effect into account, the correction factors

$$F_\mathrm{M} = (1 + B_\mathrm{M})^{0.7}\,\frac{\ln(1 + B_\mathrm{M})}{B_\mathrm{M}} \tag{2.33}$$

and

$$F_\mathrm{T} = (1 + B_\mathrm{T})^{0.7}\,\frac{\ln(1 + B_\mathrm{T})}{B_\mathrm{T}} \tag{2.34}$$

are introduced for the diffusive and the thermal film. F_T is the correction factor for thermal film and F_M is the factor for diffusive film. Since the two correction factors physically represent a change in the film thickness due to the Stefan flow, they must always be greater than 1. With the correction factors, the modified Sherwood Sh^* and Nusselt Nu^* number can now be calculated.

$$Sh^* = 2 + \frac{Sh - 2}{F_\mathrm{M}} \tag{2.35}$$

$$Nu^* = 2 + \frac{Nu - 2}{F_\mathrm{T}} \tag{2.36}$$

While F_M and thus Sh^* can be calculated directly, the Spalding thermal energy transfer number B_T, which must be determined iteratively, is needed for determining F_T. For the calculation, a suitable starting value or the value from the preceding iteration (${B_\mathrm{T}}^\mathrm{old}$) is needed.

The number one is in most cases a good first guess, the calculation converges in a few steps so that the estimation does not have to be very accurate. B_{T} is calculated with:

$$B_{\mathrm{T}} = (1 + B_{\mathrm{M}})^{\varphi} - 1. \tag{2.37}$$

The φ is calculated using the modified Sherwood and Nusselt number:

$$\varphi = \frac{c_{\mathrm{p,v}}}{c_{\mathrm{p,g}}} \frac{Sh^*}{Nu^*} \frac{1}{Le_{\mathrm{mix}}}. \tag{2.38}$$

Then

$$\left| B_{\mathrm{T}}{}^{\mathrm{old}} - B_{\mathrm{T}} \right| < \epsilon \tag{2.39}$$

is used to check whether the accuracy of the result is satisfactory. If this is not the case, the step for calculating F_{T} and B_{T} is performed again. For the solution of the differential equations described in eq. 2.19, 2.20 and 2.21, the instantaneous droplet evaporation rate $\dot{m}_{\mathrm{ev}}$ is:

$$\dot{m}_{\mathrm{ev}} = \pi D_{\mathrm{d}} D_{\mathrm{v,mix}} \rho_{\mathrm{mix}} Sh^* \ln(1 + B_{\mathrm{M}}). \tag{2.40}$$

To solve eq. 2.21, the heat flux into the droplet is calculated with:

$$\dot{Q}_{\mathrm{d}} = \dot{m}_{\mathrm{ev}} \left(\frac{c_{\mathrm{p,v}} \left(T_{\mathrm{g}} - T_{\mathrm{d}}\right)}{B_{\mathrm{T}}} - \Delta h_{\mathrm{vap}} \left(T_{\mathrm{d}}\right) \right), \tag{2.41}$$

where $\Delta h_{\mathrm{vap}} \left(T_{\mathrm{d}}\right)$ is the enthalpy of evaporation as a function of the drop temperature T_{d}. Regarding the simulation of engine-related application areas, it should be pointed out that this model cannot handle droplets whose surface temperature is equal to the boiling temperature. In case the droplet temperature is equal to the saturation temperature ($T_{\mathrm{d}} = T_{\mathrm{sat}}$), it yields to $Y_{\mathrm{v,s}} = 1$ and thus to $\dot{m}_{\mathrm{ev}} \propto B_{\mathrm{M}} \rightarrow \infty$ [104]. This singularity is a weak point that also exists in other evaporation models based on Spalding's assumption [30].

3 Reaction Kinetic Analysis of the Pre-Ignition Process

3.1 Methodology and Model Setup

Ignition delay calculations are often used in the simulation and modeling of knocking or auto-ignition mechanisms in Internal Combustion Engine (ICE) applications. Ignition delays can be measured with a Rapid Compression Machine (RCM). For this purpose, a mixture is rapidly compressed and then kept at the same volume. Due to the high pressure and temperature, the mixture ignites and the ignition delay can be determined. Since the measurements are complex and expensive and must cover many boundary conditions, the ignition delay is calculated using reaction kinetic mechanisms in simulation applications. When creating reaction mechanisms, these are validated against measurement data from RCMs.

A tool was developed for this purpose, which is briefly presented in the following section. It is capable of calculating ignition delays by multiprocessing, has already been presented and is described in more detail in [108, 105]. Use cases for this tool have already been published in [108]. Here only those parts which are relevant for this thesis are explained.

All reaction kinetics studies in this thesis are performed with Cantera [45] and programmed in Python [101]. Cantera is an open-source suite of tools for problems involving chemical kinetics, thermodynamics, and transport process and can be used from Python and Matlab or in applications written in C/C++ and Fortran 90. The advantage of using Cantera and Python is that the software can be used without licensing fees.

Table 3.1 lists the boundary conditions required for calculating ignition delay times. The list includes standard engine parameters such as pressure p, temperature T, AFER λ and the fuel composition. In addition, the parameter X_{oil} must be entered, which defines the proportion of the lubricating oil substitute in the overall mixture. The oil fraction is relevant for the reaction kinetics investigations because, as explained in section 2.2, the lubricating oil has a decisive influence on the pre-ignition, which will be shown in the course of this thesis.

Table 3.1: Boundary conditions for the calculation of ignition delay times.

Parameter (Symbol) [Unit]	Description
Pressure (p) [Pa]	Starting pressure of the mixture
Gas Temperature (T) [K]	Start temperature of the mixture
Fuel Composition	Mole fraction of the fuel components
Air–Fuel Equivalence Ratio (λ) [-]	Ratio of actual AFER to stoichiometry
Mole fraction oil (X_{oil})[-]	Mole fraction of the lubricating oil surrogate in the gas mixture
EGR Rate (Y_{EGR})[-]	Ratio of exhaust gas mass to total mass

3.1.1 Model Structure

The model structure for the reaction kinetic investigations is shown schematically in **??**. The fuel composition is given here as a boundary condition, consisting of a pure substance or a mix of different species. Furthermore, the temperatures, pressures and the AFER λ are to be specified. Also the desired EGR fraction is set which is mainly used in this thesis after definition of the stoichiometric EGR and is defined in section 3.1.5. For the investigations with lubricating oil influence, the fraction of lubricating oil substitute, which will be discussed in more detail in section 3.1.3, is set. A reaction mechanism is required for the calculations. The selection of a suitable mechanism for this thesis is explained in section 3.1.4.

At the beginning of the calculation, the initial gas composition is calculated from the previously mentioned boundary conditions. A mixture of N_2 and O_2

is used as fresh air. All other components of the air are neglected. Two procedures are possible in the model for calculating the EGR composition. The first is the classical case in which the initial mixture is brought into chemical equilibrium, i.e. the reaction is given an infinite amount of time. This composition is now added as the EGR fraction. Since in the operation of an internal combustion engine only limited time is available for the reactions, a second setting is possible. In this case the reaction is stopped after a defined time which corresponds to the approximate combustion time. In this mixture, products of incomplete reactions are now present, as they would be in an engine, and are added as an EGR content [108].

In a zero-dimensional reactor, as explained in section 2.3.2, the system of equations for the reactions is solved. The result of this calculation is the concentration of all species represented in the reaction mechanism and the temperature as arrays as a function of time. From these, the ignition can then be calculated as explained in section 3.1.2.

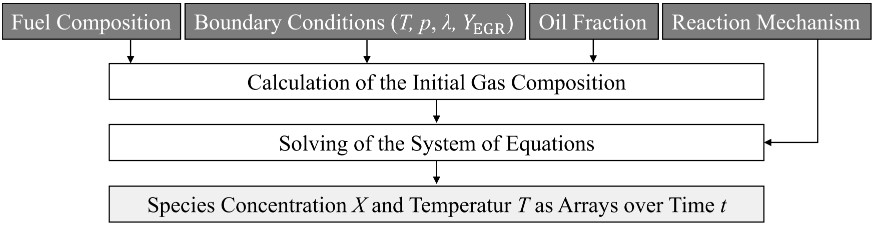

Figure 3.1: Schematic model structure of the ignition delay calculation with addition of lubricating oil.

3.1.2 Ignition Determination

In order to determine the ignition in an ignition delay calculation, several criteria are determined simultaneously in each calculation. The calculation of these criteria does not bring a significant calculation time disadvantage and is therefore used as a comparison. In the case of outliers of a criterion, this can indicate a faulty calculation and thus also be used as debugging.

Four criteria are implemented, two of which depend on the temperature and two on the concentration of the hydroxyl radical($^{\bullet}$OH). The four criteria are shown in fig. 3.2 for an example with methane (CH_4) as fuel at a temperature of 1200 K and a pressure of 30 bar.

The two temperature-dependent criteria τ_{ignT300} and τ_{ignT400} are based on the principle of the temperature increase of the mixture compared to the start value. The criterion τ_{ignT300} is therefore triggered when the temperature in the reactor has increased by 300 K. Similarly, the temperature at τ_{ignT400} must increase by 400 K for ignition to be detected. In most cases, the temperature change gradient is much steeper than the example in fig. 3.2a. Often the temperature-dependent criteria are even closer together.

The other criteria relate to the $^{\bullet}$OH radical formed during the conversion of hydrocarbons. Metrologically, the emitted light of the species can be used to measure the $^{\bullet}$OH evolution and thus detect an ignition [42]. As shown in fig. 3.2b, the first criterion τ_{ignOHmax} is the maximum $^{\bullet}$OH concentration. Since the evaluation is performed according to the reaction time set in the reactor, the determination is relatively simple. If ignition does not occur, it is evident that this criterion returns the maximum value. The redundancy with the temperature-dependent criteria becomes clear, since a non-existent ignition is detected in this way.

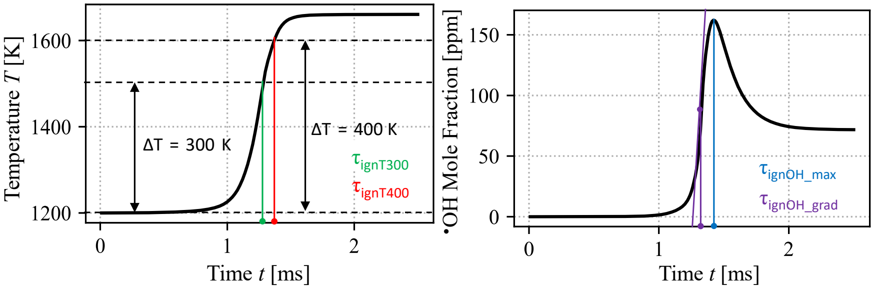

(a) Temperature-dependent ignition criteria.

(b) $^{\bullet}$OH dependent ignition criteria.

Figure 3.2: Ignition criteria for determining the ignition.

For the detection with $\tau_{\text{ignOHgrad}}$, a tangent is applied to the point where the slope is steepest. Mathematically, the second derivative would be zero at this point. The point of intersection of this tangent with the time axis is the ignition delay time for this criterion.

3.1.3 Lubricating Oil Surrogate

In order to take the influence of lubricating oil into account, a substitute had to be found. Unfortunately, precise oil compositions could not be provided for the test rig measurements or the real engine. The properties of the substitute must therefore represent those of the lubricating oil sufficiently accurately. Furthermore, the substitute should cover a wide range of lubricating oils if possible.

A pragmatic approach was therefore adopted. Distaso et al. [28] describe in their paper that the influence of lubricating oil on ignition delay during gasoline combustion can be reproduced very well with C_{16}-C_{18} hydrocarbons. Furthermore, he states that his result ”implies that it is reasonable to neglect the additives’ effect in developing a reaction mechanism for lubricant oil”[28].

Kuti et al. support this statement and states in the conclusion of their work that C_{16}-C_{18} n-alkanes represent the ignition characteristics of real base oils and fully formulated lubricants very well. They also found that the chemical ignition delay plays a more significant role than the physical one, which will be discussed later. Further investigations must also be carried out with organometallic additives to investigate their influence, as is also briefly mentioned with $CaCO_3$ in section 2.1. However, the influence is negligible compared to the hydrocarbons in the base oil [57].

The experiments of Kuti et al. [57] compared with the simulations of Distaso et al. [28] show that at 1 % lubricating oil content, the behavior can be perfectly reproduced with 100 % n-hexadecane ($nC_{16}H_{34}$). If lubricating oil content is increased to 10 %, the behavior can be reproduced well with a mix of 50 % n-octadecane ($nC_{18}H_{38}$) and 50 % n-hexadecane. As the calculations later in this thesis show, lube oil concentrations of no more than 1 % of the mix are a more realistic value. Furthermore, within the framework of this thesis, attempts are made to calculate ignition delay times for C_{18} n-alkanes, and the calculation times on a single core are in the range of more than one day, while the calculation time for C_{16} hydrocarbons is approximately 100 s.

In summary, it can be said that excellent results can be expected with n-hexadecane as a lubricating oil substitute with manageable calculation times. In this thesis, oil, lubricating oil or lubricating oil substitute always refers to the species n-hexadecane with which all further investigations are carried out.

For completeness, table 3.2 gives the coefficients of the NASA 7-coefficient polynomial parameterization used to calculate the species reference-state thermodynamic properties $c_\mathrm{p}(T)$, $h(T)$ and $\mathrm{s}(T)$. The coefficients are divided into two temperature ranges. The Low Temperature (LT) range between 300 K and 1800 K and the High Temperature (HT) range between 1800 K and 3500 K. The coefficients are taken from the POLIMI_TOT_NOx_1412 kinetic mechanism [82, 33, 35, 21]. This reaction mechanism will be discussed in more detail in section 3.1.4. With this information, the material properties of hexadecane can be calculated for the lubricating oil substitute as described in section 2.3.1.

Table 3.2: NASA 7-coefficient polynomial parameterization for the high (1800-3500 K) and low temperature (300-1800 K) regime for the lubricating oil substitute $nC_{16}H_{34}$ [82, 33, 35, 21].

Polynomial Coefficient	**LT (300 - 1800 K)**	**HT (1800 - 3500 K)**
a_0	−3.6406e0	4.9821e+1
a_1	1.9619e−1	7.7388e−2
a_2	−1.2676e−4	−2.7756e−5
a_3	4.1365e−8	4.6968e−9
a_4	−5.4057e−12	−3.1296e−13
a_5	−5.1605e+4	−7.0851e+4
a_6	6.4502e+1	−2.2484e+2

3.1.4 Selection of the Reaction Kinetic Mechanism

In order to select a suitable reaction mechanism, a mechanism comparison was performed. The reaction mechanisms used for the comparison are listed in table 3.3. The individual reaction mechanisms are briefly described and explained in the following section.

Table 3.3: Reaction mechanisms for mechanism comparison.

Reaction Mechanism	Species	Reactions	*T* Range
Gri 3.0	53	325	LT + HT
POLIMI_DIESEL_REDUCED_1410	201	4240	LT + HT
LLNL_Diesel_Surrogate_Detailed	2885	11754	LT + HT
POLIMI_C1-C16_HT+LT+NOx_2003	537	18250	LT + HT
POLIMI_TOT_NOX_1412	484	19341	LT + HT

Gri 3.0

The GRI-Mech 3.0 [92] mechanism is one of the best-validated mechanisms for natural gas combustion, which is why it is also used as a benchmark in this thesis. In many simulation programs, this mechanism is already supplied as standard. Furthermore, due to the small number of species and reaction equations, the calculation time is much shorter compared to mechanisms that can calculate longer chain hydrocarbons.

POLIMI_DIESEL_REDUCED_1410

This reaction mechanism is from ”The CRECK Modeling Group” at the Politecnico di Milano [83, 94, 95]. It is a reduced diesel substitute mechanism with LT. It is mainly used for the combustion of fossil and biomass-derived transportation fuels and can handle longer-chain hydrocarbons.

LLNL_Diesel_Surrogate_Detailed

This mechanism has been developed for the combustion of diesel substitute fuel at Lawrence Livermore National Laboratory (LLNL). The detailed multi-component mechanism for $nC_{12}H_{26}$ and C_8H_{10} was developed by combining the $nC_{12}H_{26}$ mechanism with a recently developed mechanism detailing the combustion of the xylene isomers [78]. At this point, it must be mentioned that a comparison with the LLNL mechanism for the oxidation of 2-methylalkanes from C7 to C20 [87] would have been appreciated. At the time of work on this thesis, the mechanism is not fully available on the website. Unfortunately, entries for species in the theromdynamics as well as in the transport properties are missing.

POLIMI_C1-C16_HT+LT+NOx_2003

This reaction mechanism [83, 84, 8], also developed by ”The CRECK Modeling Group” at Politecnico di Milano, can handle hydrocarbons with chain lengths up to C16. This property makes it possible to calculate the lubricating oil substitute described in section 3.1.3.

POLIMI_TOT_NOX_1412

The POLIMI_TOT_NOx_1412 [82, 33, 35, 21] is the third of the investigated reaction mechanisms of ”The CRECK Modeling Group” at Politecnico di Milano. It can also model the lubricating oil substitute $nC_{16}H_{34}$. In addition, it can calculate the formation of NO_x during combustion.

Comparison of the reaction mechanisms for the combustion of methane

Gas engines are the main area of application for the methodology developed in this thesis. Natural gas consists largely of methane (CH_4), but can also contain other components depending on its origin. These can have a mole fraction of 1 % to 15 % ethane (C_2H_6) and 1 % to 10 % propane (C_3H_8). Other minor components are butane (C_4H_{10}), ethylene (C_2H_4) and pentane (C_5H_{12}). For the mechanism comparison, however, we assume 100 % methane. The influence of different natural gas compositions or fuel qualities can be seen in section 3.2.1.

Figure 3.3 shows the mechanism comparison at $\lambda = 3$, $p = 50\,\text{bar}$. The results for the mechanisms POLIMI_DIESEL_REDUCED_1410 and POLIMI_-TOT_NOx_1412 are identical and lie on each other. Since both reaction mechanisms were developed by ”The CRECK Modeling Group”, it can be assumed that the parameters for the combustion of methane are identical. Both results are close to Gri 3.0. Due to the very good validation of Gri 3.0, this was taken as a reference for methane combustion and a mechanism that is close to Gri 3.0 can be considered suitable. LLNL_Diesel_Surrogate_Detailed and POLIMI_C1-C16_HT+LT+NOx_2003 are close to each other but show a difference in the temperature range between 950 K and 1050 K. However, both mechanisms deviate more strongly from Gri 3.0 than POLIMI_DIESEL_REDUCED_1410 and POLIMI_TOT_NOx_1412.

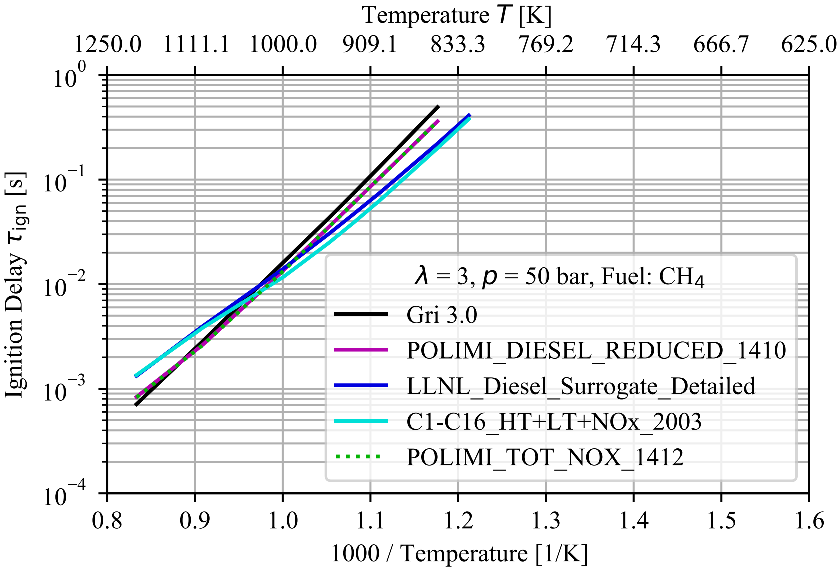

Figure 3.3: Comparison of the reaction mechanisms for $\lambda = 3$, $p = 50$ bar and fuel = CH_4.

To see if this behavior is the same with changed boundary conditions, a parameter variation with changed pressure (fig. 3.4c) and changed AFER (fig. 3.4b) from fig. 3.3 is shown in fig. 3.4.

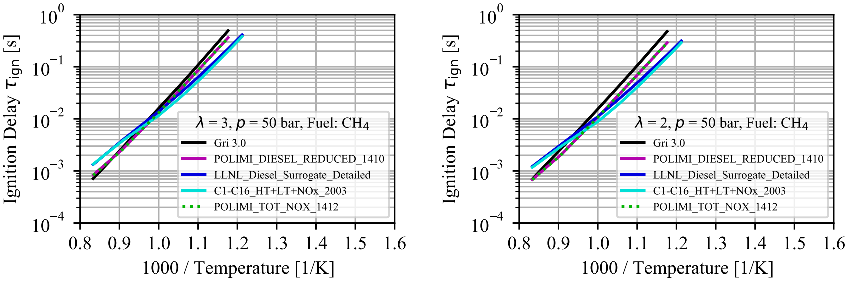

(a) $\lambda = 3$, $p = 50$ bar and fuel = CH_4. **(b)** $\lambda = 2$, $p = 50$ bar and fuel = CH_4.

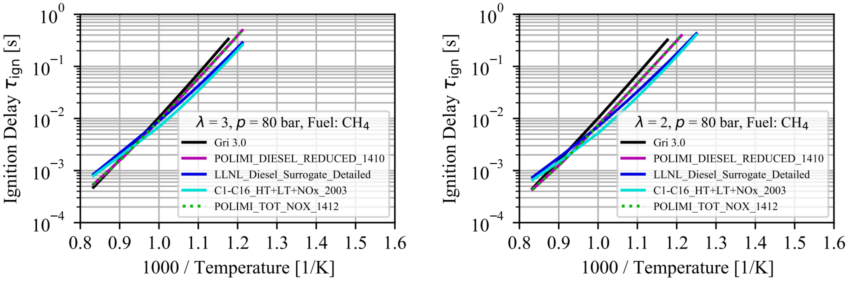

(c) $\lambda = 3$, $p = 80$ bar and fuel = CH_4. **(d)** $\lambda = 2$, $p = 80$ bar and fuel = CH_4.

Figure 3.4: Parameter variation for comparison of reaction mechanisms for methane combustion.

The POLIMI_DIESEL_REDUCED_1410 and POLIMI_TOT_NOx_1412 are still closer to Gri 3.0 than LLNL_Diesel_Surrogate_Detailed and POLIMI_C1-C16_HT+LT+NOx_2003 as can be seen. With decreasing λ, the difference is slightly more significant than with $\lambda = 3$. The influence of the higher pressure of 80 bar has virtually no effect on the result. POLIMI_DIESEL_REDUCED_-1410 and POLIMI_TOT_NOx_1412 seem the most suitable for this thesis when only methane combustion is considered.

Since the lubricating oil substitute $nC_{16}H_{34}$ has to be included in the calculation, as described in section 3.1.3, a comparison can be seen in fig. 3.5. Here, the oil ($nC_{16}H_{34}$) quantity is varied. It turned out that the LLNL mechanism cannot represent n-hexadecane, so it is eliminated from the selection.

It can be seen that the POLIMI_TOT_NOx_1412 mechanism at 0.1 % oil is almost identical to the diesel mechanism. On the other hand, at 1 % oil content, it is more in the range of the POLIMI_C1-C16_HT+LT+NOx_2003 mechanism, especially at higher temperatures. However, the differences are relatively small. It must also be pointed out that the calculation of ignition delay is always subject to a certain degree of inaccuracy, since an uncertainty of ±15 % to ±20 % is already present in the experiment when determining the individual ignition delay data points [26].

As a result of this investigation, the POLIMI_TOT_NOx_1412 is selected. All further reaction kinetic investigations are carried out with this mechanism unless otherwise stated.

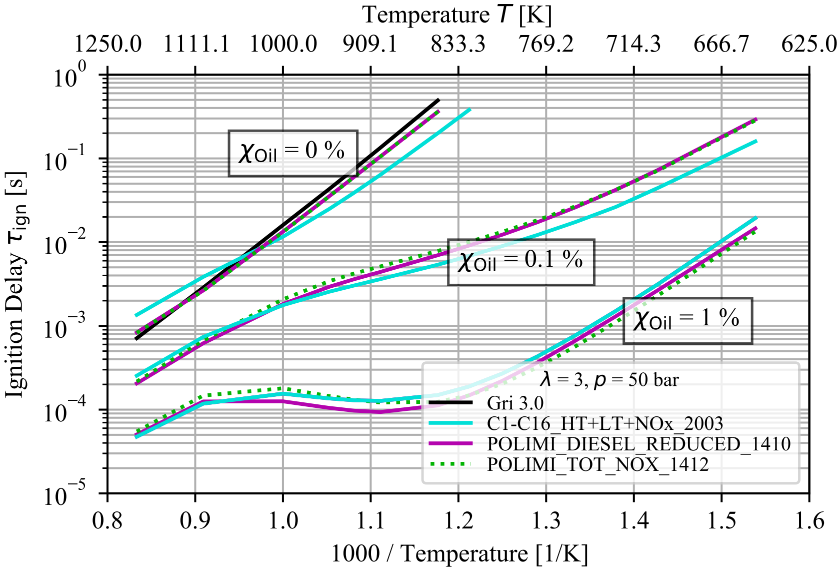

Figure 3.5: Comparison of the reaction mechanisms for $\lambda = 3$, $p = 50$ bar, fuel = CH_4 and lube oil surrogate admixture.

3.1.5 EGR Definition

Unless otherwise stated, the stoichiometric EGR is used in this thesis for the definition of the EGR rate. This definition is suitable for largely lean-burn engines such as diesel or the marine engines analyzed, since only inert species (CO_2, H_2O and N_2) are considered as exhaust gas.

The stoichiometric EGR rate $Y_{\mathrm{EGR,st}}$ can be calculated from the classical EGR rate $Y_{\mathrm{EGR,classic}}$ using equation eq. (3.1):

$$Y_{\mathrm{EGR,st}} = \frac{1 + L_{\mathrm{st}}}{1 + \lambda L_{\mathrm{st}}} Y_{\mathrm{EGR,classic}} \tag{3.1}$$

where λ is the air-fuel equivalence ratio and L_{st} is the stoichiometric air-fuel mixture. From the definition it can be seen that with increasing λ, i.e. with lean mixtures, the mass fraction of air increases with the classical EGR, while with the stoichiometric EGR the air mass fraction remains more or less constant. Another effect is that the fraction of inert gas mass decreases with increasing λ in the case of the classical EGR, while it remains constant in the case of stoichiometric EGR. The comparison is published in [105] by the author of this thesis, among others, and can be accessed there.

The advantage of the stoichiometric EGR definition becomes apparent with lean mixtures. Since the unburned O_2 is not added again by EGR, a better comparability and evaluation is possible in the reaction kinetic investigations. It must be mentioned that there is no really uniform definition in real applications. Depending on the test bench configuration or implementation in the engine, the simulation must be adapted to the real application, which is possible without any problems.

3.1.6 Reactor Type

Four different reactor types can be used for the reaction kinetics. The choices are ideal isochor, ideal isobar, real isochor and real isobar. The ideal gas behavior is used for the two ideal variants. For the real variants, real gas properties are taken into account. The underlying equations for the reactor types are explained in section 2.3.2. For the isochoric reactor types, the reactor volume is kept constant. This is an extensive thermodynamic control volume with homogeneous distribution of temperature, pressure and species concentration, which is why this is still a 0D reactor and not a 3D volume. Since the volume remains constant, the pressure increases during the reaction. In the isobaric case, analogously, the pressure is kept constant.

In the results presented in this thesis, only real gas behavior is considered, which is why the reactor types with ideal gas are not discussed in detail here. In order to show the influence of the isobaric and isochoric real gas reactor types, ignition delay times are calculated for boundary conditions of a lean gas engine near TDCF. The POLIMI_TOT_NOx_1412 selected in section 3.1.4 is chosen as the reaction mechanism. The pressure is 70 atm and CH_4 is chosen as the fuel at an AFER of $\lambda = 2$.

The result of the calculation can be seen in fig. 3.6 which shows that the isochoric variant has about 10 % lower ignition delay times compared to the isobaric case. The difference can be explained by the reaction kinetics, since the volume of the isobaric reactor is constantly adjusted to maintain the same pressure, which leads to a slower temperature rise since temperature and pressure are coupled with each other. As a result, higher temperatures and pressures reduce the ignition delay times, as shown in more detail in section 3.2.1. A more extensive comparison is published in [105], co-authored by the author of this thesis.

In summary, the influence of reactor type is relatively small. Depending on the application, evaluating which reactor type makes the most sense for the task used is necessary. The real isobaric reactor is used for all investigations, since a temperature increase in the area of pre-ignition causes a change in density and thus takes up more volume.

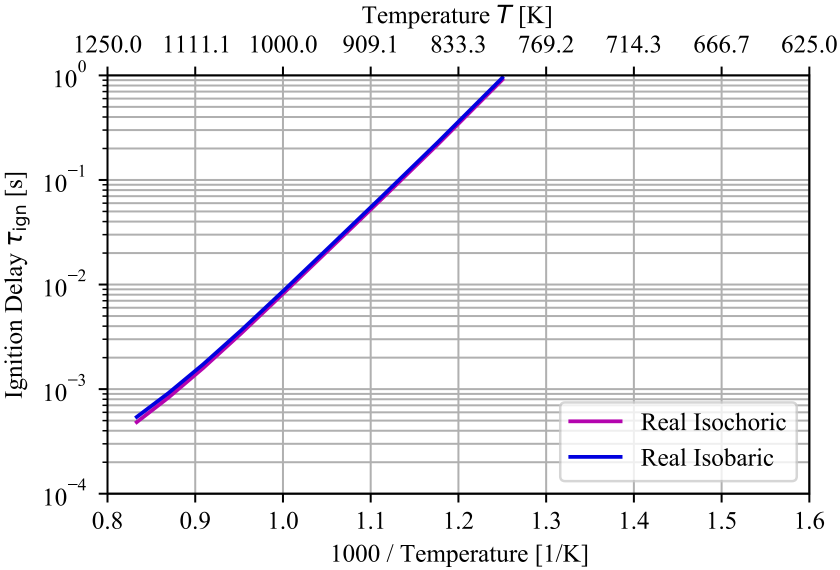

Figure 3.6: Ignition delay times in a comparison of the reactor types ”real isochoric” and ”real isobaric” at a pressure of 70 atm and $\lambda = 2$ with CH_4 as fuel.

3.2 Reaction Kinetic Studies on Ignition Process

3.2.1 Secondary Reaction Kinetic Effects

In this section, the secondary reaction kinetic influences are discussed, i.e. influences that have a rather minor effect on the ignition delay. However, these influences cannot be neglected and can have a stronger or weaker effect in different applications. In the discussion of the individual parameters, the lubricating oil influence is already included in some cases to enable a cross-comparison. The influence of the lubricating oil on the ignition delay is discussed in detail in section 3.2.2.

Influence of Fuel

In order to evaluate the fuel influence on the ignition delay, a comparison is carried out. For this purpose, different Natural Gas (NG) compositions are calculated and compared. The Russian NG as an example of high quality and the Mix NG as an example of low quality. A high methane content is considered high quality, as this fuel has a higher anti-knock property. Both of these compositions are taken from the data provided by Gecko Instruments GmbH [31]. In addition, the comparison with marine LNG [71] is extended since this thesis primarily focuses on marine applications. The reference value is 100 % methane.

Figure 3.7 shows the fuel compositions as a bar chart. It should be noted that, for better readability, the x-axis starts at 80 % to make it easier to identify the smaller fractions.

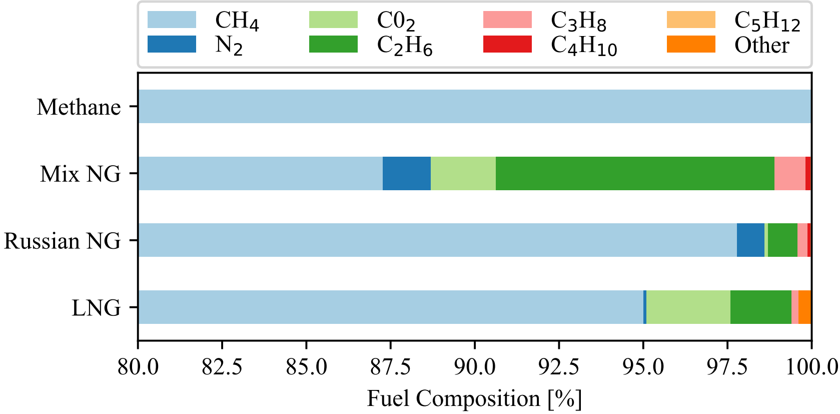

Figure 3.7: Fuel compositions of changing qualities of natural gas (data from [31, 71]).

Figure 3.8 shows the ignition delay times for the different fuels at the AFER $\lambda = 2$ and a pressure p of 80 bar. As expected, the fuels with a higher methane content have a longer ignition delay time, led by the 100 % methane curve.

The curves for Russian NG and LNG are almost on top of each other. However, the Russian NG has a minimally lower ignition delay time than the LNG. This because the Russian NG contains more propane and more butane in the fuel composition. Above all, butane has a significantly reduced ignition delay time compared to propane [70] and thus slightly reduces the ignition delay time of the mixture.

The mix NG has a significantly lower ignition delay time and already ignites at lower temperatures. This effect is mainly due to the high proportion of ethane and the even higher proportion of propane and butane compared to Russian NG.

The influence of lubricating oil on the ignition delay is clearly shown in the two curves with 0.05 % respectively 0.5 % addition of oil to the fuel mixture. The difference between the individual fuel compositions minimizes with increasing lubricating oil content. At 0.5 % oil, the fuel influence is almost non-existent.

With this knowledge, precise fuel modeling can therefore be dispensed. It is possible to represent the exact fuel later in the model, but no significant added value is expected. For this reason, further investigations will be carried out with 100 % methane unless otherwise specified. For ignition, the difference is negligible. However, the fuel influence on flame propagation after a previous pre-ignition can be present. This influence must be investigated in more detail and is not part of this thesis.

Finally, it must be said that these fuel compositions are chosen to analyze the influence. However, the fuel compositions of NG vary greatly depending on the country of origin and e.g. the LNG shown here is an example of marine LNG, which does not have the same composition in all regions.

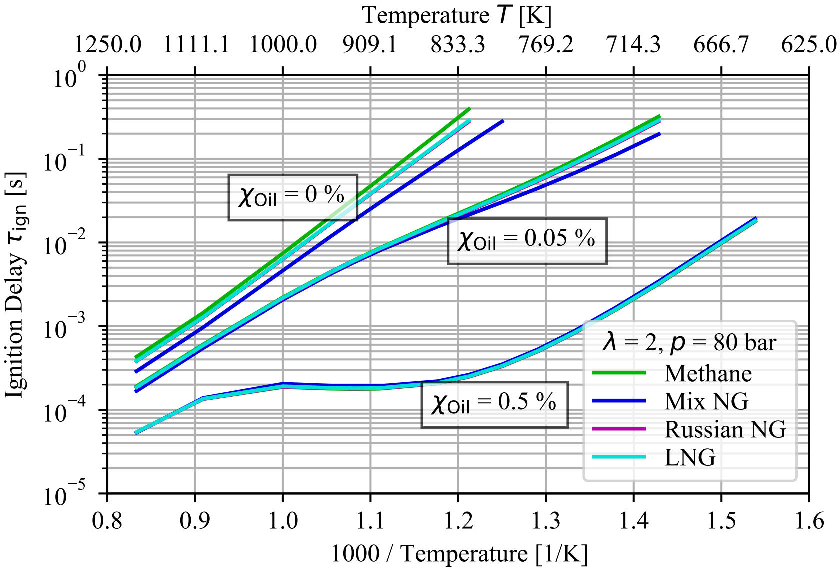

Figure 3.8: Comparison of different fuel compositions for $\lambda = 2$ and $p = 80$ bar.

Influence of Pressure

Figure 3.9 shows the influence of the pressure p on the ignition delay. For the analysis, a pressure variation between 1 and 100 bar is carried out. $\lambda = 2$ is selected as the example parameter for the AFER. It can be seen that as the pressure increases, the ignition delay time is reduced. In the low pressure range between 1 and 5 bar, the change in ignition delay time is significantly greater than in the rest of the pressure range investigated. Between 1 and 10 bar, the change in ignition delay is approximately that of the range between 10 and 100 bar.

In summary, it can be said that a change in pressure strongly affects the ignition delay, especially in the low-pressure range. On the other hand, a few bar increase in pressure at the end of compression will not significantly affect ignition delay. As can be seen, the associated higher final compression temperature has a significant influence.

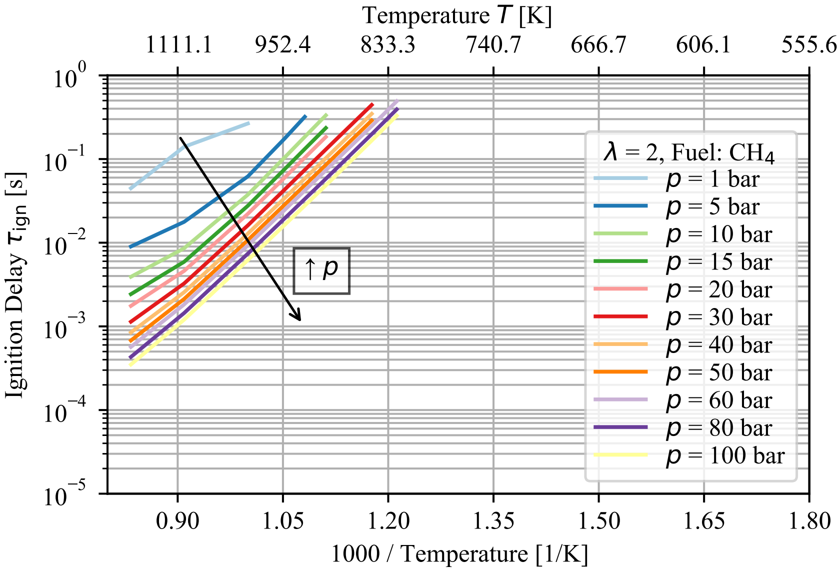

Figure 3.9: Ignition delay with a pressure variation for $\lambda = 2$ and fuel = CH_4

Influence of AFER

A variation of λ is performed to investigate the influence of the AFER on the ignition delay. Figure 3.10 shows the ignition delay between $\lambda = 0.8$ and $\lambda = 3.6$ at a pressure of 80 bar. As λ decreases, the ignition delay time decreases. The differences between the individual curves are minimal. The influence of λ seems to be less than the influence of pressure discussed in section 3.2.1.

Mixture inhomogeneities thus have a relatively small effect on pre-ignition. However, the AFER has a non-negligible influence on a possible flame propagation after a previous pre-ignition, as will be analyzed and discussed in more detail in section 3.3.

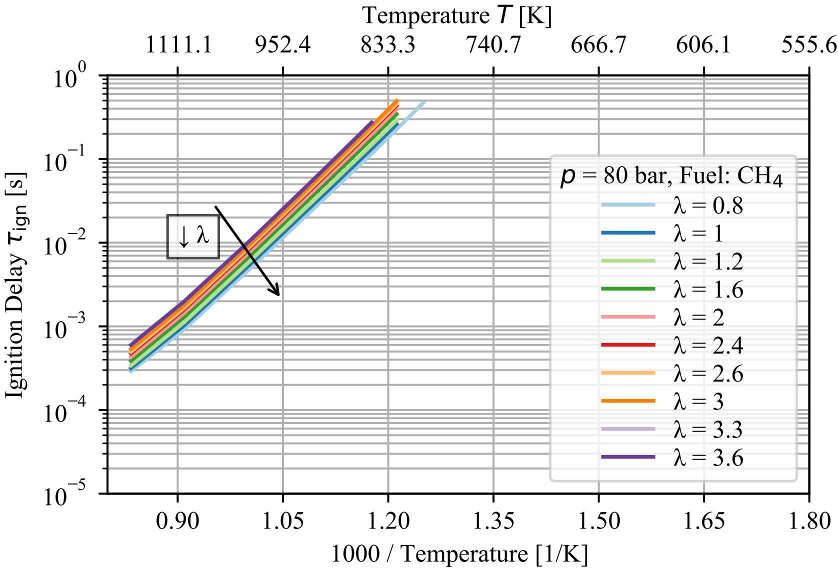

Figure 3.10: Ignition delay with a AFER variation for $p = 80$ bar and fuel = CH_4.

Influence of EGR

The influence of EGR as defined in section 3.1.5 is investigated with a variation of the EGR fraction. Figure 3.11 shows the ignition delay times with an EGR content between 0 % and 65 %. At this point, it must be explained that 65 % stoichiometric EGR is an unrealistically high proportion that is unlikely to occur in real applications. 25 % stoichiometric EGR at the AFER of $\lambda = 2$ used for this example means a value of approx. 50 % for the classical EGR. This value is already relatively high in practice and therefore higher EGR values are only to be understood as an example to analyze the influence.

As can be seen, the ignition delay time increases with increasing EGR fraction. However, the difference between 0 % and 25 % stoichiometric EGR content is relatively small. From this it can be deduced that the EGR influence on pre-ignition is negligible. However, the EGR fraction affects the flame propagation after pre-ignition, which is not investigated in more detail.

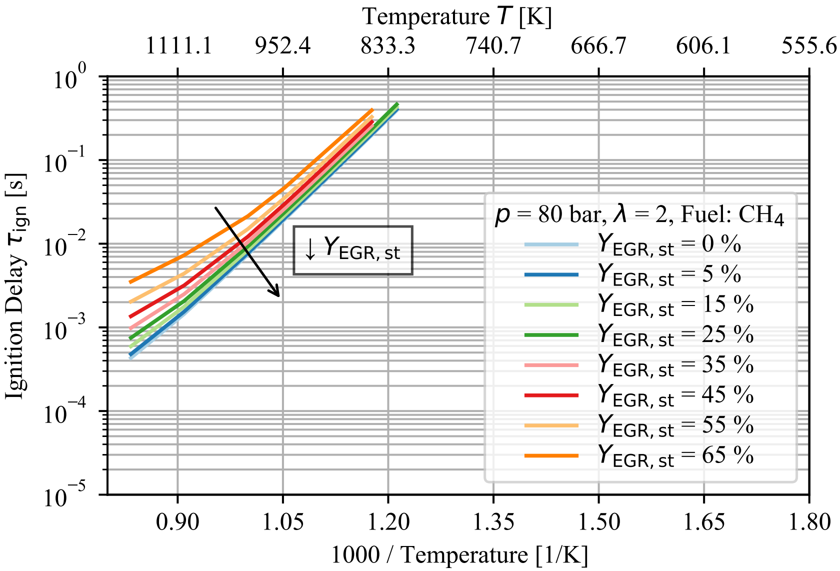

Figure 3.11: Ignition delay with a EGR variation for $p = 80$ bar, $\lambda = 2$ and fuel = CH_4.

To better classify the magnitude of the different EGR fractions, table 3.4 shows a few example values for the definition in section 3.1.5. Methane is used as the fuel for which an L_{st} of 17.12 applies. It can be seen that for $\lambda = 1$ the two values for $Y_{EGR,st}$ and $Y_{EGR,classic}$ are identical. Only in the case of excess air the effect of the stoichiometric EGR applies. With increasing AFER, the stoichiometric EGR share decreases in comparison to the classic EGR.

Table 3.4: Comparison of the two EGR definitions $Y_{\mathrm{EGR,classic}}$ and $Y_{\mathrm{EGR,st}}$ using example values for methane combustion.

L_{st} [-]	λ [-]	$Y_{\mathrm{EGR,classic}}$ [%]	$Y_{\mathrm{EGR,st}}$ [%]
17.12	1	10	10
17.12	1	25	25
17.12	1	50	50
17.12	2	10	5.14
17.12	2	25	12.85
17.12	2	50	25.71
17.12	3	10	3.46
17.12	3	25	8.65
17.12	3	50	17.30

3.2.2 Dominating Effects

In section 3.2.1, the influence of fuel, pressure, AFER and EGR on ignition delay is analyzed. All influencing parameters except temperature and pressure have a relatively small influence on the ignition delay. It is shown that auto-ignition of the mixture is not possible at the usual temperatures (700 K - 800 K) and pressures (70 bar - 80 bar) at the end of compression, even at low engine speeds. In the section where the influence of the fuel is investigated, the influence of the oil is briefly mentioned and shown. Here, a significant shortening of the ignition delay time can be observed, even with small amounts of lubricating oil. As already introduced in section 2.2, oil is probably the main factor influencing pre-ignition and is discussed in more detail in this section.

The influence of the lubricating oil on the ignition delay is shown in fig. 3.12 as a variation between 0 % and 5 % lubricating oil content at $\lambda = 2$ and $p = 80$ bar. It can be seen that even at low oil quantities of 0.05 %, a significant shortening of the ignition delay occurs. Ignition can also be seen at lower temperatures in the time window considered. With small amounts of oil, a range is reached in which auto-ignition is possible with normal engine parameters. Also favored by the low rotational speeds of larger gas engines, pre-ignition with oil influence is expected, which is not to be seen with the other influencing parameters.

At concentrations of the lubricating oil in the gas mixture of more than 0.5 %, NTC behavior can be observed between 830 K and 1100 K. As the temperature rises, the ignition delay remains the same or increases again slightly at even higher oil concentrations. In this temperature range, close to the liquid phase of the oil droplet where the oil vapor concentration is high, it can be assumed that a temperature increase has no or hardly any effect on the ignition delay.

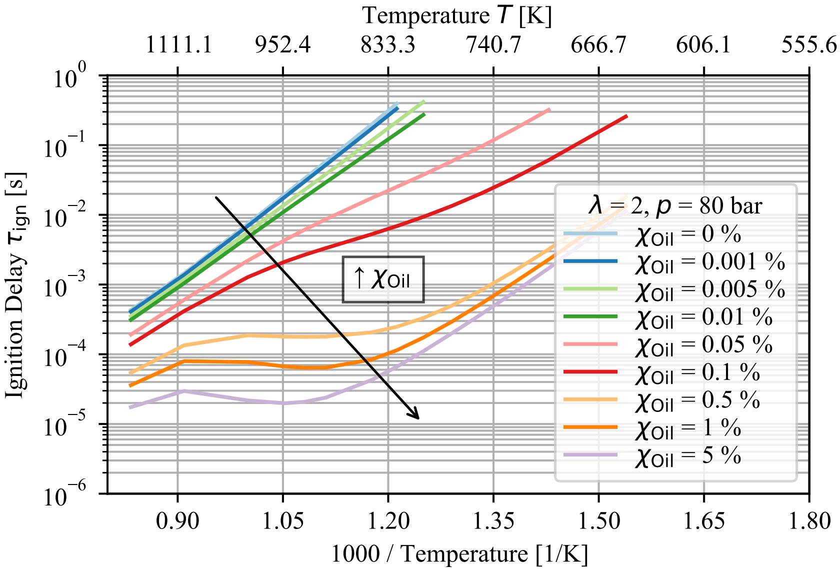

Figure 3.12: Ignition delay with an oil variation for $p = 80$ bar, $\lambda = 2$ and fuel = CH_4.

As shown in the previous chapter, the most significant influencing variables, together with the oil content, are pressure and temperature. For this reason, a cross-comparison is shown in the following two graphs. Figure 3.13 shows the first variation in which the ignition delay is plotted as a function of oil concentration and pressure. The AFER $\lambda = 2$ and a temperature of 750 K, which is a typical compression end temperature, is chosen. It can be seen that for small amounts of oil < 0.05 %, there is no ignition in the analyzed range of 1 s. With an oil content of 0.1 % or more, it is noticeable that the pressure influence decreases as the oil content increases.

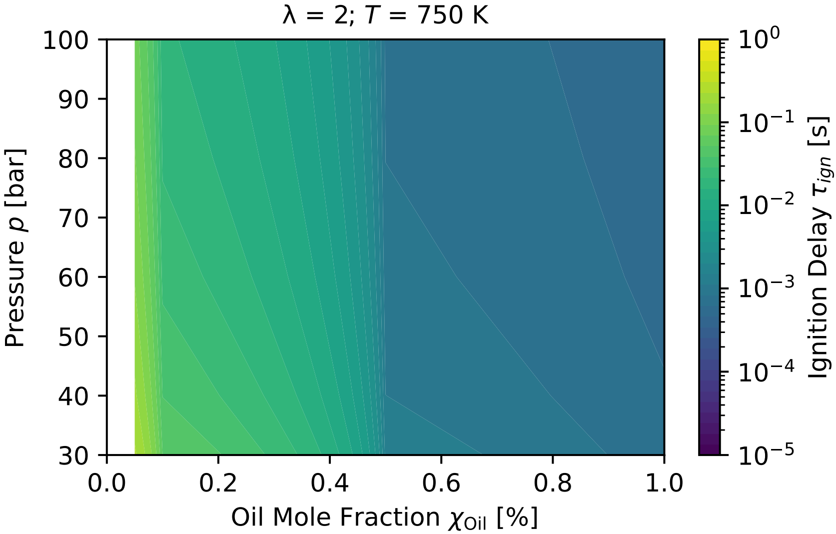

Figure 3.13: Ignition delay with a oil and pressure variation for $\lambda = 2$, $T = 750$ K and fuel = CH_4.

To see a difference in the AFER to fig. 3.12, fig. 3.14 shows the variation of temperature and oil influence with λ = 1.5 and a pressure of p = 80 bar. Since the AFER has hardly any influence on the ignition delay, similarities can be observed in the interpretation. It can be seen that ignition is already detected at 0.05 % oil and 700 K, which is also evident from the diagrams in fig. 3.12 and fig. 3.13 shown above. Based on the contour lines between 0.1 % and 0.5 % oil content, it is noticeable that the temperature has a much more significant influence, in contrast to the pressure variation. With increasing oil content, the ignition delay time also decreases, but with increasing temperature, the influence is at least more decisive up to an oil concentration of 0.5 %. This behavior continues at least in the low-temperature range below 825 K. Above 825 K and above 0.5 % lubricating oil content, the NTC behavior can be observed again, which is characterized by an almost vertical curve.

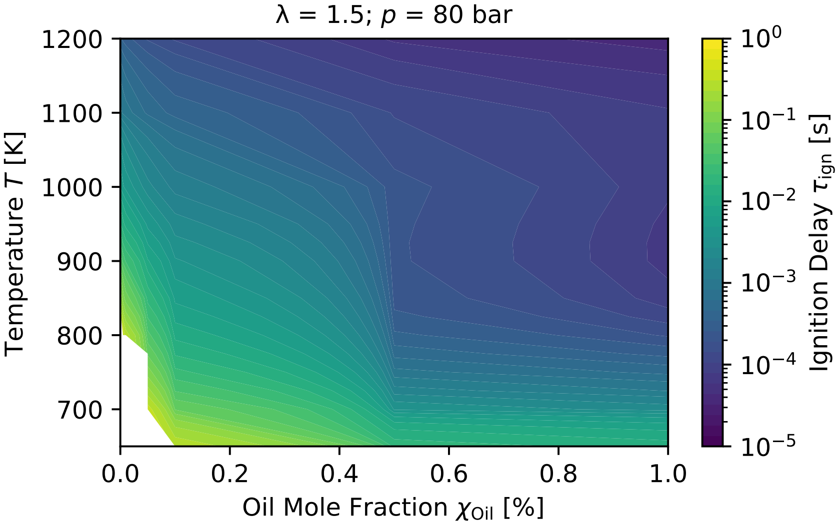

Figure 3.14: Ignition delay with oil and temperature variation for $\lambda = 1.5$, $p = 80\,\text{bar}$ and fuel = CH_4.

In summary, a temperature increase over wide ranges affects the ignition delay more than the oil concentration. However, this is no longer the case at higher lubricating oil concentrations in the NTC behavior range. This study also shows that the pre-ignition model has to be very sensitive to temperature. Even minor deviations in the measurement as boundary conditions lead to different results in the simulation.

3.3 Influence of Laminar Burning Velocities

In order to be able to assess the flame propagation after pre-ignition, calculations are carried out to determine the laminar burning velocity s_L. At this point, it must be mentioned that flame propagation after pre-ignition is not the core of this thesis and is roughly investigated in this section. Although the calculations are also carried out with Cantera, the method for determining and calculating laminar burning velocities will not be discussed further here. The method can be found in the thesis of Crönert [19]. To investigate and discuss the influence of oil on the laminar burning velocity, variations of pressure p, temperature T and AFER λ are performed. To keep the computation time reasonable, the Polimi_C1-C16_HT [83, 84, 82] is used, containing 368 species and 14462 reactions. This mechanism can only represent HT chemistry, which is sufficient for calculating laminar burning velocities. The computation times are massively shortened by this but are about one hour per operating point.

Figure 3.15 shows the pressure variation at $\lambda = 1$ and $T = 800\,\mathrm{K}$. This temperature value is chosen because it is close to a realistic value for the temperature of the unburned air-fuel mixture. The laminar burning velocity decreases with increasing pressure. Except for the low-pressure ranges, the variant with 100 % oil burns 50 % faster than 100 % methane from a pressure of 25 bar. An oil admixture of 0.1 % to the methane has hardly any effect on the laminar burning velocity. An increase to 1 % oil is also visible, but the difference is negligible. At high pressures above 100 bar, the laminar burning velocity changes only minimally.

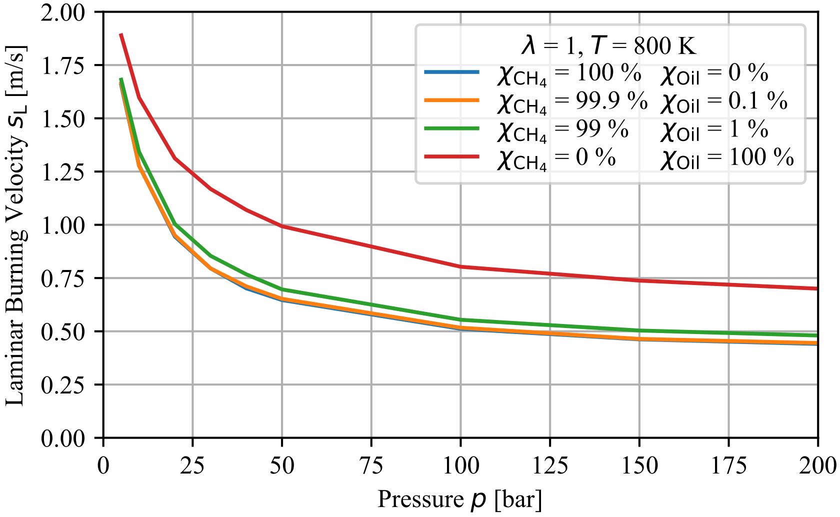

Figure 3.15: Pressure variation for the laminar burning velocity at $\lambda = 1$ and $T = 800\,\mathrm{K}$.

In fig. 3.16, the laminar burning velocity is plotted over temperature at $\lambda = 1$ and $p = 50\,\text{bar}$. With increasing temperatures, the value of the laminar burning velocity also rises. If only oil is used as fuel, the value is also higher than with pure methane. However, the distance is no longer as constant as for the pressure variation and continues to increase as the temperature rises. Small amounts of lubricating oil also have a minimal effect, analogous to the pressure variation.

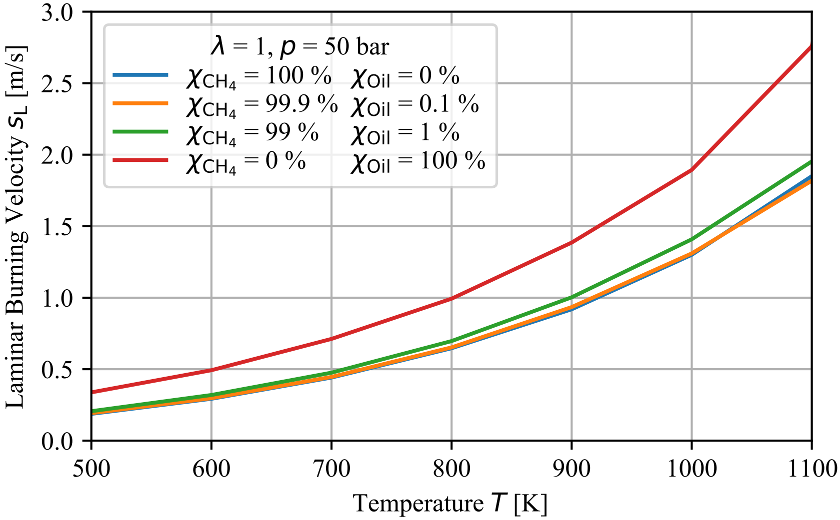

Figure 3.16: Temperature variation for the laminar burning velocity at $\lambda = 1$ and $p = 50\,\text{bar}$.

For the AFER variation in fig. 3.17, pressure and temperature are chosen to be $T = 800\,\text{K}$ and $p = 50\,\text{bar}$ constant. Again, similar behavior is observed - the oil burns faster than methane. The result is surprising for the case with 1 % oil, since the curve is slightly offset and has its maximum at $\lambda = 1$. Unfortunately, an explanation for this cannot be given at this point. The laminar burning velocity is quite low from $\lambda = 2.25$. Depending on the boundary conditions in the combustion chamber, typical flame propagation can no longer be assumed here. With the influence of lubricating oil, this limit can be shifted toward a lean AFER.

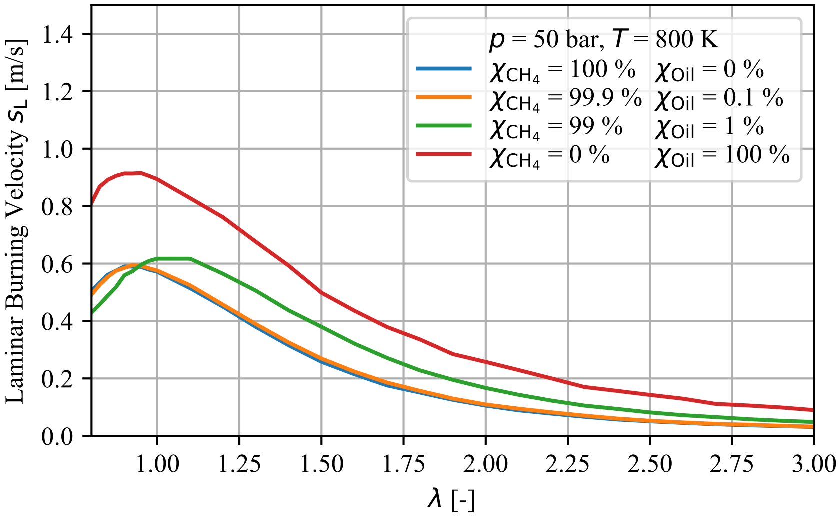

Figure 3.17: AFER variation for the laminar burning velocity at $p = 50\,\text{bar}$ and $T = 800\,\text{K}$.

These calculations are carried out to assess the flame propagation after a previous pre-ignition. For a typical 2-zone combustion simulation, the laminar burning velocity is used to calculate the flame propagation together with other parameters such as turbulence level and characterizing quantities for the flame. A fast or slow laminar burning velocity will lead to a faster or slower flame propagation under otherwise identical boundary conditions.

The investigations show that the oil influence has a relatively negligible effect on the laminar burning velocity, especially at low concentrations. From the ignition delay times, it can be seen that lubricating oil ignites already at lower temperatures. How radicals from the earlier lubricating oil combustion affect the laminar burning velocity still needs to be investigated. Also, whether the oil droplets can provide the minimum ignition energy to ignite the mixture must be further analyzed.

In summary, it can be said that flame propagation occurs at about the same rate with or without lubricating oil when the mixture ignites. The time at which ignition or pre-ignition occurs will be investigated in more detail in the following chapters.

3.4 Conclusion of the Analysis

In this chapter, the thermodynamics and reaction kinetics of the ignition process is analyzed. A methodology is presented with which various influences on ignition can be considered with detailed reaction kinetics. Ignition can be determined with four different criteria. Two criteria are temperature-dependent and two are dependent on the concentration of the $^{\bullet}$OH radical that occurs during the conversion of hydrocarbons. The temperature-dependent criteria are reached when the temperature exceeds the starting temperature by 300 K and 400 K, respectively. The $^{\bullet}$OH-dependent criteria are reached when the concentration reaches its maximum and at the second criterion, where the tangent of the gradient of increase intersects the time axis.

To represent the lubricating oil in the reaction kinetics, a lubricating oil substitute is determined. For this purpose, experience gained from investigations in the literature is used. As a result, the species n-hexadecane proved to be promising and is used as a lubricating oil substitute for this thesis.

In order to take long-chain hydrocarbons into account in the reaction kinetics, as is the case for the lubricating oil substitute, a reaction mechanism is required to model them. Therefore, different mechanisms that can handle hydrocarbons up to C16 are compared and analyzed. The POLIMI_TOT_NOx_1412 is chosen as the mechanism for this thesis because it is found to be very good for the combustion of methane which is essential for the combined analysis of lube oil and methane combustion.

For the reaction kinetics studies the EGR definition ”stoichiometric EGR” is used. This definition shows its advantages especially in the combustion of lean mixtures since O_2 which has not participated in the conversion of hydrocarbons is not added again by EGR. Also, the mass fraction of the inert gas remains constant in stoichiometric EGR while it decreases with increasing lambda in classical EGR.

Depending on the application, different reactor types of the 0D reactor can be used in the analyses. These differ in the use of ideal or real gas in the treatment of the gas behavior. In order to achieve results that are as close as possible to the actual phenomenon, only real gas behavior is used. For this gas law, it is possible to choose between an isochoric, i.e. at constant volume, or an isobaric, i.e. constant pressure, reactor. The analysis shows that the difference is relatively small and settles in the range of 10 %, where the isochoric has lower ignition delay times than the isobaric one. The real isobaric reactor type is chosen because it is closer to the actual behavior.

For this study, extensive investigations are carried out in the form of ignition delay calculations. With those calculations, engine influences on the ignition process, such as different fuels, pressure, temperature, AFER, EGR, and lubricating oil content on the ignition process are investigated. The elementary result of these calculations are that pre-ignition during regular engine operation is inconceivable without a lubricating oil influence. The oil is, therefore, necessary for pre-ignition. Pressure and temperature also significantly influence the ignition. However, fuel, AFER and EGR play a relatively minor role in this study's ignition process, which is not universally valid.

Finally, laminar burning velocities are calculated for methane and the lubricating oil substitute and in the mix of both components. The focus of this investigation is to give a rough estimate of whether the lubricating oil substitute affects flame propagation after a previous pre-ignition. For this purpose, a variation of temperature, pressure, and AFER is carried out. It is shown that in the complete range of the investigated area, the laminar burning velocity of the lubricating oil substitute hexadecane is higher than that of methane or admixture of oil. Extremely high concentrations above 5 % are not to be expected. However, these are usually in the region of 1 % lubricating oil content in the gas phase. The differences in laminar burning velocity are minor here and insignificant. How the flame propagates after pre-ignition must be studied in more detail.

4 Pre-Ignition Modeling

4.1 Droplet Evaporation

As part of this thesis, it is found that lubricating oil can cause pre-ignition in lean gas engines. To understand how this phenomenon occurs and what concentrations of oil are involved, a droplet evaporation model is implemented as part of the pre-ignition model. The main focus of the evaporation model is to estimate a lubricating oil concentration and the temperatures in the droplet and the gas phase. The previously mentioned parameters are the boundary conditions for the further modules of the model.

The methodology is presented in the following sections, and the special thermophysical properties are discussed. Furthermore, a validation of the model against literature values for natural and forced convection is shown. Finally, the droplet motion and the influence of the droplet size on the modeling are discussed. The limits of this approach are also explained.

4.1.1 Methodology

The ASM presented in section 2.4 is used and is implemented in Python, which means no commercial tools need to be purchased. All used software and libraries are based on open source. The differential equations eq. (2.19), eq. (2.20) and eq. (2.21) which describe the temporal change of size, temperature and evaporated mass are solved with the help of the SciPy library [102]. The Livermore Solver for Ordinary Differential Equations (LSODA) [79] is chosen as the algorithm.

All gaseous thermophysical properties are calculated with the Python implementation Cantera. The reaction mechanism for the transport properties is POLIMI_TOT_NOx_1412, which is selected in section 3.1.4. The thermophysical properties of the liquid phase are obtained from a database. The thermophysical properties are discussed in more detail in section 4.1.2.

4.1.2 Thermophysical Properties

The thermophysical properties, used for modeling, have a significant influence on the accuracy of the calculation. For this reason, a good data basis is crucial. All quantities with the index g or v, which are gaseous, are calculated with Cantera and the transport data of the reaction mechanism. Furthermore, the diffusion coefficient D, the density ρ, the dynamic viscosity η, the specific heat capacity c_p and the thermal conductivity κ in the gas phase of the droplet and the environment can be calculated directly with Cantera for each time step.

The thermophysical properties of the liquid phase of the droplet are taken from the NIST database. These are available in tabular form, and intermediate values are interpolated.

In order to show the influence of the databasis on the model, a comparison for the determination of the saturated vapor pressure is shown in fig. 4.1. The blue curve represents a section of the saturated vapor pressure curve used in this thesis [63], while the orange curve is calculated using the Antoine equation [3]

$$p_\mathrm{sat} = 10^{A-\frac{B}{C+T}}\,. \tag{4.1}$$

The coefficients for $nC_{16}H_{34}$ are listed in table 4.1 and are calculated by NIST [63] with data from Camin, Forziati and Rossini [14].

Table 4.1: Antoine equation coefficients for $nC_{16}H_{34}$, calculated by NIST [63] with data from Camin, Forziati and Rossini [14].

T **[K]**	***A*** **[-]**	***B*** **[-]**	***C*** **[-]**
463.2 - 559.9	4.17312	1845.672	-117.054

In section 2.4 the equations for the evaporation model are introduced. Here the calculation rule for the concentration of the evaporated substance in eq. (2.24) is shown. The saturated vapor pressure is divided by the ambient pressure. The effect on the modeling becomes apparent with the diagram since the values differ in some cases by more than 300 %, which, combined with the reaction kinetics presented in section 3.2.2, results in corresponding errors in the ignition delay times. Also, the values calculated with the Antoine equation cover only a small temperature range between 463.2 K and 559.9 K, while the values from the database are defined up to the critical temperature T_c for n-hexadecane of 723 ±2 K [2].

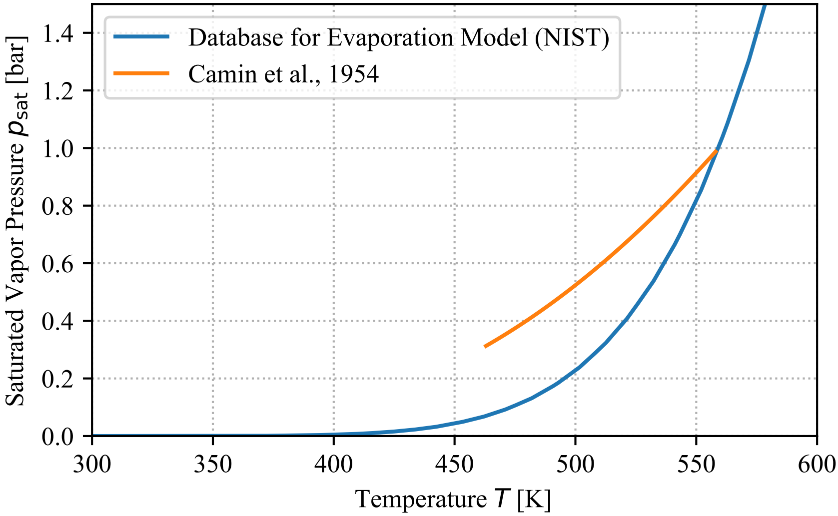

Figure 4.1: Comparison of the saturated vapor pressure between the values from the NIST [63] database used in the model and the values calculated using the Antoine equation [14].

4.1.3 Validation of the Droplet Evaporation Model

The model is validated in this section to test the droplet evaporation model's validity and suitability for the pre-ignition model. With a test in a constant volume chamber at the FHNW, measurements with single droplets are carried out. The optical detection and evaluation of the evaporation rate turned out to be very difficult, so that this test did not lead to the desired success. Therefore, literature values are used instead. However, the selection of literature for longer-chain hydrocarbons, as required for the lubricating oil substitute, is relatively limited. Validation of the droplet evaporation model is performed both with flow influence (forced convection) and without (natural convection).

Natural Convection

For the literature comparison in natural convection, the paper of Chauveau et al. [16] is chosen. In this publication, a C_7H_{16} droplet is suspended from a cross-fiber under normal gravity conditions. The droplet is introduced with the help of a piezo injector at the point where the fibers cross. The quartz filaments have a diameter of 14 μm. In this type of experimental setup, the heat input via the suspension points should be as low as possible.

The environmental conditions are atmospheric pressure and nitrogen (N_2) environment, so the droplet cannot oxidize or ignite. As soon as the droplet is exposed to ambient conditions, the temporal change of the droplet is recorded by a high-speed camera and is subsequently evaluated. It must be taken into account that the measurement accuracy for determining the droplet diameter is ±3 %. A temperature variation is carried out at 473 K, 548 K, 623 K and 748 K against which the simulation is subsequently validated. The starting drop temperature is 300 K and the diameter of the drop is 500 μm at the beginning of the experiment.

Figure 4.2 shows the transferred measurement results from Chauveau et al. [16]. Typically, the normalization to the initial droplet diameter is shown for evaporation investigations. The result is a straight line and is also called D^2-law.

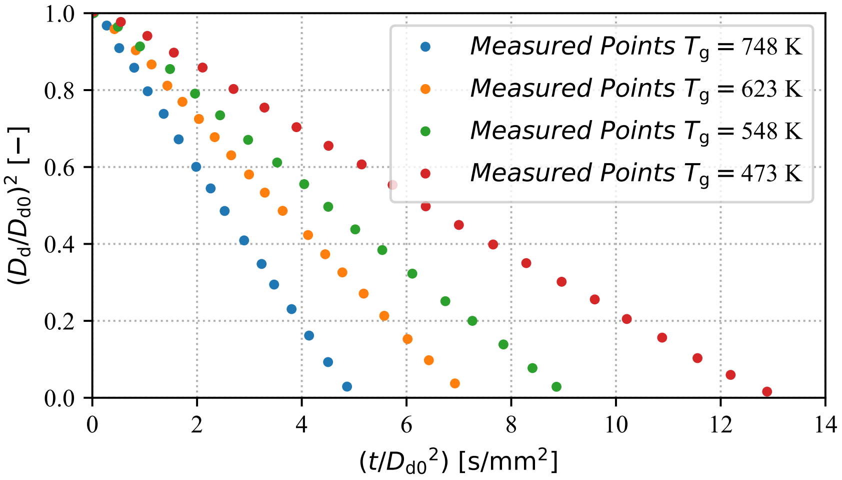

Figure 4.2: Measured droplet evaporation at different ambient temperatures T_g, $T_d = 300$ K, $D_d = 500\ \mu$m and species = n-heptane from [16].

In the following section, the four measured curves are compared with the calculated values of the evaporation model. During evaporation, the droplet temperature T_d asymptotically approaches a fixed temperature. This temperature behavior shows that the heat flux entering the droplet is as large as the energy removed from the droplet by the evaporation enthalpy. An equilibrium is therefore reached.

The wet-bulb temperature T_{wb} is used to compare the droplet temperature with the literature values. T_{wb} is estimated by Pinheiro and Vedovoto [80] based on the paper of Yuen and Chen [114]. In this publication, the droplets' wet-bulb temperatures are provided and plotted as a constant temperature in the diagrams.

Figure 4.3 shows the literature comparison at an ambient temperature around the drop T_g at 473 K. As it can be seen, the droplet evaporates more slowly than predicted by the modeling. At the beginning of the evaporation, measurement and simulation are still very close. After about two-thirds of the drop has evaporated, the deviation becomes slightly more prominent. In general, however, the agreement is given. Looking at the droplet temperature, it becomes clear why the faster evaporation occurs in the model. The resulting droplet temperature is about 3 % higher than the temperature of the measurement. However, the temperature prediction is sufficiently accurate.

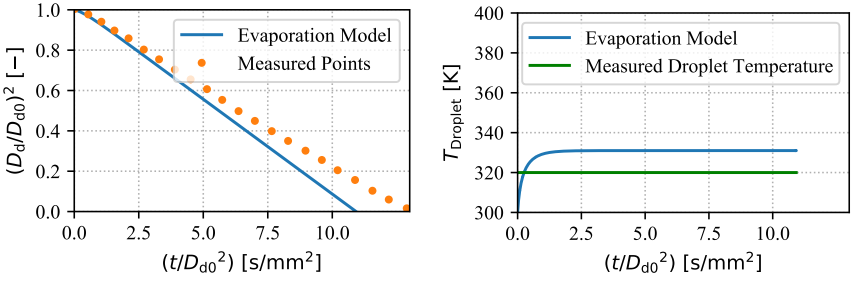

(a) Evaporation at $T_g = 473$ K **(b)** Droplet Temperature T_d at $T_g = 473$ K

Figure 4.3: Validation of evaporation and droplet temperature against measured data at $T_g = 473$ K from [16].

Figure 4.4 also shows the literature comparison, in this case at a higher temperature around the droplet, which is 548 K. Here the typical evaporation process occurs in the form of the D^2-rule, too. Both evaporation and temperature are predicted almost perfectly by the developed model and agree with the measured values. The measured droplet temperature is slightly lower than the calculated one, resulting in minimally faster evaporation than the measurement. In summary, the agreement between simulation and measurement is excellent.

The third comparison shown in Figure 4.5 is at an ambient temperature of 623 K. Again, the simulation and measurement results agree very well.

The fourth literature comparison, shown in Figure 4.6, takes place at the highest temperature of 748 K. This temperature is in a range that is relevant for the engine simulation, as it is approximately in the region of a typical compression end temperature. At this temperature, the model predicts slower evaporation than the measurement shows. This is also reflected in the higher measured temperature. Nevertheless, the measurements and the simulation are close.

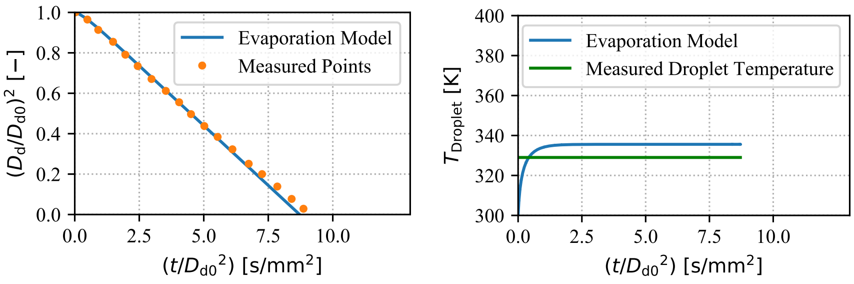

(a) Evaporation at $T_g = 548$ K.

(b) Droplet Temperature T_d at $T_g = 548$ K.

Figure 4.4: Validation of evaporation and droplet temperature against measured data [16] at $T_g = 548$ K.

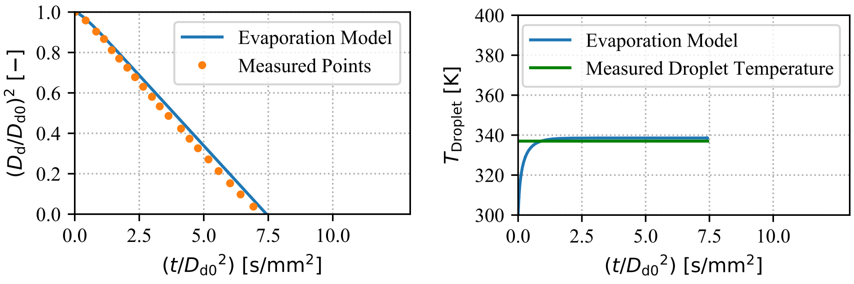

(a) Evaporation at $T_g = 623$ K.

(b) Droplet Temperature T_d at $T_g = 623$ K.

Figure 4.5: Validation of evaporation and droplet temperature against measured data [16] at $T_g = 623$ K.

The use case for droplet evaporation is to generate boundary conditions for the pre-ignition model. Minor deviations in the evaporation do not have such a substantial effect on the overall model. In general, the differences between measurement and model can be explained by the measurement accuracy of droplet diameter and temperatures. However, deviations also arise due to the physical and thermodynamic parameters used as input values for the calculation. These are only as accurate as supplied by the database or stored in the reaction mechanism. In this comparison, it should be noted that all droplet temperatures are well below the boiling temperature of heptane, which is at $T_b = 371.53$ K.

Therefore, the ASM is valid for this calculation. A further comparison is made against literature values to confirm the model's validity. The difference lies in the significantly lower temperature delta between droplet temperature T_d and the ambient temperature T_g. The evaporation rates are accordingly significantly longer.

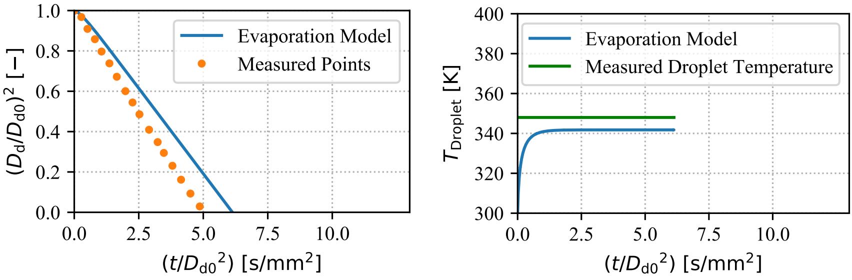

(a) Evaporation at $T_g = 748$ K. **(b)** Droplet Temperature T_d at $T_g = 748$ K.

Figure 4.6: Validation of evaporation and droplet temperature against measured data at $T_g = 748$ K from [16].

Figure 4.7 shows the evaporation rate of the model and the comparison with the findings of Daïf et al. [25]. It can be seen that evaporation takes significantly longer at the low-temperature delta of 4 K between the droplet and ambient temperature than in the previous figures. A direct comparison is only conditionally permissible due to the different boundary conditions, such as the droplet diameter. For the evaporation of 80 % of the drop, approx. 130 s are required.

The calculated evaporation, which is represented by the blue curve and has a temperature of 294 K as a boundary condition, predicts a longer evaporation time than the measurement. However, Daïf et al. indicate that ”all temperature measurements are made with an emissivity of 0.95. Measurement accuracy on temperature given by the manufacturer is ±2 %” [25].

For this reason, a 2 % higher temperature is applied as a boundary condition for the orange curve. As a result, the curve now fits the measurements better. Nevertheless, the temperature sensitivity in calculating the droplet evaporation can be seen again. A few kelvin difference in temperature lead to very different evaporation rates. This comparison also shows a good agreement between measurement and calculation. It is shown that the model can predict evaporation at high and low-temperature differences in a physically correct way.

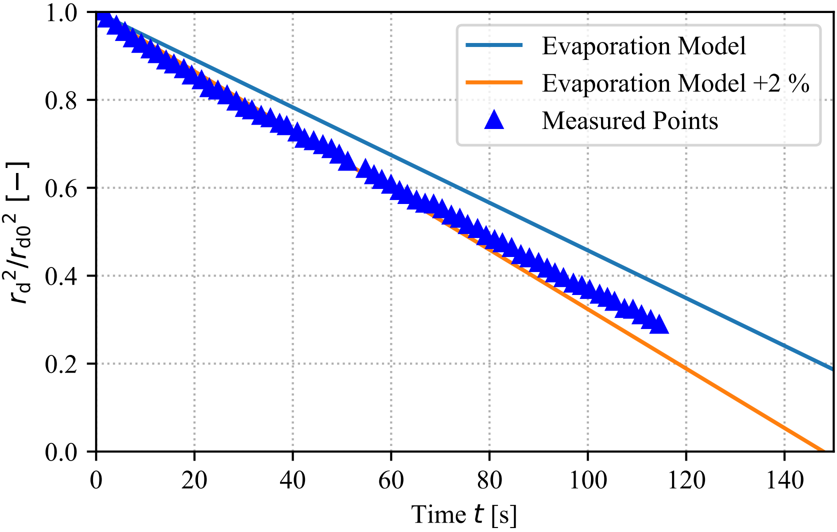

Figure 4.7: Validation of droplet evaporation with natural convection against measured data [25]. $T_\mathrm{d} = 290\,\mathrm{K}$, $T_\mathrm{g} = 294\,\mathrm{K}$, $D_\mathrm{d} = 1.386\,\mathrm{mm}$ and species = n-heptane.

Forced Convection

To validate the droplet evaporation with flow influence, a comparison with the work of Daïf et al. [25] is performed. In order to make the validation against literature uniform, the species n-heptane is also used here as the substance to be evaporated. Unfortunately, it is also difficult to find literature values for a longer-chain hydrocarbon. Since the thermal and physical data for the modeling all come from the same database and only the applicability of the modeling is shown, it can also be expected that the validation for other species will also fit very well.

Figure 4.8 shows the time evolution of the droplet radius r_d for the heptane droplet in comparison between measurement and simulation. The boundary conditions for the measurement are a start droplet diameter $D_\mathrm{d} = 1.052$ mm, a start droplet temperature $T_\mathrm{d} = 290$ K and $T_\mathrm{g} = 356$ K as ambient gas temperature. The diameter at the start is measured by Daïf et al. at the first image [25]. The flow velocity is given as $u_\mathrm{g} = 3.2$ m/s.

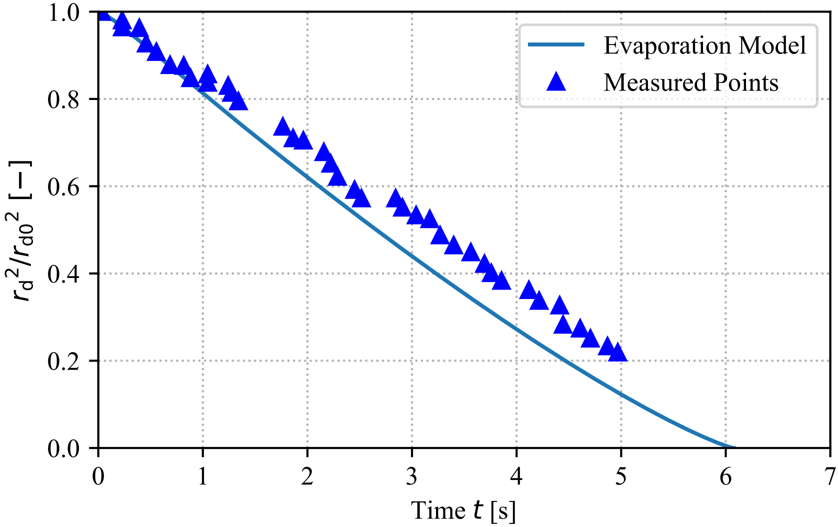

Figure 4.8: Validation of droplet evaporation with forced convection of u_g=3.2 m/s against measured data [25]. $T_\mathrm{d} = 290$ K, $T_\mathrm{g} = 356$ K, $D_\mathrm{d} = 1.052$ mm and species = n-heptane.

As can be seen, the calculation fits very well with the measured values. The slight deviation between simulation and measurement is also partly related to measurement inaccuracies. The inaccuracy in the temperature recording is given with ±2 %, and the deviation in evaluating the droplet diameter is ±3 %. Temperature deviations, however, have a more considerable effect on the result since the temperature sensitivity, i.e. the temperature influence on the evaporation, is relatively significant, especially with the minor differences between the droplet temperature and the environment.

In summary, it can be said that the droplet evaporation model fits the measurements from the literature very well both for the case of natural convection and with forced convection. The modeling can therefore be integrated into the pre-ignition model, and plausible results can be expected.

4.1.4 Influence of Flow and Droplet Movement

The slip velocity between drop and environment can be specified in the model if this boundary condition is known. It should be noted in advance that the investigations on the test facility show that the lubricating oil is moved along with the prevailing flow directly after it is introduced into the combustion chamber. In this case, the slip velocity is only present for a short time at the beginning and then drops to zero. Basu et al. [9] also show that the diesel engine range's droplet-gas slip velocity is minimal. Kaltz [54] also shows in her experiment with an incident flow of 500 m/s at a high-pressure environment of 200 bar that the slip velocity is negligible for tiny droplets. Therefore, the expected flow velocities in this thesis are significantly smaller. Also, Stårner et al. [96] show that the droplets have a similar velocity to the carrier flow. Thus, the slip velocity can be neglected as expected. Nevertheless, the model can simulate this influence if necessary. The flow conditions are taken into account in the Reynolds number and calculated with eq. (2.29). This dimensionless number is, in turn, used to calculate the Nusselt number (eq. (2.31)) and Sherwood number (eq. (2.30)), which affect the determination of the instantaneous droplet evaporation rate (eq. (2.40)).

It can be observed that the influence of flow and droplet motion affects the model as follows: Firstly, as shown in section 4.1.3, it leads to faster droplet evaporation. Secondly, it also leads to a slight thinning of the lubricating oil concentration because the flow cools the droplet since heat is extracted from it by evaporation enthalpy. Finally, the lower droplet temperature leads to a lower vapor pressure, resulting in a lower oil concentration since equilibrium conditions are assumed, as shown in eq. (2.24). In the sensitivity analysis in section 4.4, these factors are discussed and analyzed with examples.

4.1.5 Influence of Droplet Size

The vapor concentration calculation is of particular importance for the modeling. A saturated state, i.e. equilibrium condition, is always assumed in the model approach, as can be seen in eq. (2.24). For smaller droplet sizes below 50 μm, as shown by Miller, Harstad and Bellan [72], equilibrium conditions can no longer be assumed. If necessary, a better prediction of the droplet lifetime can be achieved by taking non-equilibrium effects into account, but this is not investigated. Also because Pinheiro and Vedovoto [80] show that, when comparing the equilibrium approach of this thesis and the non-equilibrium approach, the vapor concentration is identical even for a wide range of droplet sizes. In this thesis, droplet sizes between 10 μm and 500μm are investigated. In addition, it can be seen that the value of the vapor concentration is also identical between the different droplet sizes, and therefore the droplet size is also irrelevant to the vapor concentration. For the boundary condition from the droplet evaporation model, this means that as long as a droplet is present and evaporates, the same concentration will occur. For this reason, the droplet size does not influence the pre-ignition as long as the droplet is large enough for the modeling. The latter influence will be discussed in section 4.1.6 and in the sensitivity analysis in section 4.4.

4.1.6 Limits of Modeling

For modeling, a few limiting factors need to be considered to understand what the model can do and where it may reach the end of its capabilities. Starting with the droplet property itself, there are limits to the droplet size in several respects. For very small droplets below 50 μm, equilibrium conditions for evaporation can no longer be assumed [72]. The modeling would have to represent non-equilibrium conditions, as is typical for spray modeling. However, this is unnecessary for the model created since the droplet size must be chosen larger as a boundary condition. As shown in the sensitivity analysis in section 4.4 and also addressed in section 4.1.5, the droplet size does not play a significant role in the model. The droplet must be chosen large enough to persist through the compression phase in order to be able to calculate an oil concentration in the gas phase at any time. A droplet diameter of 100 μm is established as a good starting value. This can, of course, be specified flexibly as a boundary condition. The modeling differs in the range of application since larger droplets are assumed which do not evaporate completely during compression but continuously provide gaseous oil which mixes with the surrounding air-fuel mixture. The fact that the oil drops in the large engines then start to burn under the corresponding boundary conditions and have not completely evaporated and mixed with the environment is also proven by Unfug and Weisser [99] with optical measurements.

As a droplet evaporation model, the ASM is chosen as a relatively simple approach since the equilibrium condition, and the ambient temperatures are used to calculate an approximate oil concentration. Since this model is also used in spray modeling, it is more than sufficient for the application used here. Due to the simplicity of this model, some high pressure effects are not taken into account. These include liquid-phase solubility of gases, variation of gas- and liquid-phase properties with pressure, and gas-phase nonidealities. In the literature [66, 23, 22, 111, 116], there are approaches to consider these effects. However, implementing them would be excessive for the application in this thesis, since the focus is not on a perfectly modeled droplet evaporation. Also, the difference is almost negligible since the drop burning time of a high-pressure model is almost the same as a conventional low-pressure model, as Lazar and Faeth [61] and Canada and Faeth [15] have found.

Furthermore, the analysis in section section 3.2.1 shows that the ignition delay times decrease with higher pressure. Matlosz et al. [67] show that liquid-phase gas solubility has a negligible effect on the ignition delay time. Also, no apprupt change in the ignition phenomenon is observed when the ambient pressure exceeded the critical value. Another important finding is provided by numerical and experimental investigations [43, 55, 77, 32], which show that when the droplet is introduced into an ambient condition where temperature and pressure exceed the thermodynamic critical point, the critical mixing point does not occur immediately. Also, most studies show that the droplet surface reaches the critical mixing states at pressures much higher than the critical pressure of the fuel [116].

To answer the question whether the model and thus a classical evaporation process is admissible, the results of Crua et al. [20] and Gong et al. [44] are decisive. Gong et al. has investigated the evaporation process of the lubricating oil substitute n-hexadecane at ambient conditions, between 40 bar and 360 bar and between 750 K and 3600 K, which covers areas in the subcritical and supercritical range. He shows that, for example, at the boundary conditions of 900 K and 90 bar, classical evaporation is given. At lower pressures of 75 bar, this behavior is still present even at 1000 K, which is above the boundary conditions relevant for this thesis. This statement is confirmed by Crua, Manin and Pickett [20], who performed experiments with a high-speed camera. In their paper, n-hexadecane single droplets are introduced at 907 K and 79 bar, and they show that ”all droplets converge to spherical shapes, with their diameters progressively reducing. This behavior is characteristic of a classical evaporation process, even though the conditions are above the critical point of n-hexadecane.” [20]

The data basis significantly influences the model accuracy. The NIST database [63] for liquid phase properties, used in this thesis, is comprehensive and covers the required parameter range. For the gas phase, where especially the diffusion coefficients have an influence, the reaction mechanism selected in section 3.1.4 is used. A prerequisite for the calculation of this is a mechanism with transport data. The values can only be as good as the mechanism provides them.

In general, it can be concluded that excellent results are generated with this approach. However, if it is later determined that the model achieves inaccurate results for a different application, the lubricating oil concentrations can also be specified in tabular form, for example. For the intended application, it works satisfactorily.

4.2 Chemical Ignition Delay

After the drop evaporation model is used to calculate the temperature and the lubricating oil concentration in the gas phase as a function of time, respectively, the crank angle, the time profile is divided into equal periods. At each period, ignition delays are determined using the boundary conditions present with detailed reaction kinetics. These are calculated using the 0D-reactor described in section 2.3.2. For this purpose, the gas composition is determined in advance from the lubricating oil concentration, AFER, temperature, and pressure and transferred to the reactor. Then the ignition delay time is calculated as shown in the investigation of chapter 3. ”Real isobaric” is selected as the reactor type.

In other words, real gas behavior and a constant pressure is used for the modeling. Finally, the simulation results are returned to the model and represent the reaction kinetic part of the modeling. The integration of the chemical ignition delay and how this interacts with the pre-ignition model is explained in more detail in the next section.

4.3 Combination to the Pre-Ignition Model

This section shows how the individual sub-models, such as the droplet evaporation model and the reaction kinetics, are combined to the phenomenological pre-ignition model which is already presented in [109],[108] and [107]. For the explanation, an arbitrary example is chosen in comparison with the measurements performed for this thesis at a test facility. The extensive validation and comparison with the measurement results are explained in detail in chapter 5. The example is at the boundary conditions of 800 K and 70 bar at the end of compression and an AFER of $\lambda = 1.5$. An initial droplet diameter of 100 μm is selected, and an SOI of -50 °CA at which the droplet is introduced into the combustion chamber.

Figure 4.9 plots the three temperature ranges of the droplet evaporation model. T_s is the droplet surface temperature of the liquid phase. As can be seen, it starts at about 453 K, which corresponds to the initial droplet temperature measured on the test rig. T_g is the temperature of the surrounding gas phase that enters the model as a boundary condition as the measured temperature curve from the test facility. The reference temperature T_mix is calculated by eq. (2.22), as shown in section 2.4, and represents a variable for the droplet evaporation model.

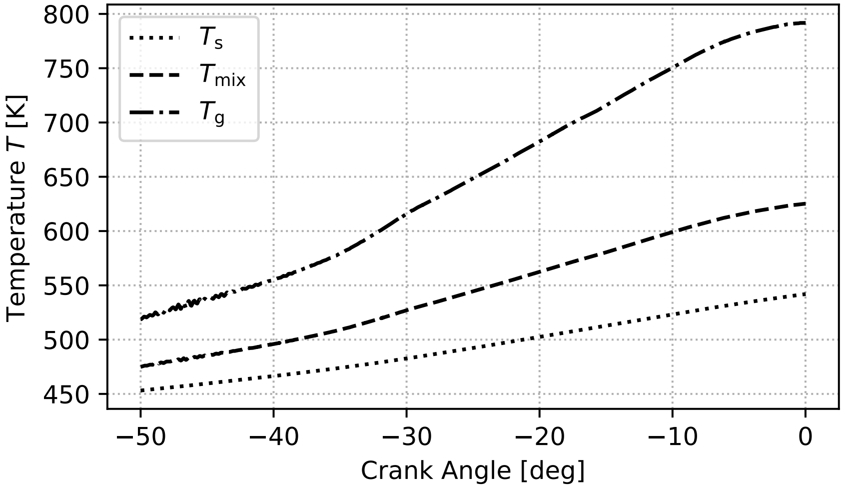

Figure 4.9: Temperature profiles calculated by the droplet evaporation model with an SOI of -50 °CA, temperature and pressure at the end of compression of 800 K and 70 bar and an AFER of $\lambda = 1.5$.

With the temperature previously calculated, the saturation vapor pressure p_{sat} is interpolated at each time step using database values. Since saturated conditions are always assumed in the evaporation model, eq. (2.24) can be used to calculate the concentration of the oil X_{oil} in the gas phase. The concentration curve for the SOI of -50 °CA used as an example is shown in fig. 4.10. The pressure curve required for the calculation is also measured on the test rig and is included in the modeling as a boundary condition.

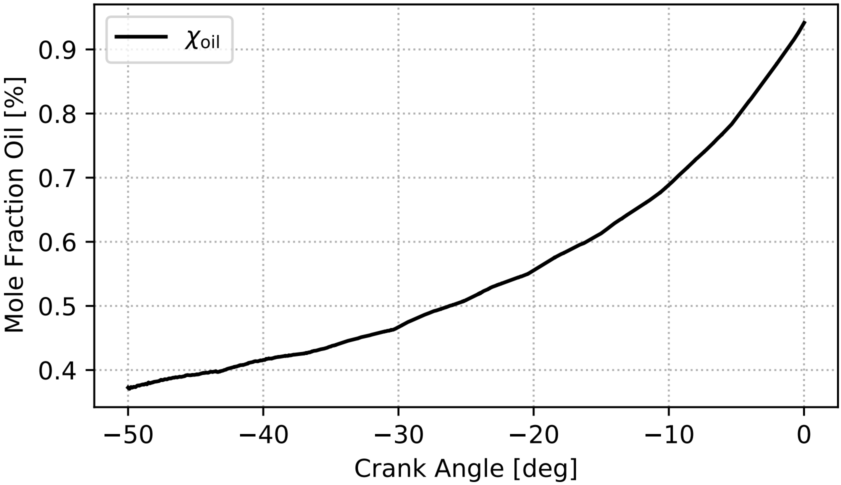

Figure 4.10: Lubricating oil concentration curve calculated by the droplet evaporation model with an SOI of -50 °CA, temperature and pressure at the end of compression of 800 K and 70 bar and an AFER of $\lambda = 1.5$.

With the boundary conditions calculated by the evaporation model, such as temperature and oil concentration, the ignition timing is calculated with detailed reaction kinetics. For this purpose, ignition delays are calculated in adjustable sections with the currently valid boundary condition. Figure 4.11 shows a representation in which the evaporation and reaction kinetics are combined. The solid line shows the weight of the evaporating droplet, which decreases over time. The dashed line shows the chemical ignition delays calculated in the model in adjustable grids. If there are jumps or other unusual effects in the result, reducing the step size is worthwhile. The result from evaporation and reaction kinetics is shown as a star. At this time, the gaseous oil-air-fuel mixture will ignite. The result for this SOI operating point is the minimum value of the ignitions.

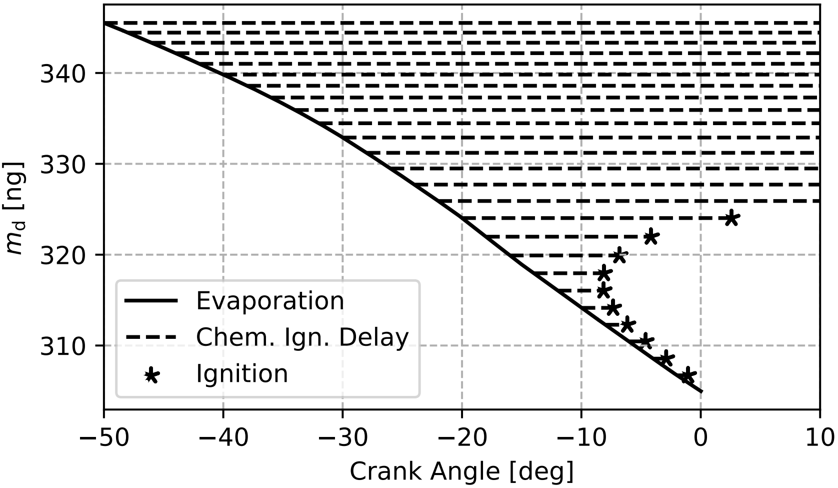

Figure 4.11: Combination of droplet evaporation and reaction kinetics with an SOI of -50 °CA, temperature and pressure at the end of compression of 800 K and 70 bar and an AFER of $\lambda = 1.5$.

The minimum value of the considered SOI of -50 °CA is marked in fig. 4.12 as a red star. This diagram already shows the measurement results from chapter 5, which will be discussed in detail later. The median of the measurements is marked as MED, and the standard deviation as Standard Deviation (SD). The ignition calculated by the phenomenological pre-ignition model is plotted as Ignition (IGN) in the diagram. The other black stars are the results of a calculated SOI variation. It is noticeable, without going deeper into the analysis, that the calculated values agree very well with the measured values. Especially in the lower SOI range <-60 °CA the calculated values are almost on the median of the measurements. This range is particularly relevant for engine applications, since it is to be expected that significant amounts of lubricating oil are already present in the intake air or are introduced into the combustion chamber by the lubrication system.

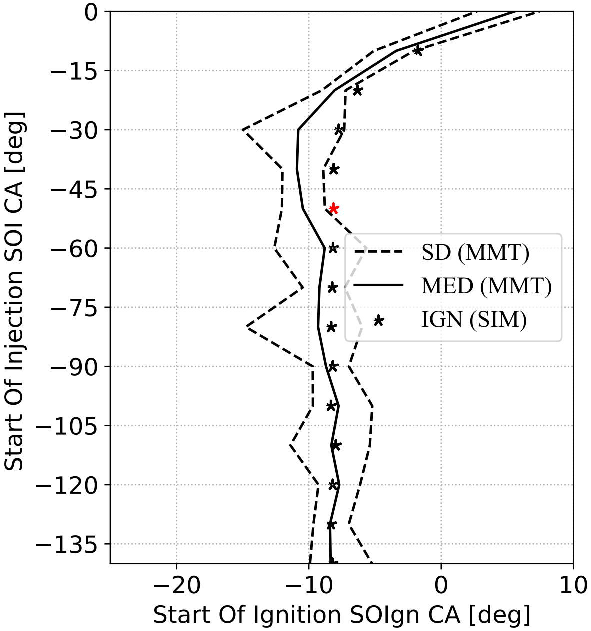

Figure 4.12: SOI variation and result of the exemplary calculation with an SOI of -50 °CA, temperature and pressure at the end of compression of 800 K and 70 bar and an AFER of $\lambda = 1.5$.

4.4 Sensitivity Analysis

The effect of various parameters on the model is examined through a sensitivity analysis. With this, it should be possible to recognize the influence of the individual boundary conditions on the model. For some cases, the sensitivity analysis also examines boundary conditions whose values are rather unrealistic for the real application. These values are discussed in the individual subsections and an explanation is given of how a conclusion can be derived from them.

4.4.1 Slip Velocity and Droplet Size

In the first study, the variation of the droplet size is coupled with the variation of the slip velocity between droplet and environment. As described in section 4.1.5, the droplet size alone would not provide much new information. However, in combination with the velocity influence, valuable insights can be obtained from the three diagrams below. The modulus of the two velocity vectors $|\vec{v}_{\mathrm{g}} - \vec{v}_{\mathrm{d}}|$, which represent the slip velocity between the droplet and the surrounding gas and are given in equation eq. (2.29), is varied between 0 m/s and 15 m/s.

Initial diameters of 10 μm, 100 μm, and 500 μm are chosen for the droplet size variation. The curve with 750 K at the end of the compression of the test rig is selected as the temperature curve, which will be discussed in more detail in section 5.2. For the AFER of methane as fuel, $\lambda = 1.5$ is chosen. The pressure at the end of compression is 70 bar for all subsequent analyses.

Figure 4.13 shows an SOI variation, i.e., the time in °CA at which a lubricating oil drop is introduced into the combustion chamber. The five curves represent a constantly forced convection between 0.01 m/s and 15 m/s and a curve without slip velocity. At this point, it must be mentioned that a constant velocity difference between the droplet and the surrounding flow is rather unrealistic. In the experimental setup, which will be described later, the drops are moved with the inner cylinder flow shortly after insertion. The slip velocity thus becomes 0 m/s or is not a constant value. In order to represent the flow conditions and achieve more accurate droplet motion modeling, more complex CFD simulations are necessary, which are not the focus of this thesis. However, it shall be shown that forced convection can be considered in the modeling and affects the result if the boundary condition is known.

As can be seen in the diagram, even slight flow differences effect the result. However, the difference between a slip velocity of 1 m/s and 15 m/s is marginal. The reason for the later pre-ignition in Start Of Ignition (SOIgn) becomes apparent when looking at the equations in section 2.4. Due to the air flow, the droplet evaporates more quickly, as shown in section 4.1.3. The droplet becomes slightly cooler with the forced convection resulting in lower vapor pressure at the droplet surface. Since the modeling always assumes a saturated state, it is clear that the lubricating oil concentration decreases as a result. A lower lubricating oil concentration leads to longer chemical ignition delay times in the reaction kinetics part of the pre-ignition model. This results in a later SOIgn, as shown in the diagram.

However, the influence is relatively small and is only in the range of about 2 °CA. The droplets are moving along with the flow, so the relative velocity is almost 0 m/s, which results in a negligible effect on pre-ignition. Nevertheless, the flow characteristics affect the flame propagation after pre-ignition, but this will not be further investigated.

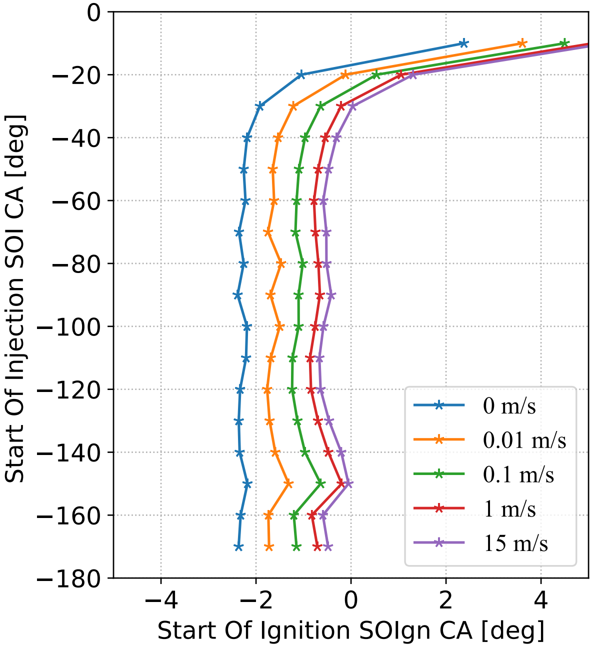

Figure 4.13: Sensitivity analysis for slip velocity and droplet size at a droplet diameter of $D_\mathrm{d} = 500\,\mu\mathrm{m}$, $T_\mathrm{EOC} = 750\,\mathrm{K}$, $p_\mathrm{EOC} = 70\,\mathrm{bar}$ and $\lambda = 1.5$.

The sensitivity analysis at an initial droplet diameter of 100 μm is shown in fig. 4.14. As expected from the results obtained previously, the results are almost identical to the variant with a larger drop diameter. Slight differences and peaks result mainly from a not fine enough gradation of the boundary conditions for the chemical ignition delay, as can be seen in section 4.2 and section 4.3. As long as the droplet is large enough for a lubricating oil concentration to develop, the droplet size does not matter.

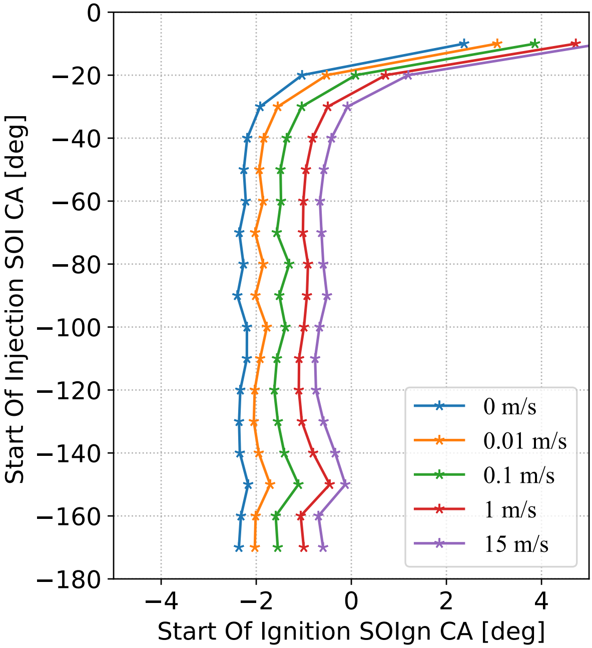

Figure 4.14: Sensitivity analysis for slip velocity and droplet size at a droplet diameter of $D_\mathrm{d} = 100\,\mu$m, $T_\mathrm{EOC} = 750\,$K, $p_\mathrm{EOC} = 70\,$bar and $\lambda = 1.5$.

The following fig. 4.15 shows the variation at a tiny initial droplet diameter of $10\,\mu$m. As already explained in section 4.1.6, the model requires a continuously evaporating droplet to calculate the oil vapor concentration at equilibrium. This is due to the model approach and is independent of the droplet size in reality. Since it is shown both in the model and on the test rig that the droplet size does not affect the start of pre-ignition, a droplet size large enough so that it does not evaporate entirely during the period under consideration must be selected for the desired calculation.

As can be seen in fig. 4.15, without slip velocity, the droplet evaporates at an SOI of -100 °CA. For this reason, calculations are no longer possible at earlier SOIs. However, it can also be seen that compared to the previous calculations, at larger initial droplet diameters, the value remains the same. If a slip velocity is applied, the droplet evaporates faster, as shown in section 4.1.3 and validated against measured values. Accordingly, the model can no longer calculate the oil vapor concentration at an earlier stage. As already mentioned, a larger droplet diameter must be selected for the simulation so that the model functions correctly even if smaller droplets occur in the real engine. Since the droplet size does not affect the result, this parameter is also not important as a variable and is only used by the model to determine the oil concentration in the gas phase.

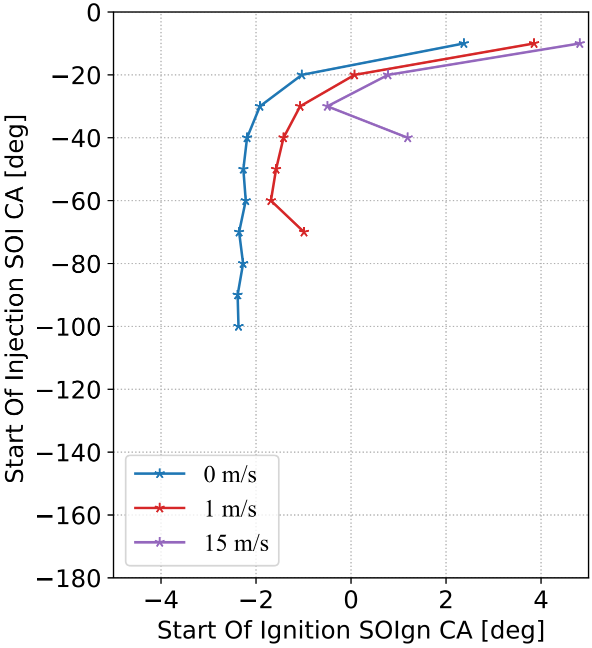

Figure 4.15: Sensitivity analysis for slip velocity and droplet size at a droplet diameter of $D_\mathrm{d} = 10\,\mu$m, $T_\mathrm{EOC} = 750$ K, $p_\mathrm{EOC} = 70$ bar and $\lambda = 1.5$.

4.4.2 Engine Speed Variation

For the sensitivity analysis of the pre-ignition model, an engine speed variation is performed. As in the previous analysis, the pressure and temperature curves of the Flexibility regarding Optical engine Combustion diagnostics and/or Sensing (Flex-OeCoS) test facility are used at a temperature of 750 K at the end of compression. However, two points should be noted for the interpretation of the results:

- First, as discussed in more detail later, the speed at the test facility is only comparable to an engine speed to a limited extent. The time dependencies are roughly comparable, but the speed is mainly used to set a turbulence level on the test rig.
- Secondly, all speed variations are calculated using the measured pressure and temperature curves of the 600 rpm variant as a boundary condition. Therefore, for the different speeds, other temperature gradients or temperature curves are expected, which also have a substantial effect on the pre-ignition phenomenon due to the strong temperature sensitivity.

If the limitations, explained above, are taken into account in the interpretation, it is nevertheless possible to gain insights from the variation.

The SOI variation calculated with the phenomenological pre-ignition model for different engine speeds is shown in fig. 4.16. With increasing engine speed, later pre-ignitions or starts of ignitions (SOIgn) occur. Even if the relatively large influence cannot be confirmed with certainty for the reasons mentioned above, an influence of the engine speed is expected. At low engine speeds, more time is available at critical pressure and, above all, temperature range to ignite the mixture. It also becomes clear that this type of pre-ignition is particularly critical for slow-running engines. At high speeds, there is simply not enough time at critical temperatures. Even with the influence of lubricating oil, the chemical ignition delay is too short to ignite the mixture in the relevant timespan. This is also the reason why this type of pre-ignition does not apply to passenger car applications. This is confirmed by Reimer et al. with the statement: ”From the length of the ignition delay for oil droplets in air, it could be concluded that an oil droplet in the engine combustion chamber cannot initiate a pre-ignition in the same working cycle.”[85].

In summary, low engine speeds favor pre-ignition. In the model, this is set as a parameter and influences the result. However, the variation shown must be viewed with caution for the reasons mentioned. Nevertheless, the basic effect of a change in engine speed is demonstrated in this analysis.

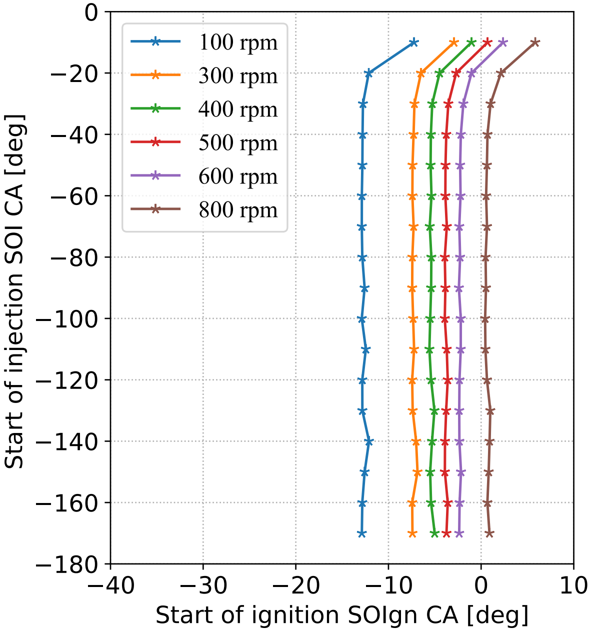

Figure 4.16: Sensitivity analysis for the engine speed at $T_{\mathrm{EOC}} = 750\,\mathrm{K}$, $p_{\mathrm{EOC}} = 70\,\mathrm{bar}$ and $\lambda = 1.5$.

4.4.3 AFER Variation

The impact of the AFER on the model is examined in this sensitivity analysis. For reasons of uniformity, the case measured on the test rig with a temperature of 750 K at the end of compression is selected again. Methane is used as fuel. An initial droplet diameter of 100 μm is chosen. The result of the SOI variation at different AFER is shown in fig. 4.17. The range $\lambda = 1$, $\lambda = 1.5$ and $\lambda = 2$ is shown, other air fuel ratios follow the same trend. In general, it can be seen that the AFER has a relatively small effect on the SOIgn.

On the other hand, it can be seen that ignition occurs earlier with lean mixtures. This result is not to be expected because, as shown in the ignition delay times in section 3.2.1, later ignition is to be expected with a lean mixture. Therefore, a further investigation is carried out to explain this effect, as shown in the following.

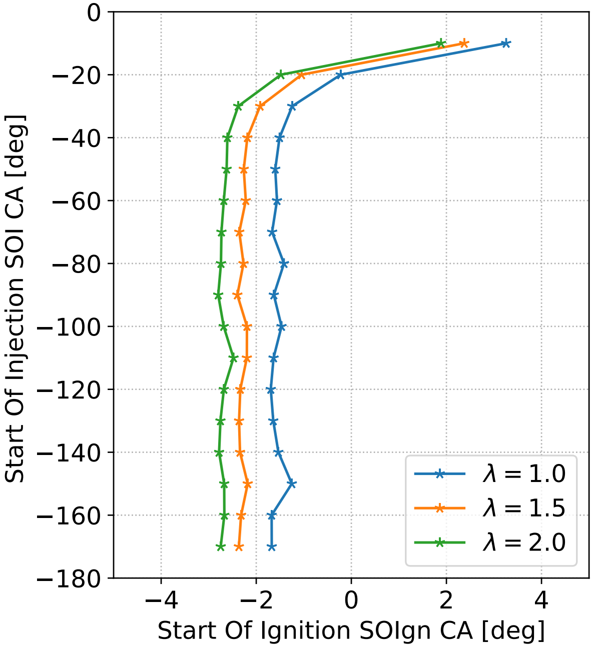

Figure 4.17: Sensitivity analysis for the AFER impact on the ignition at $T_{\text{EOC}} = 750\,\text{K}$, $p_{\text{EOC}} = 70\,\text{bar}$.

In order to explain the effect, ignition delay times are calculated using the methodology shown in chapter 3. The AFER is calculated using the same gradation as in the previous diagram. Methane is also the fuel used in this calculation. The oil concentration of 0.5 % corresponds to the concentration found in the previous AFER variation at ignition conditions. In order to exclude pressure as a cause for the observed inverse behavior for the ignition delay times, the calculation is also performed at 10 bar and 70 bar

Figure 4.18 shows the result of the chemical ignition delay calculation. The influence of pressure on ignition delay is as expected and also already extensively analyzed in section 3.2.1. Without oil, a lower ignition delay is seen almost universally for the pressure variation with a lower AFER. For the 10 bar case, this behavior reverses at a temperature of approximately 1150 K. However, this temperature and pressure range is not relevant for the behavior considered here.

In the curves with an oil content of 0.5 %, a behavior can be noted which answers the previously described behavior. It can be seen throughout that the ignition delays have reversed. A low AFER leads to longer ignition delay times than before without oil. Looking into the results from the AFR variation of the phenomenological model, it is noticeable that the ignition conditions are almost at the same temperature, pressure and oil concentration. However, between $\lambda = 1$ and $\lambda = 1$ the chemical ignition delay differs by about 16 % which explains the difference.

When looking at the ignition delay diagram, two further effects can be recognized which need to be analyzed. Firstly, with the influence of lubricating oil, a clear NTC behavior can be observed. At 70 bar, from approx. 830 K up to 1000 K with increasing temperature, there is no longer any reduction in the ignition delay time. For the model, this does not mean that the SOIgn can be expected to remain at the same level with increasing temperature. The chemical ignition delay may be the same, but the higher temperature changes the evaporation which leads to a different oil concentration which again affects the ignition delay as shown in section 3.2.2. The second effect that can be identified with lubricating oil influence is that the ignition delay is significantly less sensitive to pressure at lower temperatures below 710 K. At higher temperatures, the difference between 10 bar and 70 bar increases significantly. When comparing the two curves without oil, it can be seen that the difference in the logarithmic diagram between 10 bar and 70 bar is almost constant.

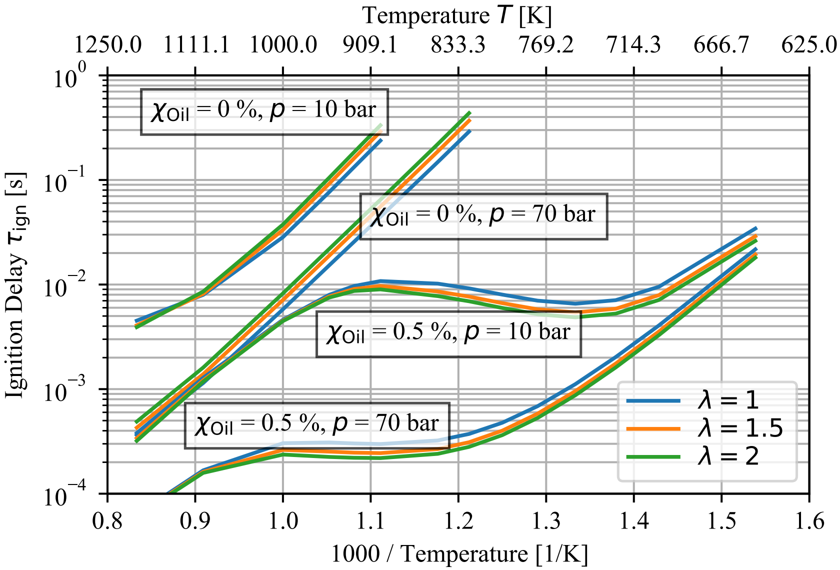

Figure 4.18: Ignition delays at a variation of the AFER, a pressure variation of 10 and 70 bar and a comparison without oil and the oil concentration of 0.5 % which corresponds to the concentration at ignition conditions in the AFER sensitivity analysis of the pre-ignition model.

4.4.4 Temperature Variation

The temperature at the end of compression is varied for the last sensitivity analysis. In order to obtain a realistic result, the measured pressure and temperature profiles of the Flex-OeCoS test facility are applied as a boundary condition for this variation. The design of this test facility is described in detail in section 5.2 later on. At this point, the effect of the temperature change will be discussed in more detail. The results of the phenomenological pre-ignition model for an SOI variation at the three temperatures at the end of compression of 750 K, 800 K, and 850 K are shown in fig. 4.19. A concise temperature influence can be seen, which underlines the already mentioned strong temperature sensitivity of the pre-ignition phenomenon. At this point, it can be summarized that the temperature has a very significant effect on the pre-ignition and has the greatest influence on all the parameters investigated and will be discussed later at several points, as it is a primary influencing factor for the pre-ignition.

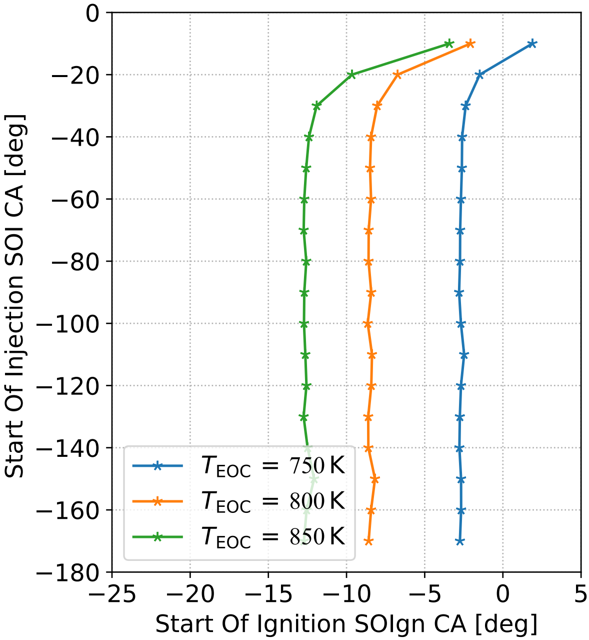

Figure 4.19: Sensitivity analysis for the temperature at the end of compression at $p_{\mathrm{EOC}} = 70\,\mathrm{bar}$ and $\lambda = 2$.

4.5 Model Robustness

Reaction kinetics is used to calculate over 150000 cases for parameter variation of pressure, temperature, AFER, EGR, oil quantity, and different fuels. All provided operating points from both the Flex-OeCoS test facility and the WinGD engine are calculated with the phenomenological pre-ignition model and compared against this measured data. Additionally, approximately eight hundred calculations are performed to analyze the model and identify sensitivities. When the minimum droplet size is selected, as discussed in section 4.1.5

and section 4.4.1, the model operates without problems and provides plausible results.

At this point, it must be said that there are usually many more operating points to consider in a passenger car application than in marine gas engines, where there are hardly any speed and load variations. Accordingly, as shown in section 5.2, only the relevant operating points are measured on the test bench due to the very complex and time-consuming optical evaluation procedures.

The model functioned very robustly at the operating points and in the tests considered for this thesis. Positive feedback is also received from industry participants who attended an event to test the model. Some of the participants have already tested the model for their applications.

Another important point is that the model does not require any tuning parameters, which is a unique feature in the 0D/1D environment. It has been shown, both in comparison with the test facility and on the WinGD engine, that the better the boundary conditions are known and can be measured, the better the model matches the measurement. The model is based on purely physical and reaction kinetic assumptions and is not fitted to measurement results.

Concerning the calculation time of the model, reaction kinetics is the main bottleneck. The long-chain hydrocarbons of the oil require a much more complex reaction mechanism, as shown in section 3.1.4. In the case of droplet evaporation, initializing the mechanism for the transport data and properties of the gas phase requires almost the entire time of the complete evaporation calculation. The reaction kinetics for ignition can be calculated in parallel on several cores, but it takes about 2 minutes per core per case. Therefore, there is already the consideration to implement this calculation map based to reduce the computation time.

In summary, it can be said that the model runs very robustly. Optimization potentials will show up in the case of intensive application, which will be integrated into the modeling if necessary.

5 Validation of the Pre-Ignition Model

5.1 Test Bench Setup

This thesis is carried out as part of a research project. All measurements, unless otherwise stated, are performed at the Institute for Thermal and Fluid Engineering (ITFE) at the chair of Prof. Kai Herrmann at the FHNW. An optically accessible engine test facility ”Flex-OeCoS” was developed – the designation indicating its Flexibility regarding Optical engine Combustion diagnostics and/or development of corresponding Sensing devices [89] to investigate in-cylinder phenomena of gas/dual-fuel combustion processes closer to engine-relevant conditions. It is perfectly suited for analyzing pre-ignition behavior, especially at low engine speeds, due to its flexible operating modes and its adaptability [49, 50].

The experimental setup ”Flex-OeCoS” is shown in fig. 5.1 (left). As shown, only cylinder three (the third cylinder from the right) is in operation, while the other three cylinders of the heavy-duty engine are deactivated. The optical setup on cylinder three is illustrated in more detail in fig. 5.1 (right). The configration shown is a DF combustion process, i.e., a lean premixed gas-air mixture ignited with a pilot. Engine-relevant operating conditions such as compression pressure and temperature, adjustable flow conditions, AFER, and a high procedure variance realized by a pneumatic valve train can be set.

The inlet valves can be seen in fig. 5.1 (right) where a premixed air/gas mixture is fed into the combustion chamber and then compressed. The two exhaust valves can be seen to the left and right of the pilot injection or, in the other configuration, next to the lubricating oil injection. For full flexibility of engine operation, the two intake and two exhaust valves can be controlled independently of the crankshaft position. In addition, different engine speeds can be applied, which allows the test bench to match the time scales of marine two-stroke engines in gas/dual-fuel operation. Due to the flexible individual setting of pressures, temperatures, AFER, and flow conditions, pre-ignition phenomena can be analyzed well, and the results provided for model development.

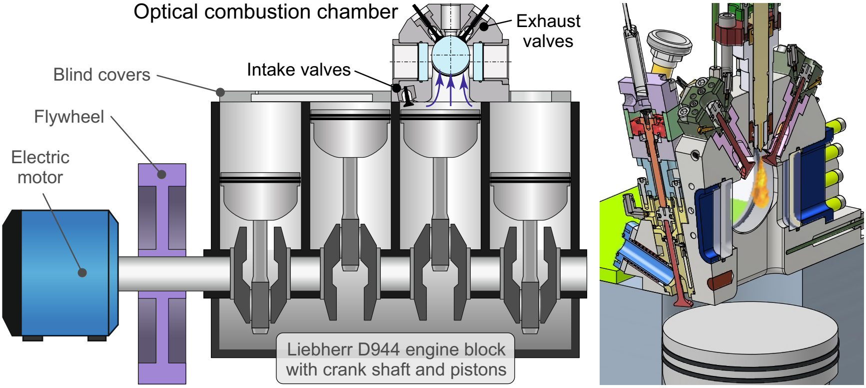

Figure 5.1: Concept of the ”Flex-OeCoS” test facility (left), operation specifications and dual-fuel configuration of the optically accessible combustion chamber (right) [110].

Optical accessibility is ensured by sapphire glasses, as shown in fig. 5.2 (left). The cylinder head is equipped with extensive measurement technology, such as pressure and temperature sensors, to record the boundary conditions needed for modeling. In addition to the possibility of heating the intake air, the cylinder head can also be heated to simulate behavior similar to actual engine operation. This is also done because only individual cycles are run; therefore, the cylinder head would cool down too much between the operating breaks. As a result, the boundary conditions would no longer correspond to a realistic engine. Unique instrumentation can also be used as an alternative to the glass window, such as fast thermocouples, pressure sensors for calibration, or heat flow sensors. Furthermore, hot spots or spark plugs can be used instead of side windows, as shown in fig. 5.2 (right). The single-hole injector for lubricating oil is variable conditionable to study pre-ignition effects.

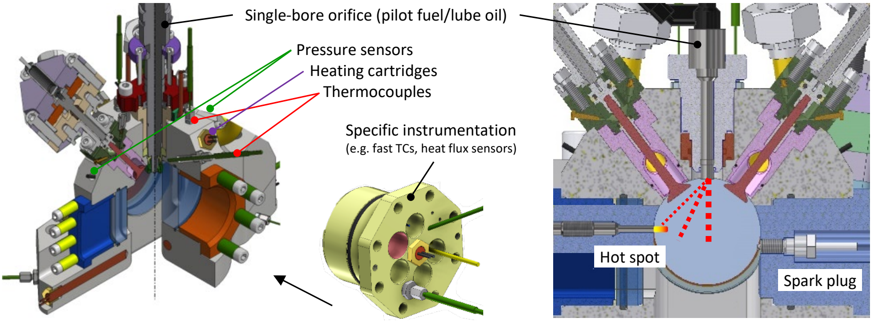

Figure 5.2: Instrumentation of the optically accessible combustion chamber and the possibility to adapt inserts for specific instrumentation (left) [53] or ”hot spot” and spark plug (right) [97] to enable lube oil addition by a distinct injector.

The detection and analysis of the pre-ignitions is achieved by a double application of Schlieren and $^{\bullet}$OH chemiluminescence. Figure 5.3 on the left shows the setup already in use for dual-fuel investigations [49]. In this Schlieren configuration, a collimated light beam passes through the two circular sapphire windows, which have a diameter of 60 mm, and is then filtered through a pinhole and captured by a high-speed camera. This covers almost the entire combustion chamber, which facilitates an analysis of the pre-ignition effect. Image acquisition is synchronized to the engine’s CA encoder, where for a typical speed of 600 rpm, a temporal resolution of 0.1 °CA (36 kHz) can be achieved. If a reduction of the image area is accepted, a frame rate of up to 200 kHz can be realized.

Figure 5.3 on the right shows sample images for an investigation with dual-fuel combustion processes. A second high-speed camera coupled to a high-speed image intensifier is used to record chemiluminescence of the $^{\bullet}$OH radical. The formation of $^{\bullet}$OH radicals is an indicator of ignition, which is also shown in chapter 3.1.2 and is therefore used as an ignition criterion.

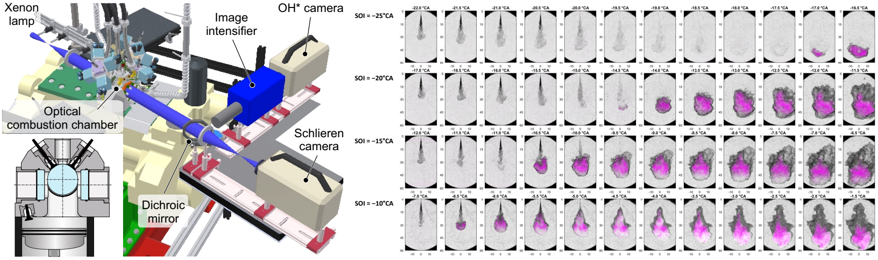

Figure 5.3: Optical setup of simultaneously applied Schlieren and $^{\bullet}$OH chemiluminescence methods (left) [110]; exemplary high-speed Schlieren acquisition of lean premixed CH_4/air pilot ignited DF combustion process (right) [53].

5.2 Available Data and Measurements

An extensive SOI variation is performed to validate the pre-ignition model with test bench measurements. After coordination and evaluation of data from large engines, a pressure of 70 bar and the three temperatures 750 K, 800 K, and 850 K at the end of compression are selected for the tests. The air-fuel ratio is also varied, as shown in table 5.1. For the temperature of the lubricating oil, 453.15 K is chosen. This value is also based on empirical values on large engines. For each of these operating points, the time at which the lubricating oil is introduced is varied. This is performed for almost all operating points between -180 °CA and TDCF in 10 °CA steps each and thus at 18 SOIs. For each SOI, approximately 30 tests are carried out and optically evaluated. After just a few tests, the sapphire window of the test rig becomes dirty and has to be removed and cleaned. It quickly becomes apparent that thousands of measurements had to be carried out and evaluated for this validation data.

Table 5.1: Boundary conditions of the SOI variation for comparing measured data and pre-ignition model.

λ [-]	T_{EOC} [K]	p_{EOC} [bar]	T_{oil} [K]
1	750	70	453.15
1.5	750	70	453.15
2	750	70	453.15
1	800	70	453.15
1.5	800	70	453.15
2	800	70	453.15
2.25	800	70	453.15
2	850	70	453.15

Figure 5.4 shows the temperature curve plotted against the crank angle for the temperatures 750 K, 800 K, and 850 K at the end of compression. However, only the range between -180 °CA and TDCF is usually required as input parameters for the pre-ignition model since pre-ignitions that would occur after TDCF are no longer relevant. This is because the main ignition, e.g., by a diesel pilot, already occurs a few degrees crank angle before the TDCF. The temperatures at the end of compression of 750 K and 800 K are realized by the late closing of the intake valve. This type of operation is also called Atkinson cycle after its inventor James Atkinson [7].

For the blue curve with the lowest temperature of 750 K at the end of compression, the inlet valve is closed later resulting in less compression and thus a lower temperature. The different temperatures of 750 K and 800 K are achieved by changing the effective compression ratio. At a temperature of 850 K at the end of compression, the standard valve timing is used. A higher temperature is set by a combination of charge air temperature and boost pressure.

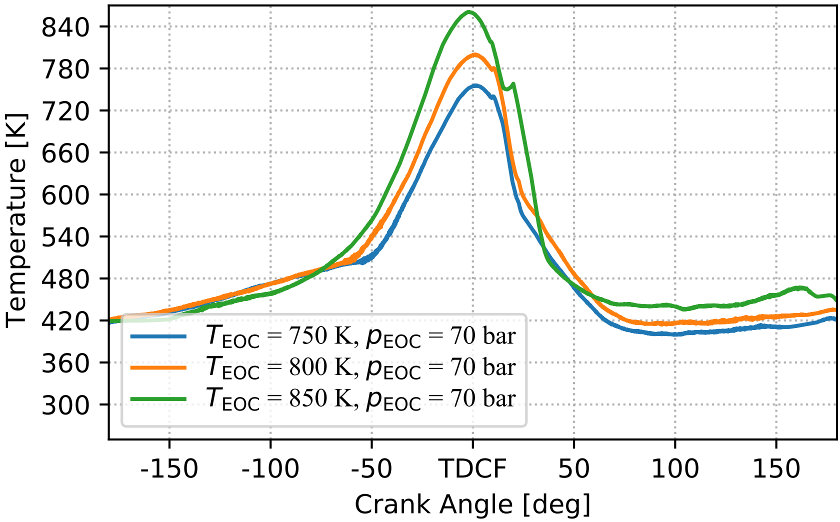

Figure 5.4: Temperature curve of the test rig for 750 K, 800 K and 850 K and a maximum pressure of 70 bar at the end of compression.

In fig. 5.5, the pressure is plotted against the crank angle in the same way as in the previous figure. It can be seen that with the changed temperature at the end of compression, the same pressure is not achieved for all cases. In order to achieve a similar or the same pressure at the end of compression, the boost pressure is increased in the 750 K case compared to the 800 K. The case of 850 K at the end of compression is not directly comparable with the other two cases because the standard valve timing of the test facility is used here and not the Atkinson timing as in the other two cases. The higher temperature of 850 K is realized by a higher inlet temperature and a higher boost pressure. Even if the target for all operating points is 70 bar at the end of compression, some difference is visible. For the evaluation, the final compression pressure is still 70 bar. The deviation is used both for the measurements and as a boundary condition for the simulation. The deviation is therefore taken into account. The pressure curve is also only transferred from -180 °CA to TDCF in the simulation for the normal case, since pre-ignition after TDCF is irrelevant for standard operating points. If there is a use case for pre-ignition after TDCF, this can be set in the model.

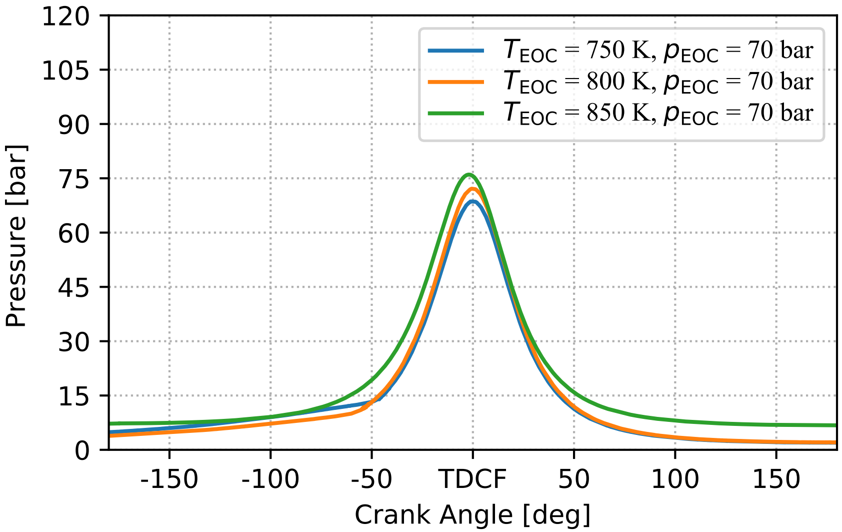

Figure 5.5: Pressure curve of the test rig for 750 K, 800 K and 850 K and a maximum pressure of 70 bar at the end of compression.

The rotational speed for all experiments of this SOI variation is set to 600 rpm. At this point it is important to explain that the speed of the Flex-OeCoS is not comparable to the speed of a normal combustion engine. The test rig cannot be compared to a normal engine in this respect. By selecting the speed, different flow conditions or turbulence levels can be set. For this reason, engine speed variation makes little sense at this point. The influence of the flow has already been described in section 4.1.3 for validation under the influence of forced convection as well as in section 4.1.4. The main effect of the change in rotational speed is more or less time at which ignitable boundary conditions prevail for the lubricating oil. This also explains why lube-oil-induced pre-ignition plays a role above all in the case of slow-running large engines, since the period during which critical boundary conditions are present is longer in the case of these engines.

5.3 Measurement Data Analysis

The measured data of the SOI variation by the Flex-OeCoS test rig is discussed for the measurement data analysis. First, the measurements are explained using two operating points and then all available measurement data of the SOI variation are compared and discussed. Section 5.4 uses the measurement data studied here to validate the pre-ignition model.

Figure 5.6 shows the first operating point. The Measurement (MMT) is performed at the temperature curve of the operating point of 750 K at the end of compression (see section 5.2). The diagram shows the SOI on the y-axis, i.e. the time in °CA at which the lubricating oil is injected into the combustion chamber. The SOIgn, which is determined optically, is plotted on the X-axis. The SD is shown as a dashed line. To exclude strong outliers, the MED is shown as a solid line as a reference for the assessment.

As can be seen from the first diagram, the SOIgn is almost independent of the time at which the oil is injected into the combustion chamber. With each measurement, the same behavior can be observed to a greater or lesser extent, namely that the MED tends slightly towards later SOIgn at earlier SOIs. This behavior is due to the test bench design. As presented in section 5.1, the combustion chamber is accessible via a circular window. Lubricating oil drops have much more time to move before ignition occurs in an earlier SOI. If a drop flies outside the detectable area and ignites outside of it, only the flame front that enters the visible area will be detected as ignition. In this case, the SOIgn is detected later than it actually occurred. This behavior is observed much more often with earlier SOIs than with late SOIs or those in the middle range (-60 °CA < SOI < -120 °CA). The quality of the measurement results is not impaired by this effect, but it must be taken into account when interpreting them.

When interpreting fig. 5.6, it is noticeable that clear peaks in the SD can be seen in some SOIs. Earlier SOIgn occurs in individual measurements, which can be attributed to a locally higher temperature. It can be seen that the SOIgn is relatively constant over the SOI variation. The time at which the lubricating oil is introduced into the combustion chamber thus seems to be less relevant. It can be said that pre-ignition is thus triggered as soon as lubricating oil is available and a specific temperature and pressure are present.

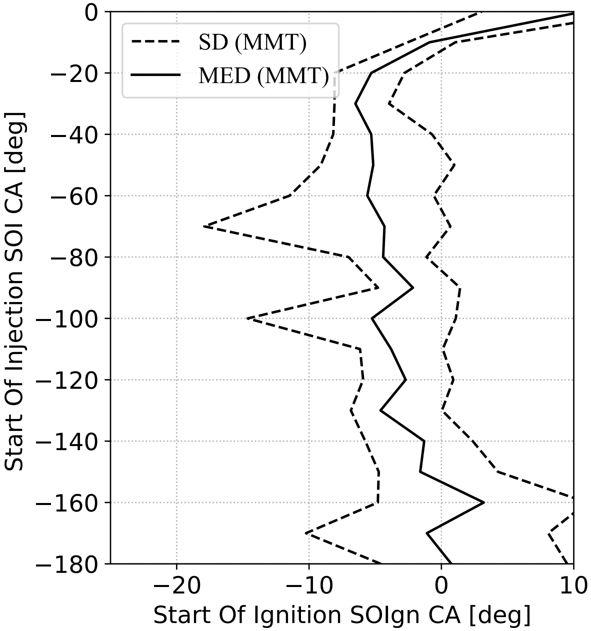

Figure 5.6: SOI variation measurement at a temperature of 750 K and 70 bar at the end of compression and varying AFER $\lambda = 2$.

The second operating point shown in fig. 5.7 differs from the first in the temperature at the end of compression, which is increased by 50 K to 800 K, and in the AFER, which is reduced by 0.5 to $\lambda = 1.5$. Similar to the previous operating point, it can be observed that the SOI also has no significant influence on the SOIgn. There are also two peaks in the SD, but they are not as strong as at the previous operating point. The SD is lower than before, which indicates a very stable SOIgn over the many measurements. At an SOI < -140 °CA, a slight jump in the SD towards a later SOIgn can be seen, which can be explained by the previously mentioned issue of the detectable range. The temperature increase of 50 K at the temperature at the end of compression has the effect of a relatively constant shift of approx. 5 °CA towards early SOIgn.

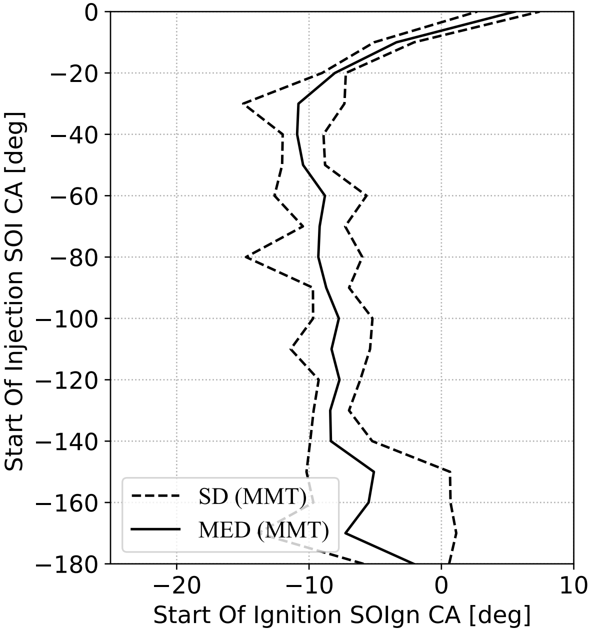

Figure 5.7: SOI variation measurement at a temperature of 800 K and pressure of 70 bar at the end of compression and varying AFER $\lambda = 1.5$.

The median from all measurements of SOI variation with a temperature of 750 K at the end of compression are summarized in fig. 5.8. All results are shown unfiltered and unchanged. For this reason, the error in the AFER of $\lambda = 1$ is also seen at the 0 °CA SOI. The cause of this is unknown, and the measurements at the low SOI < −30° CA are hardly relevant since it cannot be assumed that new oil will enter the combustion chamber at such a late stage. It can be seen that the leaner the mixture, the earlier the SOIgn takes place. Between $\lambda = 1$ and $\lambda = 2$ this effect can be seen more clearly, at $\lambda = 1.5$ the points are almost on the $\lambda = 2$ curve or even equal on average. Since the measurement is only carried out up to an SOI of −70 °CA, it is difficult to make a statement about the further course. In general, it can be said that the influence of the AFER is relatively small. The reproducibility on the test rig is very high, but it cannot be assumed that temperature and AFER can be set precisely at every operating point. There are also local inhomogeneities that can lead to variations in the measurement results. However, since the median is already used here, it can be stated that an excess of oxygen due to a leaner mixture affects an earlier SOIgn.

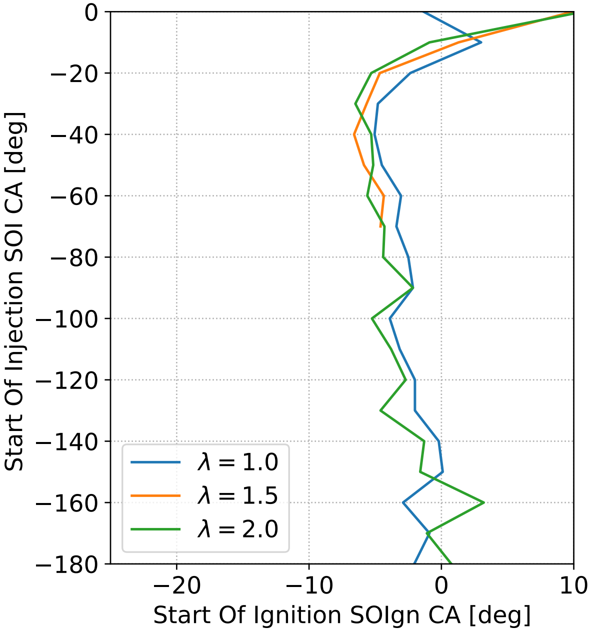

Figure 5.8: MED of the SOI variation measurement at a temperature of 750 K and pressure of 70 bar at the end of compression and varying AFER.

The measured median at 800 K at the end of the compression is shown in fig. 5.9. There is a SOI variation at different AFERs between $\lambda = 1$ and $\lambda = 2.25$. When analyzing the measured data, the $\lambda = 2$ case is immediately noticeable which does not fit the otherwise observed behavior. This operating point should be between $\lambda = 1.5$ and $\lambda = 2.25$ and the small AFER difference should not have such an enormous influence. At the current time, no exact cause could be found on the test bench side. However, it can be assumed that a slight increase in temperature during the tests led to a slight shift. Compared to the curve with 750 K at the end of compression, a shift of approx. 5 °CA in the early direction can be seen. Again, a slight tendency towards late SOIgn is observed for early SOIs, which can be attributed to the optically accessible range.

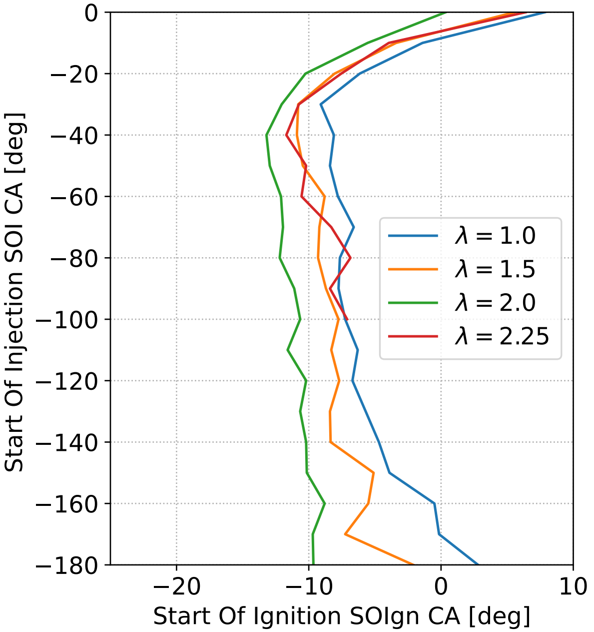

Figure 5.9: MED of the SOI variation measurement at a temperature of 800 K and a pressure of 70 bar at the end of compression and varying AFER.

In order to still have a very hot operating point in the SOI variation, an SOI variation is measured at a temperature of 850 K at the end of compression. The AFER of $\lambda = 2$ is chosen because this operating point is still controllable, as the risk of engine knock is significantly increased at richer operating points. The already discussed issue with the evaluation error at this operating point is similar to the temperature of 800 K at the end of compression and $\lambda = 1$. Some measurement series seem to be more sensitive for earlier SOIs, and some less. Slight differences in the flow conditions can have a visible effect on early SOIs and carry the lubricating oil outside the optically evaluable range. A strong temperature sensitivity of the pre-ignition phenomenon can also be seen at this operating point. The MED of the SOIgn of the 850 K end-of-compression operating point is 3.2 °CA earlier at a reference point of −100 °CA SOI than the same operating point at 800 K end of compression and 8.6 °CA earlier than at 750 K end of compression, supporting the temperature sensitivity.

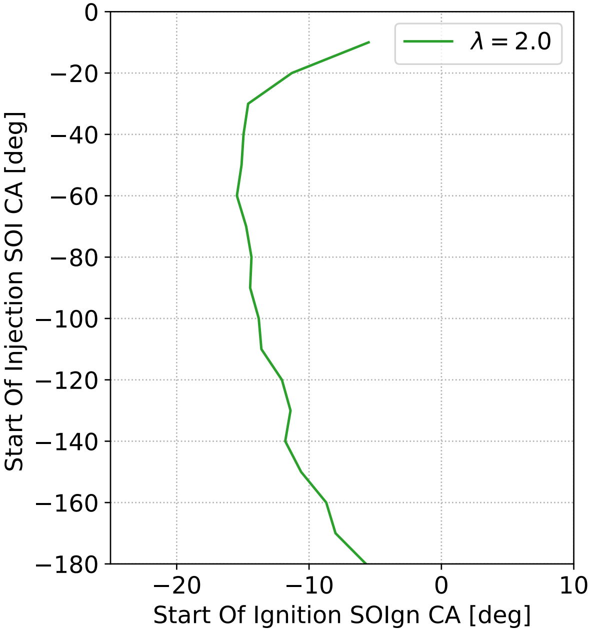

Figure 5.10: MED of the SOI variation measurement at a temperature of 850 K and a pressure of 70 bar at the end of compression and varying AFER.

In summary, several conclusions and results can be extracted from the measurement data analysis. The fact that the faulty operating point at a temperature of 800 K and an AFER of 2 is presumably due to a temperature increase also underlines this observation. The influence of the AFER is almost negligible for both temperature curves. The impact is visible, but is lost in the normal fluctuation of measurements. However, the results are precious for identifying trends and performing model validation. Another elementary finding is that the time at which the lubricating oil drops are introduced into the combustion chamber (SOI) has virtually no influence on pre-ignition. This finding simplifies both the modeling and the applicability to other engines. In order to assess whether pre-ignition can occur, an SOI in the medium range (−60 °CA < SOI < −120 °CA) is usually sufficient as a boundary condition for the model in order to be able to make a statement about the occurrence of pre-ignition. The measurements shown are used in the following section and compared and analyzed with the results from the phenomenological pre-ignition model.

5.4 Temperature Variation Results

This section presents the main part of the validation of the phenomenological pre-ignition model against the measured data. As already shown in section 5.2, 750 K, 800 K, and 850 K are chosen as the temperature at the end of the compression. An SOI variation is performed on the three temperature curves at varying AFER. With the boundary conditions of the optically accessible test facility in the form of a pressure and temperature curve, the time of the pre-ignition onset is calculated with the pre-ignition model. In the following section, each measured operating point is compared with the calculation from the model, analyzed, and discussed.

When interpreting the diagrams, it should be noted that the abbreviation MMT stands for measurement, and Simulation (SIM) represents the data calculated by the pre-ignition model. The SD is shown as a dashed curve, the MED as a solid line, and the calculated time of pre-ignition (IGN) as a star.

5.4.1 750 K at the End of Compression

In this section, all measured operating points with a temperature of 750 K and a pressure of 70 bar at the end of compression are compared with the measured values of SOI variation. The three operating points have an AFER of $\lambda = 1$, $\lambda = 1.5$, and $\lambda = 2$. The $\lambda = 1$ and $\lambda = 2$ cases are performed at an SOI from TDCF (0 °CA) to −180 °CA. In the case of $\lambda = 1.5$, the measurement is performed only up to an SOI of −70 °CA because, at the time of the measurement, it is necessary to limit the number of experiments. In retrospect, earlier SOIs (< −60 °CA) would have provided more insight, since they are in the more relevant range for the real engine. Nevertheless, a comparison with the simulation is possible.

In the first comparison, the operating point of $\lambda = 1$ is shown in fig. 5.11. As already discussed in the measurement data analysis, the SOI at 0 °CA is not realistic. All other SOIs seem plausible. It can be seen that the calculated values agree very well with the measurements. Especially in the relevant range SOI < -60 °CA, because after this point a new lubricating oil input can no longer be assumed, the simulation matches the measurement very well. All calculated points are in the range of the SD. The simulation can accurately predict the occurrence of the later SOIgns at late SOIs. In summary, a good agreement between the results of the pre-ignition model with the measurement can be assumed.

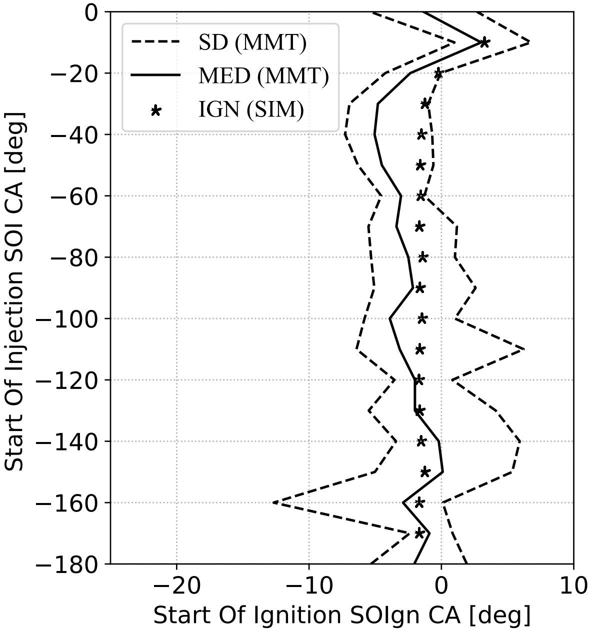

Figure 5.11: Validation of the pre-ignition model against measured data for an SOI variation at a temperature of 750 K at the end of compression and pressure of 70 bar at the end of compression and AFER $\lambda = 1$.

In the second comparison between the pre-ignition model and the measurement for the temperature of 750 K at the end of compression, the case $\lambda = 1.5$ can be seen in fig. 5.12. As mentioned, this measurement is only performed up to an SOI of −70 °CA. The engine-relevant range below −60 °CA can, unfortunately, only be analyzed to a limited extent. It can be seen that the simulation calculates the SOIgn slightly later than the MED from the measurement. Three points calculated with the model are minimally outside the SD. The other calculated points are within the SD. Compared to the calculation at $\lambda = 1$ in the previous one, it can also be seen that the SD turns out to be lower. One reason for this is that fewer measurements are performed per SOI. Nevertheless, an acceptable agreement of measurement and simulation is given.

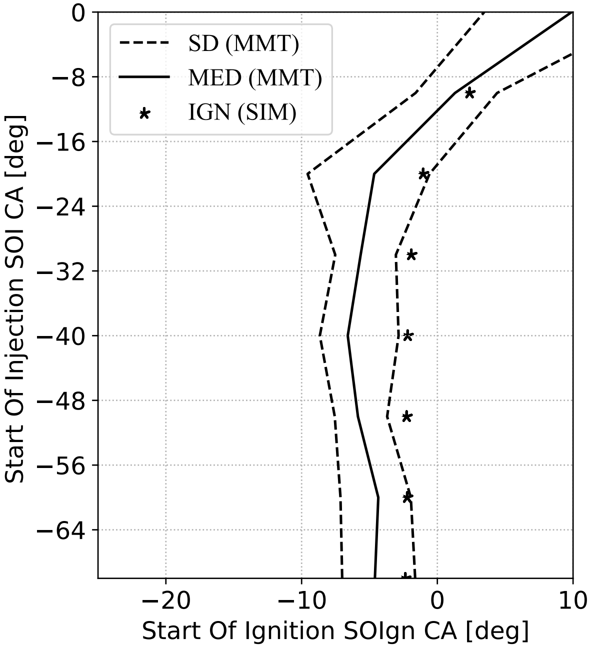

Figure 5.12: Validation of the pre-ignition model against measured data for an SOI variation at a temperature of 750 K at the end of compression and pressure of 70 bar at the end of compression and AFER $\lambda = 1.5$.

The final comparison of the simulation with the measured data at a temperature of 750 K at the end of the compression, can be seen in fig. 5.13. The AFER at this operating point is very lean with $\lambda = 2$. In the measured data, the peaks in the SD are noticeable, which are already discussed in the previous chapter. The MED of the measurement results is very jagged, especially in the low SOI range, and goes towards late SOIgn at very early SOIs. The calculation results from the phenomenoligical pre-ignition model fit very well to the measurements at this operating point, especially in the engine-relevant range. As already mentioned, it is a sign of good modeling if the simulation follows the trend for late SOIs, but these SOIs are less important for real applications. From an SOI of −40 °CA, all calculated pre-ignitions lie within the SD. There is a perfect agreement between the model and measurement.

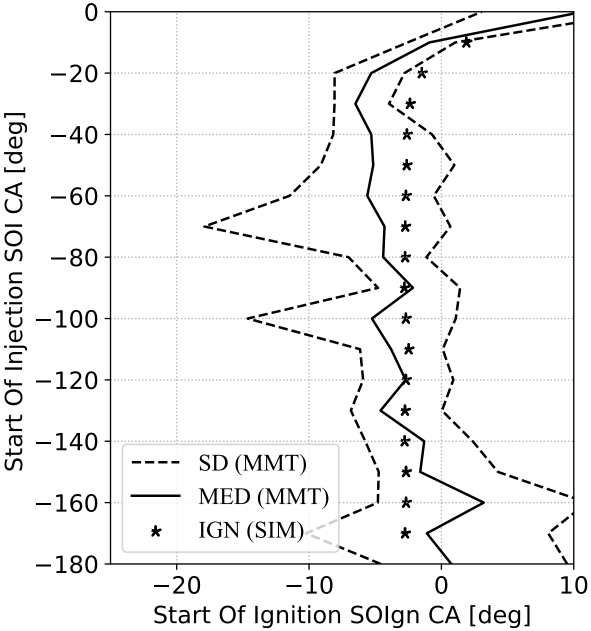

Figure 5.13: Validation of the pre-ignition model against measured data for an SOI variation at a temperature of 750 K at the end of compression and pressure of 70 bar at the end of compression and AFER $\lambda = 2$.

5.4.2 800 K at the End of Compression

In the following section, the measured operating points for 800 K at the end of compression are compared with the results from the phenomenological pre-ignition model. The first operating point at an AFER of $\lambda = 1$ is shown in fig. 5.14. Most clearly, of all the comparisons presented, the shift toward late SOIgn is seen here, starting at an SOI of −120 °CA. This behavior has already been analyzed and explained in detail in section 5.3 and is due to the limited area of the optical evaluation. However, up to the SOI of −120 °CA, there is an almost perfect agreement between the values calculated with the pre-ignition model and the measured values. Especially in the engine-relevant middle SOI range, the agreement is perfect. Despite the shift in very early SOIs, it can be seen that the values lie in the range of the SD.

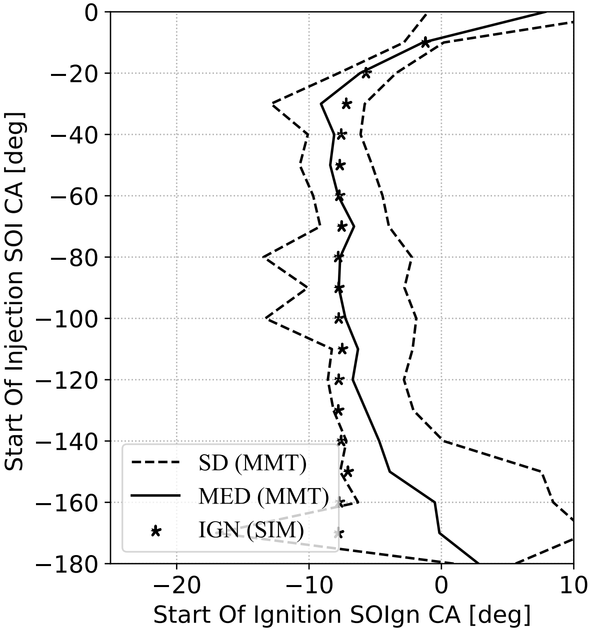

Figure 5.14: Validation of the pre-ignition model against measured data for an SOI variation at a temperature of 800 K at the end of compression and pressure of 70 bar at the end of compression and AFER $\lambda = 1$.

In the subsequent comparison, the operating point is set with an AFER of $\lambda = 1.5$ and shown in fig. 5.15. The shift for very early SOIs, as seen in the comparison before, is much smaller in this case. There is an excellent agreement between the calculated values of the phenomenological pre-ignition model and the measured values at the Flex-OeCoS. All simulated values are within the range of the SD and match the MED within a wide range. Especially in the engine-relevant area, a perfect prediction of the pre-ignition can be seen.

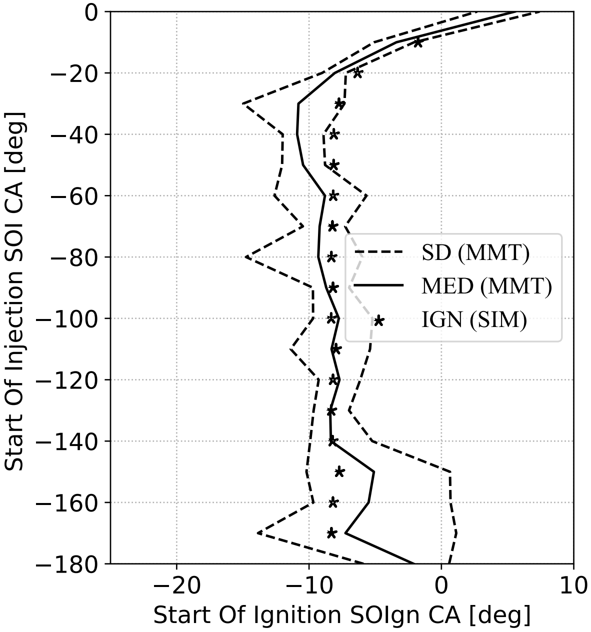

Figure 5.15: Validation of the pre-ignition model against measured data for an SOI variation at a temperature of 800 K at the end of compression and pressure of 70 bar at the end of compression and AFER $\lambda = 1.5$.

In fig. 5.16, the comparison with the incorrect measurement is shown for completeness. As already discussed in the measurement data analysis in section 5.3, the measurement here does not fit the general trend and is implausible. An unintentional temperature increase in this measurement campaign could cause the shift towards early SOIgns. An apparent deviation of the MED from the calculated values, especially for late SOIs, can be seen. From −80 °CA SOI and from −100 °CA SOI, respectively, the calculated values are even again in the range of the SD. For very early SOIs, the calculation and MED are even relatively close to each other, but this is again due to the known evaluation inaccuracy. At this operating point, the extreme temperature sensitivity of the pre-ignition phenomenon can also be observed, which has already been discussed and will be analyzed further. Minor temperature changes in the charge air that are barely noticed or easily overlooked significantly affect the measurement, but the model can represent the effect. A shift of a few °CA in the direction of early SOIgn is possible through a slight temperature change.

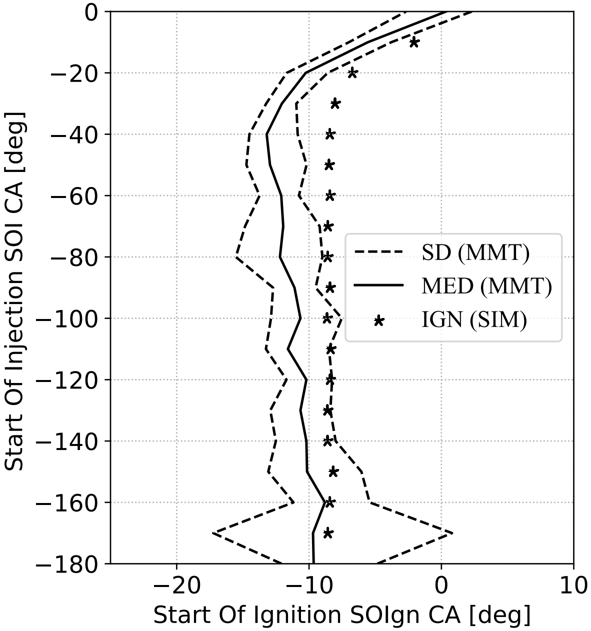

Figure 5.16: Validation of the pre-ignition model against measured data for an SOI variation at a temperature of 800 K at the end of compression and pressure of 70 bar at the end of compression and AFER $\lambda = 2$.

The last comparison is performed down to an SOI of −100 °CA. This very lean operating point with an AFER of $\lambda = 2.25$ can be seen in fig. 5.17. It must be said that this operating point is very relevant for the comparison to real gas DF engines since these are usually operated very lean and on the other hand, it is already hardly possible at this operating point that the mixture combusts completely. Some oil remains deposited on the test facility window and has to be removed and cleaned after each test cycle, which is why fewer SOIs are measured.

As can be seen, the predicted pre-ignitions by the phenomenological pre-ignition model again agree very well with the measurement results. The calculated points are all located on or just next to the MED. All simulated values of the model are within the range of the SD. There is a very good agreement between the model and the test rig.

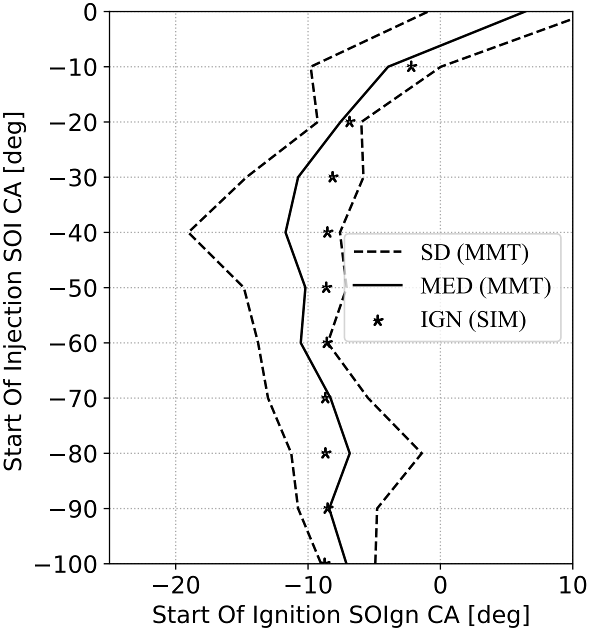

Figure 5.17: Validation of the pre-ignition model against measured data for an SOI variation at a temperature of 800 K at the end of compression and pressure of 70 bar at the end of compression and AFER $\lambda = 2.25$.

5.4.3 850 K at the End of Compression

In order to compare an operating point with a higher temperature at the end of compression, the case with 850 K is measured on the test facility, and a comparison is made with the phenomenological pre-ignition model. An AFER variation could no longer be performed, but an SOI variation is measured at $\lambda = 2$. The high temperatures are also increasingly challenging to measure on the test rig, since strong knocking occurs, especially at richer operating points. For this reason, the test is limited to the one operating point at $\lambda = 2$ in order not to damage the test facility. The result of the comparison can be seen in fig. 5.18. It can be seen from the measurements that for very early SOIs, the median tends towards later SOIgn. On the one hand, this is due to the evaluation problems already explained, and on the other hand, it could be because that the strong temperature influence causes the lubricating oil droplets to evaporate more quickly, resulting in a mixing of the lubricating oil concentration. The more time available for evaporation, the lower the lubricating oil concentration could become locally and thus the ignition delay times longer, which leads to a later SOIgn.

Despite this behavior, the model can predict the measured values very well. Almost in the complete SOI range, the model results are within the standard deviation. Particularly in the engine-relevant range, the model even hits the median. It should also be emphasized that the model correlates well with the measurements, especially in areas with a low standard deviation.

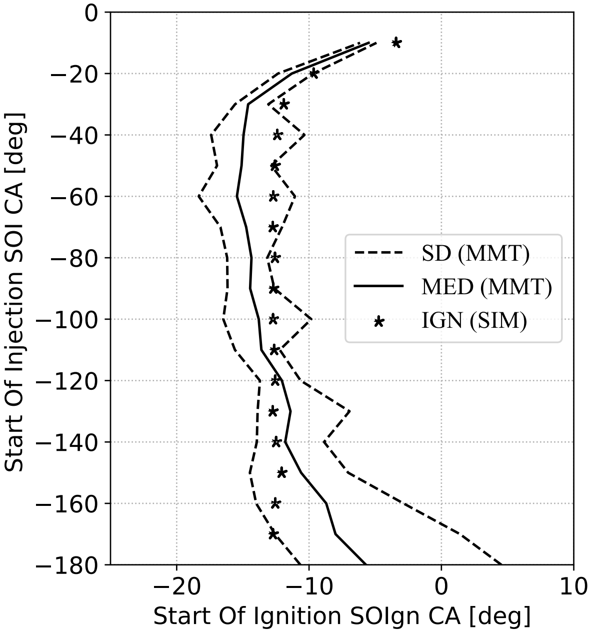

Figure 5.18: Validation of the pre-ignition model against measured data for an SOI variation at a temperature of 850 K at the end of compression and pressure of 70 bar at the end of compression and AFER $\lambda = 2$.

5.5 Discussion and Conclusion of the Validation

The setup of the test facility Flex-OeCoS used for these measurements is shown and briefly explained to better analyze and classify the subsequent results. All measurements to validate the model are performed at the ITFE of the University of Applied Sciences FHNW. The SOI variations carried out to validate the model are studied in the measurement data analysis. The key finding of this investigation is that the pre-ignition phenomenon reacts very sensitively to the influence of temperature. Another finding is that the time at which the lubricating oil is introduced into the combustion chamber is hardly decisive.

The AFER of the premixed air-methane mixture also has little influence on pre-ignition onset.

The issue in the evaluation is explained why early SOIs tend to later SOIgns. The reason for this is an onset of flame propagation outside the optically accessible area at the test facility. Apart from this effect, the SOI has no influence on the SOIgn over wide areas but remains almost constant.

Excellent agreement is shown when comparing the extensive SOI variation, measured by the Flex-OeCoS test facility, with the phenomenological pre-ignition model. The modeling exceeds the expectation made on this modeling approach. It is expected that the model would be able to reproduce a trend but not fit the measurements well at different conditions. In this type of modeling, tuning parameters are usually used to fit the simulation results with the measurement results so that further operating points can be predicted well. However, in the phenomenological pre-ignition model, purely physical assumptions are made. The reaction kinetic and the physics-based calculation does not need any tuning parameters. As a result, the model works very well with the measurements performed. Whether the prediction fits as well with other data can be further investigated. The modeling also benefits from the fact that in the range of slow-running gas engines, significantly fewer operating points are relevant for real operation. Nevertheless, the approach shown here is promising and has been validated using test bench measurements.

6 Validation and Investigations of the Pre-Ignition Modell at Full Engine

6.1 Piston Underside Temperature Variation

In this section, the phenomenological pre-ignition model is compared to a critical operating point of a real marine Gas DF engine from WinGD. The specifications of this engine are listed in table 6.1. For confidentiality reasons, a comprehensive comparison cannot be shown. However, the approved data presented here illustrates how the pre-ignition model can be used in a real engine.

Table 6.1: Specification of the WinGD Test Engine [99].

Parameter	Unit	Value
Bore	[mm]	500
Stroke	[mm]	2050
Rated Power	[kW]	6900
Rated Speed	[rpm]	99
Rated BMEP	[bar]	17.3
Number of Cylinders	[-]	6
Gaseous Fuel	[-]	NG
Liquid Fuel	[-]	MGO

The piston underside temperature (T_{PUS}) is varied in this comparison. This temperature is comparable to the charge air temperature in a four-stroke engine.

On a marine engine, this temperature varies with the ambient temperature. In the engine studied in this thesis, pre-ignition occurs in tropical conditions. For this reason, a standard operating point at which no pre-ignition occurs is compared with the case for tropical conditions. The temperature difference of the piston underside temperature (T_{PUS}) between the two operating points is 5.4 K. The two different pressure and temperature curves measured on the engine are used as boundary conditions for the calculation with the phenomenological pre-ignition model.

Figure 6.1 shows the measured heat release versus crank angle at the marine engine of the two operating points analyzed. In this diagram, numerical values for the heat release have been omitted for reasons of confidentiality; these are not significant for interpreting the observed effect anyway. The heat release curve at tropical conditions is shown in green and the standard operating point in black. The red peak schematically shows the current flow of the ignition pilot of the engine. The height of the peak does not indicate anything. It is only intended to mark the time of the pilot injection. The standard curve shows the normal operation of this marine gas DF engine. Heat release begins immediately after the end of pilot energization, so this behavior is typical of this engine. At the tropical operating point, a significant pre-ignition can be seen. The heat release starts at approx. -7 °CA, although the pilot has not yet ignited the mixture.

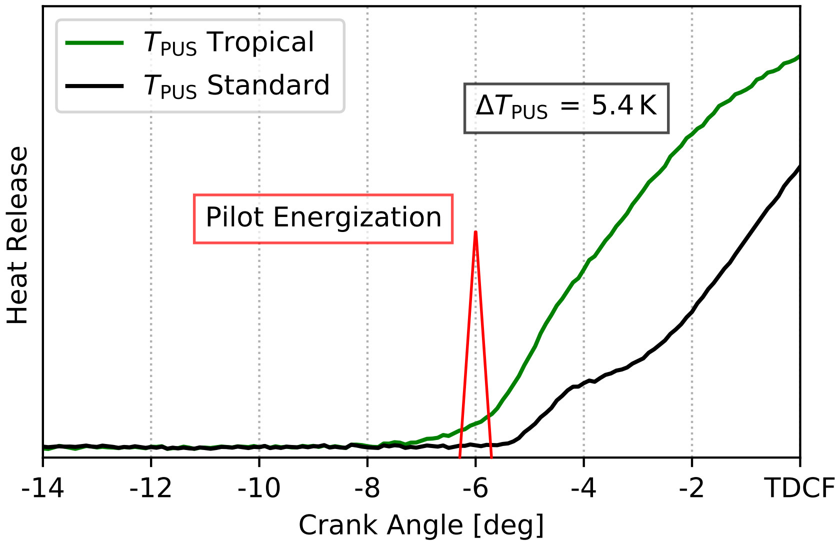

Figure 6.1: Measured heat release in a piston underside temperature comparison between tropical and standard conditions of a two-stroke gas DF engine from WinGD.

As a boundary condition for the phenomenological pre-ignition model, the measured pressure and temperature curves of the operating points ”tropical” and ”standard” and a motor speed of 99 rpm are transferred to the model. As already shown in the previous chapters, the time at which the oil enters the combustion chamber has no significant influence on the start of pre-ignition. In order to calculate the pre-ignition time and to compare it with the measurement, an SOI variation is simulated for both operating points, which is illustrated in fig. 6.2. The SOI variation is shown in the following figure. It can be seen that despite the small temperature difference in the piston underside temperature of 5.4 K, the pre-ignition model predicts a difference of about 2 °CA SOIgn. This quite significant difference in the result shows the high-temperature sensitivity of the pre-ignition phenomenon and how well the model can represent this influence.

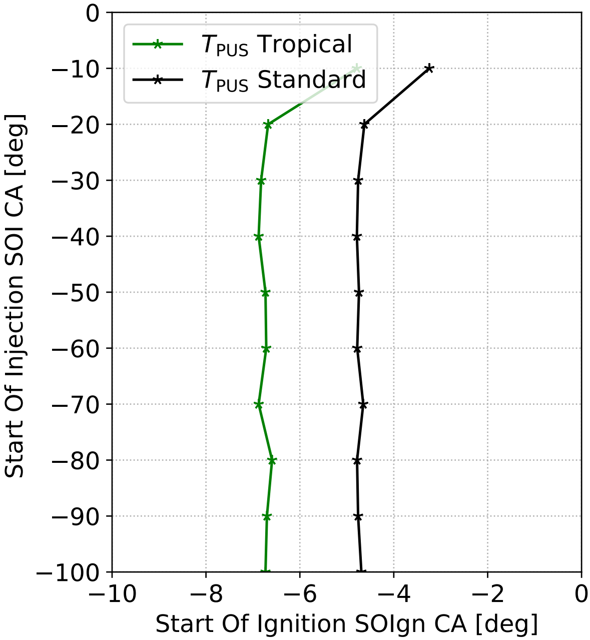

Figure 6.2: Result of the phenomenological pre-ignition model for the engine operating conditions ”tropical” and ”standard” at a difference in piston underside temperature of $\Delta T_{\mathrm{PUS}} = 5.4\,\mathrm{K}$.

In the comparison between the measurement of the real engine (fig. 6.3 left) and a section of the calculated SOI variation computed with the phenomenological pre-ignition model (fig. 6.3 right), the good agreement and predictive ability of the model can be seen. For the standard case, the model predicts pre-ignition at just below −5 °CA. Comparing this value with the measured heat release for the standard case, it can be seen that heat release has already been initiated by the pilot. As already mentioned, the start of heat release at the end of pilot energization is characteristic. The pre-ignition is lost in this main heat release. In this case, it can be assumed that the pre-ignition is not relevant.

For the tropical case with a 5.4 K higher piston underside temperature, a different behavior is seen. Here, a typical pre-ignition phenomenon can be seen in the measured heat release, which already starts before the pilot can ignite the air-fuel mixture in the combustion chamber. The start of the heat release takes place at approx. −7 °CA. The comparison with the model prediction shows that the model calculates the beginning of the pre-ignition quite accurately. This prediction accuracy is obtained using only physical assumptions without the use of tuning parameters. The model thus appears to be able to make good predictions on the real engine, just as it does on the optically accessible ”Flex-OeCoS” test engine.

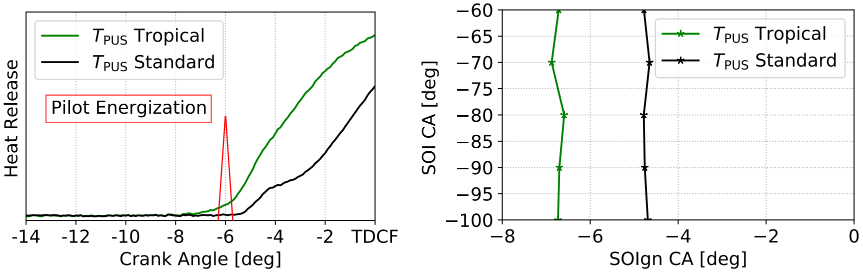

Figure 6.3: Comparison between the measurement on an engine of WinGD and the calculation by the phenomenological pre-ignition model.

In order to answer the question of when pre-ignition occurs, fig. 6.4 shows the heat releases of one hundred cycles under tropical conditions. It can be seen that virtually all cycles have a measurable pre-ignition between -6 °CA and -7 °CA. No cycle begins heat release until after pilot energization. A few start at maximum at the same time. Thus, the pilot is not the cause of heat release.

This diagram can also be used to answer another question, which has already been answered on the test bench, and that is how often pre-ignition occurs. In the case of classic engine knocking, the term ” knock probability” is often used, since knocking usually does not occur in every cycle but only sporadically. In contrast, pre-ignition occurs in every cycle if boundary conditions such as temperature and lubricating oil are present. Calculations of occurrence probabilities and cycle-to-cycle variations are, therefore, obsolete. This finding is obtained by analyzing the measurements on the test rig as well as observations on the real engine.

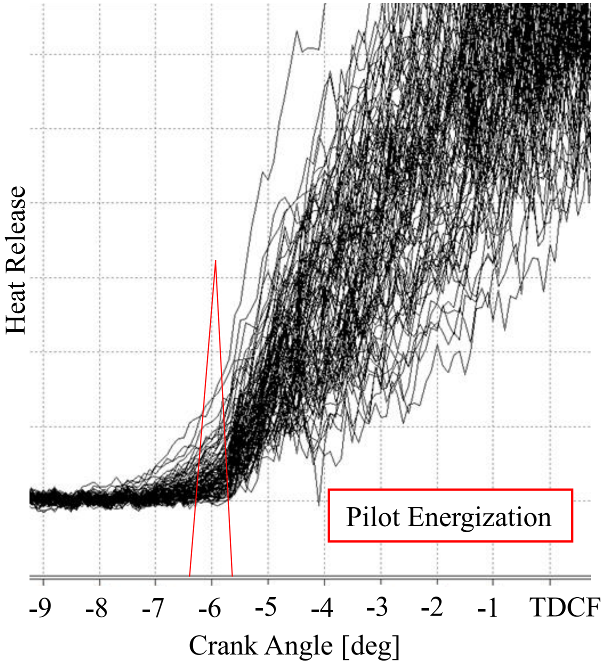

Figure 6.4: Heat release during one hundred cycles of the WinGD marine engine with visible pre-ignition between −6 °CA and −7 °CA.

6.2 Investigation of the Mixture Inhomogeneities

The inhomogeneities in the cylinder of the studied WinGD gas engine are investigated here. Figure 6.5 shows the result of a CFD simulation 10 °CA before the TDCF. Concrete numerical values are not given for reasons of confidentiality, but are not necessary for the analysis of the effect. The left figure shows the AFER distribution. Orange and red areas indicate a rich mixture, blue areas are very lean. The right image shows the residual gas content distribution, which cannot be completely eliminated due to the two-stroke process. The areas with high residual gas concentration contain hot burnt gas from the previous cycle which is blended with a fresh gas-air mixture. Orange and yellow areas represent a high residual gas content, while blue areas contain no residual gas.

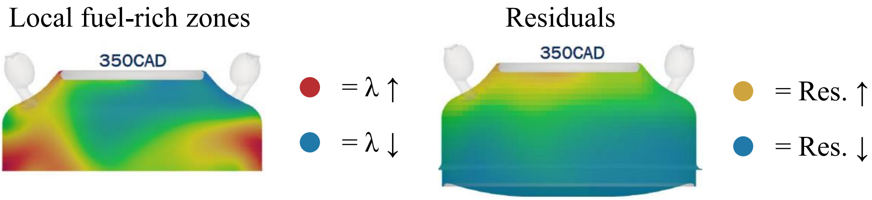
Local fuel-rich zones

Residuals

Figure 6.5: CFD at 350 °CA (TDCF is at 360 °CA) of a WinGD marine gas engine with local fuel-rich zones (left) and residual gas (right).

It can be observed that richer areas appear primarily in the peripheral areas and partly under the exhaust valve. A high residual gas content occurs above all on the combustion chamber roof below the exhaust valve. The boundary conditions can be roughly divided into four states. Lean mixture with a high and low residual gas content and rich mixture with a high and low residual gas content. For this reason, three compression and temperature curves are derived from one measured curve. The temperatures at the end of compression are 730 K, 745 K, and 800 K. It is important to note that these are not real measured curves. Therefore, the results do not allow any conclusions to be drawn about the pre-ignition start of a real engine. However, an interpretation of the temperature influence and the influence of residual gas and AFER can be shown very well with this investigation. The temperature variation aimed to estimate the influence of increased residual gas temperature.

Figure 6.6 shows an SOI variation in the same way as in the previous chapters. The temperature at the end of the compression is varied as described above and calculated for a relatively rich and a very lean mixture. The result shows the same behavior as analyzed in section 5.4. The influence of the AFER is almost negligible. The SOIgn starts slightly later with fatter mixtures than with leaner ones. The significant temperature influence is again clearly visible. Even if, as already mentioned, no real conclusions can be drawn about the time of pre-ignition in the real large engine since, as mentioned, no measured pressure and temperatures are used.

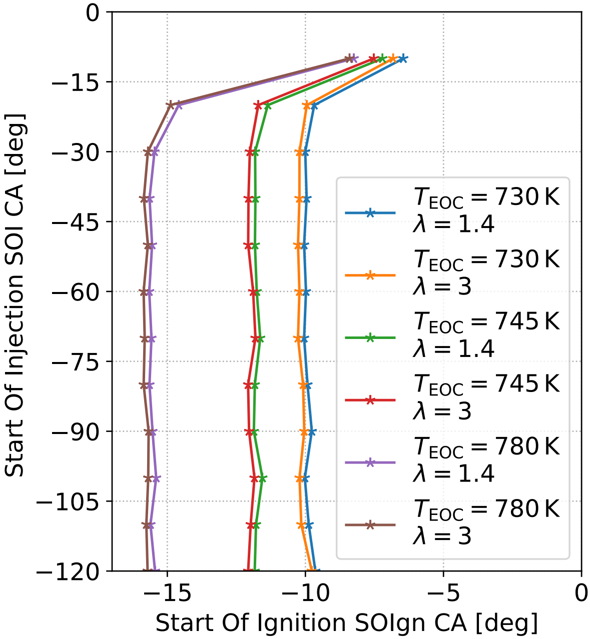

Figure 6.6: Result of the pre-ignition model with a variation of the temperature at the end of compression and the air-fuel ratio.

Both measurements at the Flex-OeCoS test facility and calculations with the pre-ignition model show that AFER has negligible influence on pre-ignition. The effect of residual gas on pre-ignition must be investigated in more detail. Three factors must be taken into account for a possible pre-ignition with residual gas influence:

- The temperature increase due to high residual gas content.
- Are there lubricating oil droplets in the area of the high residual gas content?
- How does the changed gas composition (EGR) affect pre-ignition?

To answer the first statement, the temperature variation has already been calculated. As expected, a clear temperature influence can be seen. At this point, however, how the strongly changed gas composition in combination with the higher temperature in the residual gas affects the pre-ignition remains open. So far, no EGR influence has been implemented in the phenomenological pre-ignition model. Also, no measurements with EGR are performed at the test facility for this thesis. Thus, the residual gas influence on temperature cannot be answered conclusively. Since the pre-ignition phenomenon is very temperature-sensitive, as already discussed, an earlier start of pre-ignition in this area is conceivable if corresponding oil quantities are also present.

This also leads to the next question of whether lubricating oil drops are found in high residual gas quantities. This question cannot be answered with certainty since this would require CFD simulations, which are not the focus of this thesis. However, an estimation can be made. As mentioned before, oil droplets are already present in the receiver and therefore already present in the air inlet. Since the oil droplets are moved along with the fresh mixture, the oil droplet fraction is expected to be higher in the fresh mixture than in the residual gas fraction. Whether oil that is brought into the combustion chamber by the lubrication system through lubricating oil jets (see [60]) is also brought into areas with high residual gas cannot be said with certainty. For this reason, and also to clarify the last question of how strongly EGR influences pre-ignition, a further calculation is carried out. For this purpose, laminar burning velocities are calculated as described in section 3.3.

In fig. 6.7, the laminar burning velocity is plotted against the air-fuel ratio λ. The boundary conditions correspond approximately to the boundary at full load and 10 °CA before TDCF. Both temperature ranges are at 70 bar, the 730 K corresponds to the temperature in the fresh gas, and the 780 K is an expected temperature in the range with residual gas content. The EGR content in the residual gas corresponds to approximately 10 % classical EGR, which at $\lambda = 1$ also corresponds to 10 % stoichiometric EGR. Therefore, 10 % stoichiometric EGR and no EGR are calculated for both temperature ranges. The EGR definition has already been explained in section 3.1.5.

It can be seen that both the temperature difference and the residual gas content have a clear effect on the laminar burning velocity. Temperature rise and EGR have opposite effects. While a higher temperature raises the burning velocity, a higher EGR content lowers it. When considering the mixture at $\lambda = 2$, it can be seen that there is hardly any difference between the case with higher temperature and residual gas or normal temperature without residual gas. The calculated value of the laminar burning velocity is 5.3 cm/s for the first mentioned and 6.1 cm/s for the normal conditions. At this point, it must be said that a classical flame front combustion is hardly imaginable for both cases due to the slow burning velocities. Unfug and Weisser [99] state for the same engine that a flame front combustion is no longer plausible at $\lambda > 1.9$.

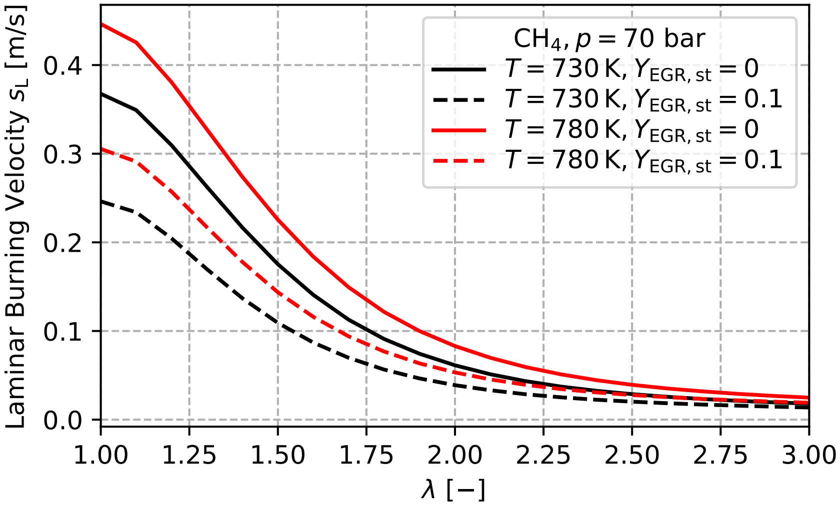

Figure 6.7: Laminar burning velocities of methane with residual gas influence (EGR) at an air-fuel ratio variation at a temperature of 730 K and 780 K and a pressure of 70 bar.

In order to analyze the influence of external EGR on flame propagation, another calculation is performed with cooled EGR, which cools the temperature in the same considered point by 20 K as before. Figure 6.8 shows a variation of the stoichiometric EGR. For reference, the standard point at 730 K is also plotted in the diagram. It can be seen that the temperature difference of 20 K has a negligible effect which almost disappears in the lean region. However, the EGR fraction significantly influences the laminar burning velocity.

Using external EGR could significantly reduce the risk of pre-ignition. The transfer to the real engine is nevertheless tricky since the compression ratio of the EGR engine has been significantly increased, which leads to higher compression temperatures. Furthermore, only chemical effects are considered in the laminar burning velocities. However, the change in calorics also influences self-ignition behavior.

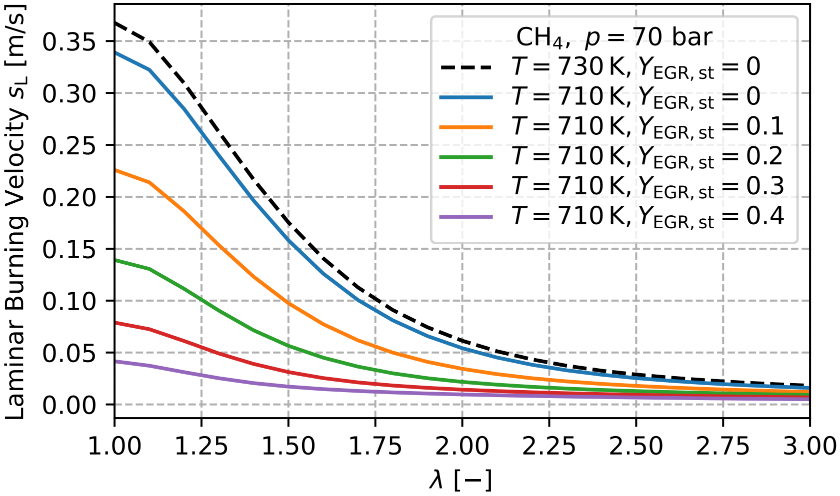

Figure 6.8: Laminar burning velocities of methane at an cooled EGR and AFER variation at a temperature of 710 K and a pressure of 70 bar and a reference point at 730 K as standard condition.

So there remain some open questions that cannot be answered so quickly. How pre-ignition leads to ignition of the mixture must be investigated in more detail. Also, a kind of Homogeneous Charge Compression Ignition (HCCI) combustion can be observed rather than a classical flame front combustion, which is why the burning velocity calculations shown here only serve as a rough analysis. The actual combustion seems much more complex and can not be discussed in detail in this context.

6.3 Discussion

The applicability of the phenomenological pre-ignition model to the full engine is shown in this chapter. The critical application case in tropical conditions where pre-ignition occurs in every cycle is compared against a standard case. The temperature difference of the piston underside temperature is only 5.4 K. Due to the strong temperature dependence of the pre-ignition phenomenon, this small temperature delta is already sufficient to shift the pre-ignition significantly before the pilot energization. With the measured boundary conditions, such as the pressure and temperature curve, fuel composition, lubricating oil temperature, and engine speed, the pre-ignition model is able to predict the pre-ignition time very well. The pre-ignition model is also in the initial test phase for other WinGD engines and shows good agreement. Subsequent work and publications will validate the model against these engines.

Furthermore, an investigation is carried out on how mixture inhomogeneities could affect the pre-ignition. As a basis for this, a CFD simulation is evaluated at an operating point shortly before TDCF and possible boundary conditions are worked out. This analysis also shows the large influence of temperature. Since the higher temperature in the residual gas is also accompanied by a change in the gas composition, laminar burning velocities with EGR influence are calculated.

The comparison with the calculated laminar burning velocities shows that the latter is slightly lower in the area with residual gas than in the fresh gas. However, this should hardly make a difference in the real engine, but in a borderline case it could be decisive whether a flame propagates or not. In general, it is doubtful whether a classic flame front can be assumed since the latest investigations by Unfug and Weisser [99] instead assume an HCCI combustion.

Also, the distribution of the oil droplets is not known or is difficult to predict. Since oil is already present in the receiver, a distribution of the oil as in the figure of the residual gas fraction can be assumed, since the oil droplets are moved along with the flow. Thus, there could be fewer oil droplets in the residual gas. In addition, the oil introduced by the lubrication system could behave differently. In summary, only those findings can be evaluated by the simulation that predict earlier pre-ignition in the residual gas when only the temperature influence is considered.

When examining the external EGR, it becomes apparent that this can massively reduce the laminar burning velocity. Transferability to the real engine is challenging, since factors such as an increase in the compression ratio and calorific effects must be taken into account and, as discussed above, a classic flame-front combustion cannot be assumed.

In this analysis, the behavior of flame propagation after pre-ignition remains an open question. The consideration of the EGR influence has not yet been discussed in the modeling and also on the test rig, or only briefly in the reaction kinetics. However, these two points are not the focus of the thesis, which concentrates on the occurrence of pre-ignition.

7 Conclusion and Outlook

In order to meet the ambitious CO_2 targets, the marine sector is increasingly turning to gas DF engines since natural gas has a better ratio between carbon and hydrogen atoms than diesel, heavy oil, and many other hydrocarbons. With this engine technology, pre-ignition is a problem that limits operation and, in the worst case, can lead to engine damage. The focus of studies and development has been mainly on pre-ignition in the passenger car sector. However, there are only a few studies in the heavy-duty and marine sector. This thesis contributes to a better understanding of pre-ignition in large engines, and a phenomenological pre-ignition model is developed and validated against measurements.

Pre-ignition in low-speed gas engines is induced by lubricating oil droplets. This fundamental statement results from extensive reaction kinetic investigations in the form of ignition delay calculations under various boundary conditions. In the measurements on the optically accessible Flex-OeCoS test facility, no pre-ignition is observed without the influence of lubricating oil. The measurements for this thesis are carried out by the FHNW.

In order to be able to predict the lubricating oil-induced pre-ignition, the phenomenological pre-ignition model is developed, which consists of two main components. The first component is a droplet evaporation model based on the ASM. This model provides boundary conditions for the second component, the reaction kinetics. Finally, with the help of detailed chemistry and the previously calculated gas compositions, pressure, and temperature, the ignition, respectively, the beginning of the pre-ignition, is determined.

To validate the entire model, an extensive SOI variation is performed in which drops of lubricating oil are introduced into the optically accessible combustion chamber at different times, temperatures, pressures, and AFERs. The calculated values of the phenomenological pre-ignition model fit very well with the measured values, and it could be shown that the model has good prediction accuracy. The model also shows good predictive capability when compared with a real marine gas DF engine. For validation, measurement results of a piston underside temperature variation at tropical and normal conditions are available. The phenomenological pre-ignition model is able to predict the onset of pre-ignition at tropical conditions at which pre-ignition occurs in every cycle in 100 measured cycles. The presented methodology can also be used to investigate the pre-ignition phenomenon in the real engine in more detail, which is also shown in the example of the WinGD DF gas engine.

Further analysis of flame propagation after a previous pre-ignition would be interesting for future investigations, which are already partially discussed in this thesis by calculating laminar burning velocities. The very lean mixtures ($\lambda > 2$) which are common in large gas engines, suggest that the combustion process can no longer be assumed to be a classical flame front combustion. The effect of lube-oil-induced pre-ignition on the main combustion can also be a gain in knowledge for the development of these engines.

The changeover to natural gas is already a key factor in reducing CO_2 emissions. However, CO_2 emissions could be further reduced with CO_2-reduced fuels such as ammonia or the addition of hydrogen, which is increasingly the focus of current research. Investigating pre-ignition phenomena and flame propagation with these fuels would make another important contribution to the development of large engines.

Bibliography

[1] B. Abramzon and W. Sirignano. *Droplet vaporization model for spray combustion calculations*. 1988. DOI: `10.2514/6.1988-636`.

[2] D. Ambrose and C. Tsonopoulos. "Vapor-Liquid Critical Properties of Elements and Compounds. 2. Normal Alkenes". In: *J. Chem. Eng. Data* 40 (1995), pp. 531–546.

[3] Ch. Antoine. "Tensions des vapeurs: nouvelle relation entre les tensions et les températures". In: *Comptes Rendus des Séances de l'Académie des Sciences* 107 (1888), pp. 681–684, 778–780, 836–837.

[4] Luis Arnaut. *Chemical Kinetics*. Elsevier, 2021. ISBN: 978-0-444-64039-0. DOI: `10.1016/c2016-0-04391-7`.

[5] Svante Arrhenius. "Über die Dissociationswärme und den Einfluss der Temperatur auf den Dissociationsgrad der Elektrolyte". In: *Zeitschrift für Physikalische Chemie* 4U.1 (July 1889), pp. 96–116. DOI: `10.1515/zpch-1889-0408`.

[6] Svante Arrhenius. "Über die Reaktionsgeschwindigkeit bei der Inversion von Rohrzucker durch Säuren". In: 4 (1889). ISSN: 2196-7156. DOI: `10.1515/zpch-1889-0116`.

[7] James Atkinson. "Gas-Engine". US367496A. Aug. 1887.

[8] Ghobad Bagheri et al. "Comprehensive kinetic study of combustion technologies for low environmental impact: MILD and OXY-fuel combustion of methane". In: 212 (2020), pp. 142–155. ISSN: 0010-2180. DOI: `10.1016/j.combustflame.2019.10.014`.

[9] Saptarshi Basu et al., eds. *Droplets and Sprays*. Springer Singapore, 2018. DOI: `10.1007/978-981-10-7449-3`.

[10] Robert Byron Bird, Warren E. Stewart and Edwin N. Lightfoot. *Transport phenomena*. Rev. 2. ed. New York [u.a.]: Wiley, 2007. XII, 905. ISBN: 9780470115398.

[11] C. W. Bowman et al. “Mass transfer from fluid and solid spheres at low reynolds numbers”. In: 39 (1961), pp. 9–13. ISSN: 0008-4034. DOI: `10.1002/cjce.5450390104`.

[12] P. L. T. Brian and H. B. Hales. “Effects of transpiration and changing diameter on heat and mass transfer to spheres”. In: 15 (1969), pp. 419–425. ISSN: 0001-1541. DOI: `10.1002/aic.690150323`.

[13] J. G. Calvert. “Glossary of atmospheric chemistry terms (Recommendations 1990)”. In: *Pure & Appl. Chem.* 62.11 (Jan. 1990), pp. 2167–2219. DOI: `10.1351/pac199062112167`.

[14] David L. Camin, Alphonse F. Forziati and Frederick D. Rossini. “Physical Properties of n-Hexadecane, n-Decylcyclopentane, n-Decylcyclohexane, 1-Hexadecene and n-Decylbenzene”. In: 58 (1954), pp. 440–442. ISSN: 0022-3654. DOI: `10.1021/j150515a015`.

[15] G. S. Canada and G. M. Faeth. “Fuel droplet burning rates at high pressures”. In: 14 (1973), pp. 1345–1354. ISSN: 0082-0784. DOI: `10.1016/s0082-0784(73)80120-1`.

[16] Christian Chauveau et al. “An experimental study on the droplet vaporization: effects of heat conduction through the support fiber. IT 2008”. In: (Jan. 2008).

[17] Roland Clift. *Bubbles, drops, and particles. R. Clift, J. R. Grace, and M. E. Weber*. Ed. by J. R. Grace and M. E. Weber. Includes bibliographies and index. New York: Academic Press, 1978. xiii, 380 p. : ill. ; 24 cm. ISBN: 012176950X.

[18] A. Kayode Coker. *Modeling of Chemical Kinetics and Reactor Design*. Elsevier Science and Techn., Aug. 2001. 1136 pp. ISBN: 9780080491905.

[19] Sebastian K. Crönert. *A Complete Methodology for the Predictive Simulation of Novel, Single- and Multi-Component Fuel Combustion*. 1st ed. 2567-0352. Springer Vieweg Wiesbaden, 2023. ISBN: 978-3-658-43075-7. DOI: `https://doi.org/10.1007/978-3-658-43075-7`.

[20] Cyril Crua, Julien Manin and Lyle M. Pickett. “On the transcritical mixing of fuels at diesel engine conditions”. In: *Fuel* 208 (Nov. 2017), pp. 535–548. DOI: `10.1016/j.fuel.2017.06.091`.

[21] A. Cuoci et al. “Formation of soot and nitrogen oxides in unsteady counterflow diffusion flames”. In: 156 (2009), pp. 2010–2022. ISSN: 0010-2180. DOI: `10.1016/j.combustflame.2009.06.023`.

[22] E. W. Curtis and P. V. Farrell. “A numerical study of high-pressure droplet vaporization”. In: *Combustion and Flame* 90.2 (Aug. 1992), pp. 85–102. URL: `https://ui.adsabs.harvard.edu/abs/1992CoFl...90...85C`.

[23] E. W. Curtis and P. V. Farrell. “Droplet vaporization in a supercritical microgravity environment”. In: *Acta Astronautica* 17.11 (Jan. 1988), pp. 1189–1193. DOI: `10.1016/0094-5765(88)90007-0`. URL: `https://ui.adsabs.harvard.edu/abs/1988AcAau..17.1189C`.

[24] Christoph Dahnz, Kyung-Man Han and Max Magar. *Vorentflammung bei Ottomotoren. Vorhaben Nr. 931, Untersuchung des Auftretens und der Ursache von Selbstzündungen vor Zündungseinleitung bei aufgeladenen Motoren mit hohem Verdichtungsverhältnis ; Abschlussbericht*. Frankfurt/M: FVV, Forschungsvereinigung Verbrennungskraftmaschinen e.V., 2010.

[25] A. Daïf et al. “Comparison of multicomponent fuel droplet vaporization experiments in forced convection with the Sirignano model”. In: 18 (1998), pp. 282–290. ISSN: 0894-1777. DOI: `10.1016/s0894-1777(98)10035-3`.

[26] D. F. Davidson et al. “Ignition delay time measurements and modeling for gasoline at very high pressures”. In: 37 (2019), pp. 4885–4892. ISSN: 1540-7489. DOI: `10.1016/j.proci.2018.08.032`.

[27] Jörg Dedl et al. “Using Fuel Figures to Evaluate Pre-ignition in Gasoline Engines”. In: 79 (2018), pp. 68–73. ISSN: 2192-9114. DOI: `10.1007/s38313-018-0028-2`.

[28] E. Distaso et al. “Investigation of Lubricant Oil influence on Ignition of Gasoline-like Fuels by a Detailed Reaction Mechanism”. In: 148 (2018), pp. 663–670. ISSN: 1876-6102. DOI: `10.1016/j.egypro.2018.08.155`.

[29] G. Dixon-Lewis. “Flame structure and flame reaction kinetics II. Transport phenomena in multicomponent systems”. In: *Proceedings of the Royal Society of London. Series A. Mathematical and Physical Sciences* 307.1488 (Oct. 1968), pp. 111–135. DOI: `10.1098/rspa.1968.0178`.

[30] J. K. Dukowicz. “Quasi-steady droplet phase change in the presence of convection”. In: (1979). DOI: `10.2172/6012968`.

[31] Matthias Eble and Markus Müller. URL: `https://www.gecko-instruments.de/pages/produkte/precisive/erdgas-zusammensetzung.php` (visited on 13/06/2022).

[32] G. M. Faeth. "Current status of droplet and liquid combustion". In: 3 (1977), pp. 191–224. ISSN: 0360-1285. DOI: `10.1016/0360-1285(77)90012-0`.

[33] T. Faravelli, A.Frassoldati and E. Ranzi. "Kinetic modeling of the interactions between NO and hydrocarbons in the oxidation of hydrocarbons at low temperatures". In: 132 (2003), pp. 188–207. ISSN: 0010-2180. DOI: `10.1016/s0010-2180(02)00437-6`.

[34] Shubo Fei et al. "Investigation on Ignition of a Single Lubricating Oil Droplet in Premixed Combustible Mixture at Engine-Relevant Conditions". In: *SAE Technical Paper* (2019). ISSN: 0148-7191. DOI: `10.4271/2019-01-0298`.

[35] A. Frassoldati, T. Faravelli and E. Ranzi. "Kinetic modeling of the interactions between NO and hydrocarbons at high temperature". In: 135 (2003), pp. 97–112. ISSN: 0010-2180. DOI: `10.1016/s0010-2180(03)00152-4`.

[36] S. K. Friedlander. "Mass and heat transfer to single spheres and cylinders at low Reynolds numbers". In: 3 (1957), pp. 43–48. ISSN: 0001-1541. DOI: `10.1002/aic.690030109`.

[37] Nils Frössling. "Über die Verdunstung fallender Tropfen". In: *Gerlands Beiträge zur Geophysik* (1938), pp. 170–215.

[38] Kosuke Fujimoto et al. "Engine Oil Development for Preventing Pre-Ignition in Turbocharged Gasoline Engine". In: *SAE Int. J. Fuels Lubr.* 7 (2014), pp. 869–874. ISSN: 1946-3960. DOI: `10.4271/2014-01-2785`.

[39] David J. Gardner et al. "Enabling New Flexibility in the SUNDIALS Suite of Nonlinear and Differential/Algebraic Equation Solvers". In: (May 2022). DOI: `10.1145/3539801`. URL: `https://doi.org/10.1145/3539801`.

[40] F. H. Garner and R. B. Keey. "Mass-transfer from single solid spheres I". In: 9 (1958), pp. 119–129. ISSN: 0009-2509. DOI: `10.1016/0009-2509(58)80003-2`.

[41] F. H. Garner and R. B. Keey. “Mass-transfer from single solid spheres II”. In: 9 (1959), pp. 218–224. ISSN: 0009-2509. DOI: `10.1016/0009-2509(59)85004-1`.

[42] B. M. Gauthier, D. F. Davidson and R. K. Hanson. “Shock tube determination of ignition delay times in full-blend and surrogate fuel mixtures”. In: 139 (2004), pp. 300–311. ISSN: 0010-2180. DOI: `10.1016/j.combustflame.2004.08.015`.

[43] Shawn D. Givler and John Abraham. “Supercritical droplet vaporization and combustion studies”. In: 22 (1996), pp. 1–28. ISSN: 0360-1285. DOI: `10.1016/0360-1285(95)00013-5`.

[44] Yifei Gong et al. “A molecular dynamics study of evaporation mode transition of hydrocarbon fuels under supercritical conditions”. In: *Combustion and Flame* 246 (Dec. 2022), p. 112397. DOI: `10.1016/j.combustflame.2022.112397`.

[45] David G Goodwin et al. *Cantera: An Object-oriented Software Toolkit for Chemical Kinetics, Thermodynamics, and Transport Processes*. Version 2.4.0. Aug. 2018. DOI: `10.5281/zenodo.1174508`. URL: `https://doi.org/10.5281/zenodo.1174508`.

[46] David G. Goodwin et al. URL: `https://cantera.org/science/reactors.html` (visited on 08/07/2022).

[47] Ashutosh Gupta et al. “Impact of Particle Characteristics and Engine Conditions on Deposit-Induced Pre-Ignition and Superknock in Turbocharged Gasoline Engines”. In: *SAE International Journal of Fuels and Lubricants* 10 (2017). ISSN: 1946-3960. DOI: `10.4271/2017-01-2345`.

[48] Patrick Haenel et al. *Systematic Approach to Analyze and Characterize Pre-ignition Events in Turbocharged Direct-injected Gasoline Engines*. SAE International. 2011. DOI: `10.4271/2011-01-0343`.

[49] Kai Herrmann. “SFOE project ”Adapted fuels for Dual-fuel and Diesel combustion processes under engine relevant conditions””. In: *Grant no. SI/501628-01, Swiss Federal Office of Energy (SFOE).* ().

[50] Kai Herrmann. “SFOE project ”Investigation of heat transfer (resolved in space and time) by modern combustion processes””. In: *Grant no. SI/501546-01, Swiss Federal Office of Energy (SFOE).* ().

[51] Alan C. Hindmarsh et al. "SUNDIALS: suite of nonlinear and differential/algebraic equation solvers." English. In: *ACM Transactions on Mathematical Software* 31.3 (2005), pp. 363–396. ISSN: 0098-3500. DOI: `10.1145/1089014.1089020`.

[52] G. L. Hubbard, V. E. Denny and A. F. Mills. "Droplet evaporation: Effects of transients and variable properties". In: *International Journal of Heat and Mass Transfer* 18 (1975), pp. 1003–1008. ISSN: 0017-9310. DOI: `10.1016/0017-9310(75)90217-3`.

[53] D. Humair et al. "Characterization of dual-fuel combustion processes". In: *Rostock 6th Large Engine Symposium, ISBN 978-3-941554-22-1* (Sept. 2020).

[54] Teresa Lynn Kaltz. *Simulation of transcritical oxygen droplet vaporization using molecular dynamics*. The Pennsylvania State University, 1998.

[55] Hiromitsu Kawazoe, Katsuyuki Ohsawa and Kenji Fujikake. "LDA measurement of fuel droplet sizes and velocities in a combustion field". In: 82 (1990), pp. 151–162. ISSN: 0010-2180. DOI: `10.1016/0010-2180(90)90094-8`.

[56] Fredrik Königsson. "Advancing the Limits of Dual Fuel Combustion". MA thesis. SE-100 44 Stockholm: Department of Machine Design, Royal Institute of Technology, 2012.

[57] Olawole Abiola Kuti et al. "A fundamental investigation into the relationship between lubricant composition and fuel ignition quality". In: 160 (2015), pp. 605–613. ISSN: 0016-2361. DOI: `10.1016/j.fuel.2015.08.026`.

[58] K. J. Laidler. "A glossary of terms used in chemical kinetics, including reaction dynamics (IUPAC Recommendations 1996)". In: *Pure and Applied Chemistry* 68.1 (Jan. 1996), pp. 149–192. DOI: `10.1351/pac199668010149`.

[59] Keith J. Laidler. "The development of the Arrhenius equation". In: *Journal of Chemical Education* 61.6 (June 1984), p. 494. DOI: `10.1021/ed061p494`.

[60] Malcom Latarche. *Pounder's marine diesel engines and gas turbines*. Ed. by Carrie Bolger. Tenth Edition. Oxford Cambridge, MA: Butterworth-Heinemann, 2021. ISBN: 978-0-08-102748-6.

[61] R. S. Lazar and G. M. Faeth. “Bipropellant droplet combustion in the vicinity of the critical point”. In: 13 (1971), pp. 801–811. ISSN: 0082-0784. DOI: `10.1016/s0082-0784(71)80082-6`.

[62] Arthur Henry Lefebvre. *Atomization and sprays*. Ed. by Vincent G. McDonell. Second edition. Includes bibliographical references and index. Boca Raton: CRC Press, Taylor & Francis Group, 2017. xv, 284 Seiten. ISBN: 9781498736251.

[63] P.J. Linstrom and W.G. Mallard. “NIST Chemistry WebBook, NIST Standard Reference Database Number 69”. In: *National Institute of Standards and Technology* (2009). URL: `http://webbook.nist.gov`.

[64] A. C. Lochiel and P. H. Calderbank. “Mass transfer in the continuous phase around axisymmetric bodies of revolution”. In: 19 (1964), pp. 471–484. ISSN: 0009-2509. DOI: `10.1016/0009-2509(64)85074-0`.

[65] Likun Ma, Bertrand Naud and Dirk Roekaerts. “Transported PDF Modeling of Ethanol Spray in Hot-Diluted Coflow Flame”. In: *Flow, Turbulence and Combustion* 96 (2016), pp. 469–502. ISSN: 1386-6184. DOI: `10.1007/s10494-015-9623-3`.

[66] Jose A. Manrique and Gary L. Borman. “Calculations of steady state droplet vaporization at high ambient pressures”. In: 12 (1969), pp. 1081–1095. ISSN: 0017-9310. DOI: `10.1016/0017-9310(69)90117-3`.

[67] R.L Matlosz, S Leipziger and T.P Torda. “Investigation of liquid drop evaporation in a high temperature and high pressure environment”. In: *International Journal of Heat and Mass Transfer* 15.4 (Apr. 1972), pp. 831–852. DOI: `10.1016/0017-9310(72)90124-x`.

[68] Bonnie McBride, Michael Zehe and Sanford Gordon. “NASA Glenn coefficients for calculating thermodynamic properties of individual species”. In: (Oct. 2002).

[69] Bonnie J. McBride, Sanford Gordon and Martin A. Reno. “Coefficients for calculating thermodynamic and transport properties of individual species”. In: *NASA Technical Memorandum 4513* (Oct. 1993).

[70] Shamel S. Merchant et al. “Understanding low-temperature first-stage ignition delay: Propane”. In: 162 (2015), pp. 3658–3673. ISSN: 0010-2180. DOI: `10.1016/j.combustflame.2015.07.005`.

[71] *Methanverluste entlang der Prozesskette von Flüssiggas (LNG)*. Tech. rep. WD 8 - 3000 – 050/18, WD 8: Umwelt, Naturschutz, Reaktorsicherheit, Bildung und Forschung. Wissenschaftliche Dienste Deutscher Bundestag, 2018.

[72] R. S. Miller, K. Harstad and J. Bellan. "Evaluation of equilibrium and non-equilibrium evaporation models for many-droplet gas-liquid flow simulations". In: 24 (1998), pp. 1025–1055. ISSN: 0301-9322. DOI: `10.1016/s0301-9322(98)00028-7`.

[73] Kazuhisa Mogi et al. "Analysis and avoidance of pre-ignition in S.I. gasoline engines". In: *JSAE Review* 19 (1998), pp. 9–14. ISSN: 0389-4304. DOI: `10.1016/s0389-4304(97)00045-3`.

[74] Yasuo Moriyoshi et al. "A Study of Low Speed Preignition Mechanism in Highly Boosted SI Gasoline Engines". In: *SAE International Journal of Engines* 9 (2016), pp. 98–106. ISSN: 1946-3944. DOI: `10.4271/2015-01-1865`.

[75] Charles E. Mortimer and Ulrich Müller. *Chemie: Das Basiswissen der Chemie*. Ed. by Johannes Beck. 12., korrigierte und aktualisierte Auflage. Georg Thieme Verlag, 2015. ISBN: 978-3-13-206292-4. DOI: `10.1055/b-003-125838`.

[76] P. Muller. "Glossary of terms used in physical organic chemistry (IUPAC Recommendations 1994)". In: *Pure and Applied Chemistry* 66.5 (Jan. 1994), pp. 1077–1184. DOI: `10.1351/pac199466051077`.

[77] Hiroshi Nomura et al. "Experimental study on high-pressure droplet evaporation using microgravity conditions". In: 26 (1996), pp. 1267–1273. ISSN: 0082-0784. DOI: `10.1016/s0082-0784(96)80344-4`.

[78] Yuanjiang Pei et al. *A Multi-Component Blend as a Diesel Fuel Surrogate for Compression Ignition Engine Applications*. 2014. DOI: `10.1115/icef2014-5625`.

[79] Linda Petzold. "Automatic Selection of Methods for Solving Stiff and Nonstiff Systems of Ordinary Differential Equations". In: *SIAM Journal on Scientific and Statistical Computing* 4.1 (Mar. 1983), pp. 136–148. DOI: `10.1137/0904010`.

[80] Abgail P. Pinheiro and João Marcelo Vedovoto. “Evaluation of Droplet Evaporation Models and the Incorporation of Natural Convection Effects”. In: 102 (2019), pp. 537–558. ISSN: 1386-6184. DOI: `10.1007/s10494-018-9973-8`.

[81] WE Ranz and WR Marshall. “Evaporation from drops: Part 1”. In: *Chemical Engineering Progress* 48 (1952), pp. 141–146. ISSN: 0360-7275.

[82] E. Ranzi et al. “Hierarchical and comparative kinetic modeling of laminar flame speeds of hydrocarbon and oxygenated fuels”. In: 38 (2012), pp. 468–501. ISSN: 0360-1285. DOI: `10.1016/j.pecs.2012.03.004`.

[83] E. Ranzi et al. “Reduced Kinetic Schemes of Complex Reaction Systems: Fossil and Biomass-Derived Transportation Fuels. REDUCED KINETIC SCHEMES OF COMPLEX REACTION SYSTEMS”. In: 46 (2014), pp. 512–542. ISSN: 0538-8066. DOI: `10.1002/kin.20867`.

[84] Eliseo Ranzi et al. “New reaction classes in the kinetic modeling of low temperature oxidation of n-alkanes”. In: 162 (2015), pp. 1679–1691. ISSN: 0010-2180. DOI: `10.1016/j.combustflame.2014.11.030`.

[85] Jan Reimer et al. “Basic investigations on the cause of initial pre-ignition in aconstant volume combustion cell”. In: *International Conference on Ignition Systems for Gasoline Engines – International Conference on Knocking in Gasoline Engines*. Ed. by Marc Sens. expert verlag, Oct. 2022. DOI: `10.24053/9783816985440`.

[86] P.N. Rowe, K.T. Claxton and J.B. Lewis. *Heat and Mass Transfer from a Single Sphere in an Extensive Flowing Fluid at Reynolds Numbers Less Than 2,000*. AERE-R. UK Atomic Energy Authority Research Group, 1964.

[87] S. M. Sarathy et al. “Comprehensive chemical kinetic modeling of the oxidation of 2-methylalkanes from C7 to C20”. In: 158 (2011), pp. 2338–2357. ISSN: 0010-2180. DOI: `10.1016/j.combustflame.2011.05.007`.

[88] Hermann Schlichting. *Boundary-Layer theory*. Ed. by Klaus Gersten et al. Ninth edition. Literaturverzeichnis: Seite 717-797. Berlin: Springer, 2017. XXVIII, 805 Seiten. ISBN: 9783662529171.

[89] B. Schneider and K. Boulouchos. “Final report of the CCEM project ”Flex-FI-Dual (Flexible Facility for the Investigation of Gas, Diesel and Dual-fuel Combustion)””. In: *Swiss Competence Center Energy and Mobility (CCEM)* (2017).

[90] Thorsten Schweizer et al. *Initial Pre-Ignition. Project no. 1328, Identification of the mechanism for initial pre-ignition by a combination of experimental investigations and simulation of drop ignition; Final report*. Frankfurt/M: FVV, Forschungsvereinigung Verbrennungskraftmaschinen e.V., 2021.

[91] William A. Sirignano. *Fluid dynamics and transport of droplets and sprays*. 2. ed. Literaturverz. S. 427 - 459. Cambridge [u.a.]: Cambridge University Press, 2010. XVIII, 462. ISBN: 9780521884891.

[92] Gregory P. Smith et al. URL: `http://www.me.berkeley.edu/gri_mech/` (visited on 08/06/2022).

[93] Michel Soustelle. *An Introduction to Chemical Kinetics*. ISTE LTD, July 2011. 480 pp. ISBN: 1848213026.

[94] A. Stagni et al. “Skeletal mechanism reduction through species-targeted sensitivity analysis”. In: 163 (2016), pp. 382–393. ISSN: 0010-2180. DOI: `10.1016/j.combustflame.2015.10.013`.

[95] Alessandro Stagni et al. “Lumping and Reduction of Detailed Kinetic Schemes: an Effective Coupling”. In: 53 (2014), pp. 9004–9016. ISSN: 0888-5885. DOI: `10.1021/ie403272f`.

[96] Sten H. Stårner, James Gounder and Assaad R. Masri. “Effects of turbulence and carrier fluid on simple, turbulent spray jet flames”. In: *Combustion and Flame* 143.4 (Dec. 2005), pp. 420–432. DOI: `10.1016/j.combustflame.2005.08.016`.

[97] P. Süess, P. Albrecht and K. Herrmann. “Pre-Ignition in Dual-Fuel/Gas Engines”. In: *SFOE project, Final Report, Grant no. SI/501942-01, Swiss Federal Office of Energy (SFOE)* ().

[98] Stephen R. Turns. *An introduction to combustion. Concepts and applications*. 2. ed. McGraw-Hill series in mechanical engineering. Boston, Mass. [u.a.]: McGraw-Hill, 2000. XXIII, 676. ISBN: 007235044X.

[99] Fridolin Unfug and German Andreas Weisser. "Assessment of the Combustion Process in Ultra-Lean ($\lambda > 1.8$) Natural Gas Engines". In: *SAE Technical Paper Series*. SAE International, Aug. 2022. DOI: `10.4271/2022-01-1061`.

[100] Santosh K. Upadhyay. *Chemical Kinetics and Reaction Dynamics*. Springer Netherlands, 2006. DOI: `10.1007/978-1-4020-4547-9`.

[101] Guido Van Rossum and Fred L. Drake. *Python 3 Reference Manual*. Scotts Valley, CA: CreateSpace, 2009. ISBN: 1441412697.

[102] Pauli Virtanen et al. "SciPy 1.0: fundamental algorithms for scientific computing in Python". In: *Nature Methods* 17.3 (Feb. 2020), pp. 261–272. DOI: `10.1038/s41592-019-0686-2`.

[103] Bosen Wang et al. "Fully resolved DNS of droplet array combustion in turbulent convective flows and modelling for mixing fields in inter-droplet space". In: 189 (2018), pp. 347–366. ISSN: 0010-2180. DOI: `10.1016/j.combustflame.2017.11.003`.

[104] Daniel Weber. "Flash Boiling bei Ottomotoren mit Benzindirekteinspritzung: Experimentelle Untersuchungen, Modellierung und numerische Simulation". PhD thesis. Technische Universität Darmstadt, 2016.

[105] Sebastian Welscher et al. "A Detailed Reaction Kinetics-Based Calculation Tool for Internal Combustion Engine-Related Ignition Processes". In: *SAE Technical Paper* (2022). DOI: `10.4271/2022-01-5050.`.

[106] Lukas Wißmann, Pascal Süess and Patrick Albrecht. "Modeling of Preignition in Gas Engines". In: *FVV Final Report, Project no. 1394* (2023).

[107] Lukas Wißmann, Pascal Süess and Patrick Albrecht. "Phänomenologische Modellierung von Vorentflammung in Gas-Motoren". In: *FVV-Informationstagung | Herbst 2022 – Würzburg Heft R603* (2022).

[108] Lukas Wißmann et al. "Detailed Numerical Investigation of the Influences of External Water, Lubricating Oil and Reactive EGR Components on ICE Ignition Processes". In: *Proceedings of The 10th International Conference on Modeling and Diagnostics for Advanced Engine Systems* 22-201 (July 2022).

[109] Lukas Wißmann et al. “Development of a Predictive 0/1D Model for Lubricating Oil Induced Pre-Ignitions at an Optical Gas/Dual-Fuel Engine.” In: *International Conference on Ignition Systems for Gasoline Engines – International Conference on Knocking in Gasoline Engines*. Ed. by Marc Sens. expert verlag, Oct. 2022. DOI: `10.24053/9783816985440`.

[110] Silas Wüthrich et al. “Optical investigation and thermodynamic analysis of premixed ammonia dual-fuel combustion initiated by dodecane pilot fuel”. In: *Fuel Communications* 12 (Sept. 2022), p. 100074. DOI: `10.1016/j.jfueco.2022.100074`.

[111] Changlin Yan and Suresh K. Aggarwal. “A High-Pressure Droplet Model for Spray Simulations”. In: *Journal of Engineering for Gas Turbines and Power* 128.3 (2006), p. 482. DOI: `10.1115/1.1915390`.

[112] Shinji Yasueda, Koji Takasaki and Hiroshi Tajima. “Abnormal Combustion caused by Lubricating Oil in High BMEP Gas Engines”. In: *MTZ Industrial* 3 (2013), pp. 34–39. ISSN: 2194-8682. DOI: `10.1007/s40353-013-0069-6`.

[113] Shinji Yasueda, Koji Takasaki and Hiroshi Tajima. “The Abnormal Combustion Affected by Lubricating Oil Ignition in Premixed Gas Engine”. In: *ASME 2012 Internal Combustion Engine Division Spring Technical Conference* (2012). DOI: `10.1115/ices2012-81042`.

[114] M. C. Yuen and L. W. Chen. “On Drag of Evaporating Liquid Droplets”. In: *Combustion Science and Technology* 14 (1976), pp. 147–154. ISSN: 0010-2202. DOI: `10.1080/00102207608547524`.

[115] Jean-Marc Zaccardi and David Serrano. “A Comparative Low Speed Pre-Ignition (LSPI) Study in Downsized SI Gasoline and CI Diesel-Methane Dual Fuel Engines”. In: *SAE International* 7 (2014), pp. 1931–1944. ISSN: 1946-3944. DOI: `10.4271/2014-01-2688`.

[116] G. S. Zhu and S. K. Aggarwal. *Fuel Droplet Evaporation in a Supercritical Environment*. 1999. DOI: `10.1115/99-gt-301`.

[117] Shengrong Zhu et al. “A Method for Developing Countermeasures to Lube-oil Pre-ignition in Gas Engines”. In: 5 (2015), pp. 54–61. ISSN: 2194-8682. DOI: `10.1007/s40353-015-0517-6`.